# The Impact of Sunspot Rotation on Solar Flares

Andrew Walker

A THESIS SUBMITTED IN PARTIAL FULFILMENT
OF THE REQUIREMENTS FOR THE DEGREE OF
DOCTOR OF PHILOSOPHY

Jeremiah Horrocks Institute for Maths, Physics and Astronomy

University of Central Lancashire

February 2018

# Declaration

The work presented in this thesis was carried out at the Jeremiah Horrocks Institute for Maths, Physics and Astronomy, University of Central Lancashire.

I declare that while registered as a candidate for the research degree, I have not been a registered candidate or enrolled student for another award of the University or other academic or professional institution.

I declare that no material contained in the thesis has been used in any other submission for an academic award. Data and models used in this thesis that are not my own are clearly cited in the text.

# Abstract

Solar flares are one mechanism to release stored magnetic energy in the Sun's atmosphere. This thesis aims to determine whether sunspot rotation can inject the energy required for solar flares into the corona. This thesis investigates the relationship between sunspot rotation and solar flares, and the impact that sunspot rotation has on the strength and frequency of flare events.

A robust analysis tool is developed which uses continuum images of the Sun to determine the rotation of sunspots. This tool is used throughout the thesis, first on the active region 11158, in an in-depth case study of the rotation and flaring properties of the region as it traverses the solar disc. The case study develops analysis techniques, such as introducing sunspot selection criteria, which are used in the following statistical studies. The first statistical study involves the analysis of the rotation and flaring properties of a sample of all sunspots that meet the selection criteria within all X-class flaring regions since the launch of the Solar Dynamics Observatory. As this first statistical study is biased towards higher flare-energy active regions, a second unbiased statistical study is carried out on all sunspots that meet the sunspot selection criteria between 1 May 2013 and 31 August 2013. The results of these statistical studies are combined and analysed, concluding that sunspot rotation injects enough energy (and in the majority of cases, an excess of energy) to account for the energy output by solar flare radiation. On average, the radiated bolometric flare energy outputs 65.6% of the injected energy due to the absolute sunspot rotation for the X-class flare sample, and 59.2% for the four-month

sample.

# Contents

# List of Tables

# List of Figures

# Acknowledgements

I would firstly like to thank my supervisor, Dan Brown, for his support throughout my PhD, without which this thesis would not be possible.

I would like to thank everyone at the Jeremiah Horrocks Institute for being so supportive throughout both my undergraduate degree and PhD, as well as the STFC for the three and a half years of funding.

A huge thanks go to my parents, Carole and Phillip Walker. Without their constant support and encouragement, I would not be where I am today.

Thanks to all of my PhD peers for their friendship and support. Thanks in particular to Danny Lee for fuelling my caffeine addiction, Ben MacFarlane for fuelling my Domino's pizza addiction and Steven Bourn for his friendship throughout both my undergraduate and postgraduate degrees. I also wish to thank Linus Nybergh for his long-distance support and friendship throughout my time at university.

# Chapter 1

# Introduction

The Sun provides the light and warmth that all living beings on Earth require to survive. However, the Sun is also extremely active, and solar phenomena such as solar flares, coronal mass ejections and energetic particle events can affect us detrimentally. This activity can have a direct impact on satellite communications, power grids, and can even be harmful to astronauts and polar aircraft flight passengers (Lam et al. 2002). As such it is important to understand the underlying physics of the Sun and solar phenomena.

Our understanding of the Sun has vastly improved since the advent of the telescope. Through persistent sunspot observations, astronomers recognised that sunspot numbers varied on an approximate 11-year cycle (Schwabe 1844; Hathaway 2010), and eclipse observations uncovered the faint outer atmosphere, the solar corona. Observations of the Sun have evolved dramatically over the last 400 years, and presently space-based instruments such as the Solar Dynamics Observatory (SDO) provide 24-hour observations of the Sun in a multitude of different wavelengths. It is also possible to measure the surface magnetic field of the Sun, as well as surface and even interior plasma flows.

Presented in this thesis are results pertaining to sunspot rotation. This work ranges from the definition and calculation of sunspot rotation, to the role that

sunspot rotation plays in solar activity, particularly solar flares. Documented in this thesis is the first quantitative relationship between sunspot rotation and solar flare energy, furthering our understanding of the injection and subsequent release of magnetic energy in solar flare events.

This chapter provides a brief summary of the properties of the Sun, as well as a brief history of solar observations. Towards the end of the chapter, the work carried out in this thesis is contextualised through a description of the literature relating to sunspot rotation.

## 1.1    The Solar Interior

The Sun is comprised mainly of ionised hydrogen and helium atoms (92% and 8% respectively, by number), with trace amounts of heavier elements such as Carbon, Nitrogen and Oxygen (Priest 2014). The interior of the Sun can be divided into three regions based on their physical properties. In order of increasing radius, these regions are defined as the core, the radiative zone, and the convection zone, as shown in figure 1.1.

The core of the Sun has a typical peak temperature of 15 million degrees Kelvin and an average density of $1.6 \times 10^5$ kg/m$^3$, which fall off as a function of radius, out to the edge of the core at about 0.25 R$_\odot$. At these temperatures, protons can quantum tunnel through their Coulomb barriers and fuse together in what is called the proton-proton (PP) chain. The PP chain fuses four protons into one helium nucleus, releasing energy in the process, and is the dominant form of nuclear fusion that takes place in the core of smaller stars such as the Sun (Burnell et al. 2003).

The radiative zone is the next layer radially outwards from the core, where the dominant energy transport process is radiation. Photons within the radiative zone are continually absorbed and re-emitted, such that it takes a vast amount of time (on the order of $10^6$ years) for light to eventually escape (Burnell et al.
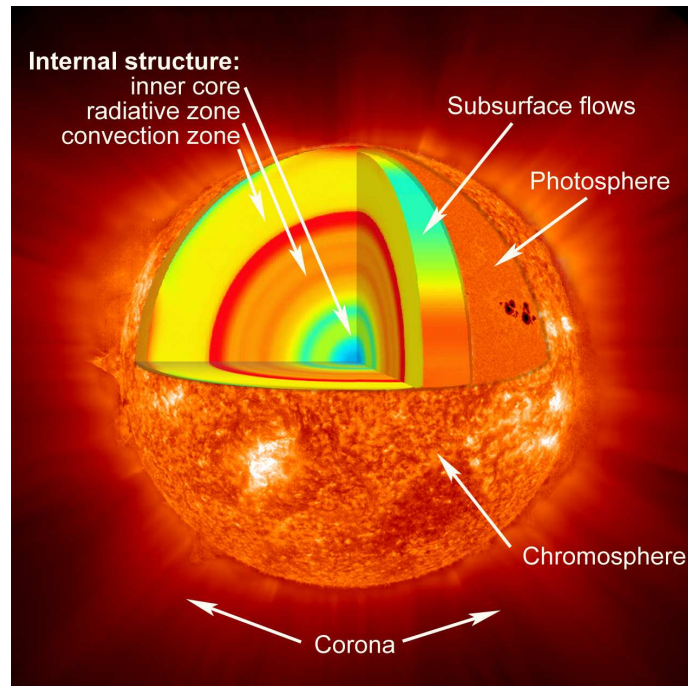
**Figure 1.1:** *Schematic showing the layers of the Sun, from the core out to the solar atmosphere. Image credit: NASA*

2003). The opacity of the radiative zone increases rapidly as the distance from the core increases due to the drop in temperature, until around 0.7 $R_\odot$, where the convective zone begins. This increase in opacity leads to a steeper temperature gradient, and convective instability occurs when the vertical temperature gradient ($|dT/dr|$) becomes too large (Stix 2002). The plasma becomes hot and buoyant, rising through the solar interior. The plasma cools when it reaches the surface of the Sun, falls, and gets re-heated again as it falls further through the interior, forming a convective flow.

Between the radiative and convective zones lies a layer known as the tachocline. The tachocline is a narrow shear layer that lies at approximately 0.713 $R_\odot$ (Priest 2014), where the rotation velocity rapidly changes from being uniform in the radiative zone to non-uniform in the convective zone (Tobias et al. 1995; Hughes et al. 2007).

## 1.2 The Solar Cycle

Many solar phenomena are magnetic in nature. There are many features of the Sun's magnetic field that indicate an underlying pattern - referred to as the solar cycle - and hint towards the nature of the magnetic field (Priest 2014). The main features of the solar cycle are as follows:



**DAILY SUNSPOT AREA AVERAGED OVER INDIVIDUAL SOLAR ROTATIONS**
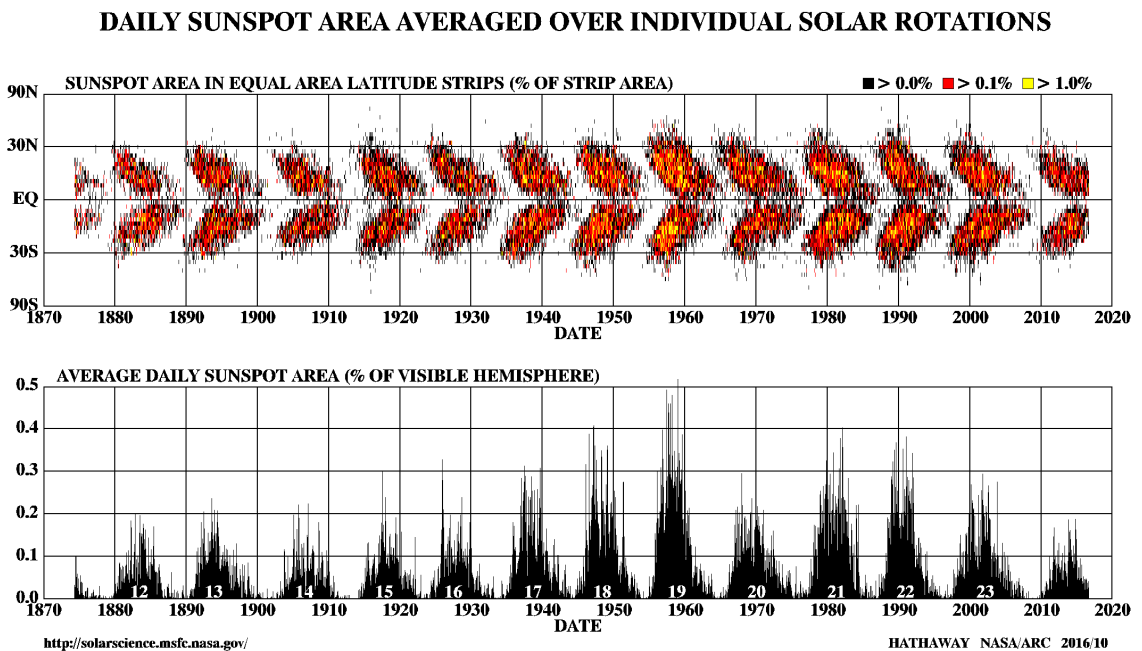
***Figure 1.2:*** *Top: The butterfly diagram. This shows the variation of solar lati-tude as a function of time over 13 solar cycles. The colour indicates the percentage of the area sunspots occupy in each latitudinal strip. Lower: Sunspot area versus time. The sunspot area is used as a gauge of solar activity, and reveals the approx-imate 11-year solar cycle (sunspot area is used as an analogue of sunspot number). Image credit: NASA*

- There is an approximate 11-year sunspot number cycle, in which there is a sunspot number peak at solar maximum and a trough at solar minimum. The lower plot in figure 1.2 illustrates the solar cycle, tracked by sunspot area.

- Sunspots are typically limited to latitudes of $\pm 35°$. As per Sporër's Law, sunspots tend to emerge closer to the poles at solar minimum, and emerge closer to the equator as the solar cycle progresses towards maximum, illustrated in the top panel of figure 1.2.

- Leading sunspots are more inclined towards the equator relative to following sunspots in the same active region. The amount of inclination reduces as regions form closer to the equator; this is known as Joy's Law.

- The polarity of the solar poles flips every 11 years. Leading sunspots in each hemisphere all have the same polarity, and the polarity of these leading spots swaps every 11 years, implying an underlying 22-year magnetic cycle. The polarity of leading sunspots in each hemisphere is always opposite (e.g. if positive polarity sunspots lead in the northern hemisphere, negative polarity spots lead in the southern hemisphere).

Over the solar cycle, the global poloidal field is dragged by the solar equator rotating faster than the poles (differential rotation), generating a more toroidal field (this is known as the $\omega$-effect). The conversion back to the poloidal field and the field reversal to end the cycle is much more complicated. The $\alpha$-effect, defined in Parker's dynamo model, describes how localised regions of toroidal field can reconnect and reconfigure into a poloidal field. If this occurs frequently enough, these poloidal components can coalesce into a global poloidal field, completing the magnetic solar cycle (Dwivedi 2003).
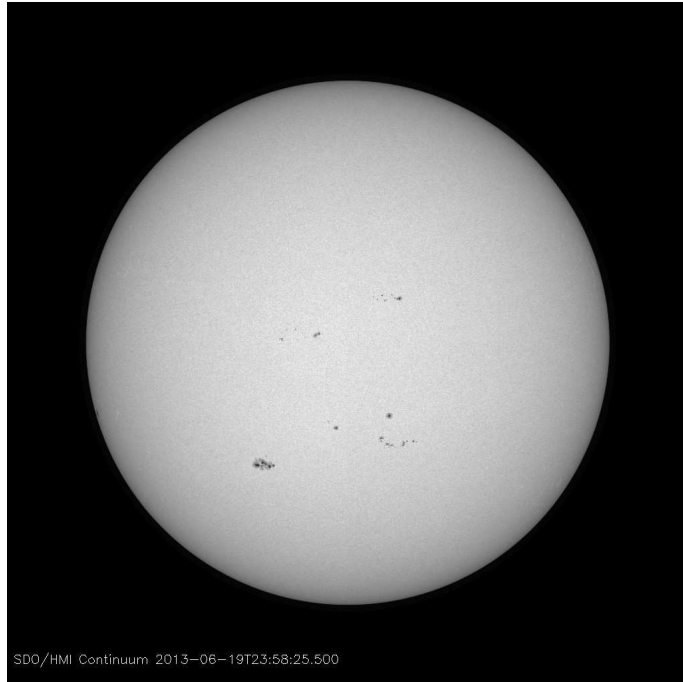
**Figure 1.3:** *A SDO/HMI observation of the photosphere from the continuum data series, taken in June 2013 during solar maximum; the dark spots seen on the surface are sunspots. Image credit: NASA/SDO*

## 1.3 The Solar Atmosphere

### 1.3.1 The Photosphere

The photosphere (figure 1.3) is the visible solar surface, and emits the vast majority of the Sun's visible light. The photosphere has an average temperature of approximately 5800 K, and a thickness of around 300 km. Visible on the photosphere at all times and present over the whole solar surface is granulation. Granules are locations where convective currents reach the solar surface, bringing up hot (and therefore bright) material, visible in the middle of the granule, which flows horizontally to the outer edge of the granule as the plasma cools and sinks back into the interior. Granules have typical diameters of approximately 1 Mm and average lifetimes of around 7 minutes. Granules constantly form and disperse, such that the

photosphere is an extremely dynamic place (Priest 2014).

As well as granules, substantially larger, much longer lived features called supergranules can be observed on the photosphere as a pattern of horizontal motions. Supergranulation is most easily seen through horizontal motions on the solar surface, rather than in white light intensity images. A typical supergranule would have a diameter of approximately 30 Mm and a lifetime of between 1 and 2 days. Supergranules can be formed between existing supergranule cells, or by fragmentation of an existing supergranule (Foukal 2013). Supergranules are large-scale convection cells, with plasma rising at approximately 30 $ms^{-1}$ at the centre, and moving radially outwards at around 350 $ms^{-1}$ and descending at the supergranular boundary (Priest 2014).

## 1.3.2   Sunspots and Active Regions

There are many sources of magnetic flux present in the photosphere. The weaker magnetic field components occupy the supergranular cells, and have typical magnetic field strengths of between 100 and 300 G. The stronger, more vertical fields are present in smaller, more concentrated regions of flux. These regions are observed as dark regions on the photosphere, where the intense magnetic field inhibits convection, cooling the plasma, and are called pores or sunspots depending on their size and properties. It is widely understood that sunspots are locations where regions of strong magnetic field generated in the solar interior penetrate the solar surface and can act as footpoints for flux tubes (Priest 2014).

Sunspots generally consist of a central dark umbra and an outer, lighter penumbra, whereas pores tend to be smaller and have little to no penumbra. The umbral magnetic field is almost completely vertical relative to the solar surface, with a very high magnetic field strength of around 3 kG. The penumbral magnetic field is less vertical, becoming more horizontal with increasing radius from the sunspot centre,
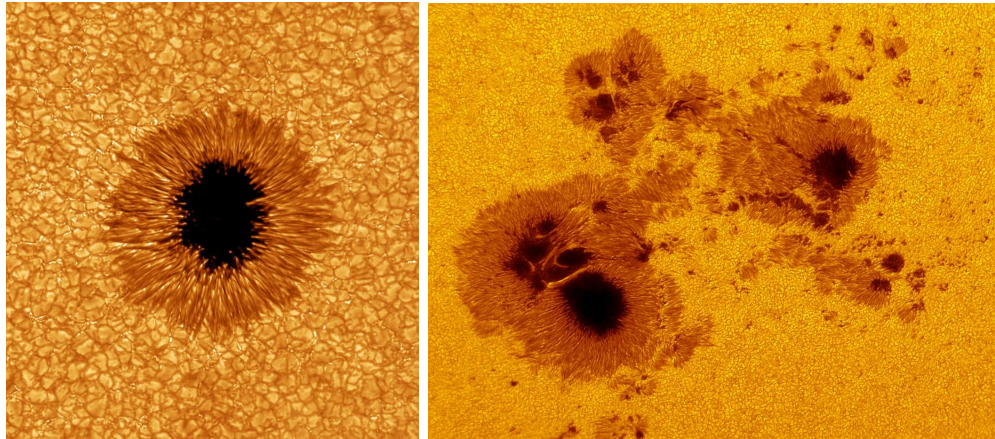
***Figure 1.4:*** *Left panel: A continuum image of a single sunspot taken by the Big Bear Solar Observatory. The central dark umbra and the brighter penumbra can be seen clearly. The light and dark lines in the penumbra directed radially outwards from the umbra are fibrils. Granulation can be seen in the photosphere surrounding the sunspot. This is an example of a simple, unipolar active region. Right panel: NOAA active region 12192 taken from the SDO/HMI continuum data series. This is an example of an extremely complex active region, in which one penumbra surrounds separate umbrae of opposite polarities. Image credit: BBSO (left) and NASA (right)*

and has a lower magnetic field strength than the umbra, typically around 1 kG. Sunspots sizes can vary quite significantly, although tend to have radii between 5-30 Mm. The lifetime of sunspots is generally related to their size; 5 Mm radii spots tend to last for 2 to 3 days, while 30 Mm spots can last for up to 90 days (Thomas & Weiss 2008).

Sunspot penumbrae contain extremely fine features called penumbral fibrils (these can be seen in figure 1.4), which vary from 3.5 to 7 Mm in length, and last for between 0.5 and 6 hours (for reference, it is these fibrils which are tracked and used to calculate sunspot rotation in this thesis). Penumbral fibrils form in the penumbra and tend to move inwards (towards the sunspot centre) in the inner 60% of the

penumbra and outwards in the outer penumbra (Priest 2014).

Groups of sunspots and/or pores are referred to as active regions, and are defined based on their magnetic complexity (Hale & Nicholson 1938). The majority of active regions are either unipolar ($\alpha$ type) or bipolar ($\beta$ type). However, a small number of active regions are more complex in their magnetic structure ($\gamma$ type), and some even contain multiple umbrae of differing polarity in the same penumbra ($\delta$ type). These more complex active regions are likely to produce solar flares and coronal mass ejections. An example of an extremely complex active region (a $\beta\gamma\delta$ configuration) is shown in the right-hand panel of figure 1.4.

### 1.3.3 The Corona

The solar corona was initially observed in visible light during solar eclipses, with the light originating from scattering from both electrons and dust (the K- and F-corona respectively). This is due to the photosphere being several orders of magnitude brighter than the corona in visible light, and as such, the solar disc must be occulted for the corona to be seen. However, the corona can be imaged directly in extreme ultraviolet (EUV) and X-ray emission lines, as the contribution from the photosphere in these wavelengths is negligible (Golub & Pasachoff 2013).

At coronal temperatures of around 1 MK, the material is so hot that hydrogen is fully ionised, and up to 15 electrons may be stripped from heavier nuclei. Due to this highly ionised state, the plasma is dominated by the magnetic field and traces magnetic structures (akin to iron filings around a bar magnet). The source of the extremely high temperature in the corona is understood to be the solar magnetic field, however the mechanism by which the plasma is heated is not yet understood. This is known as the coronal heating problem. There are, however, two main mechanisms that have been proposed. The first mechanism relies on magnetic waves formed in the convective zone propagating up into the corona and releasing their
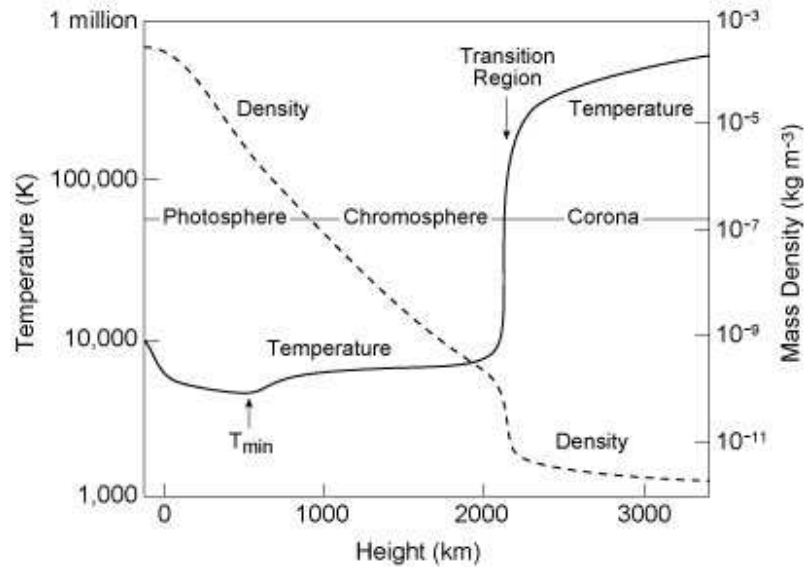
**Figure 1.5:** *The temperature profile of the solar atmosphere. The solid line represents the change in temperature as a function of height above the photosphere and the dashed line represents the change in density. The sharp increase in temperature at just over 2000 km above the photosphere occurs in a region known as the transition region, residing between the chromosphere and corona. Image credit: NASA*

energy, whereas the second mechanism suggests that magnetic reconnection over an array of current sheets, arising from series of equilibria from the highly dynamic magnetic field, provides the energy required to heat the corona. Even though the specific mechanisms differ, coronal heating is generally accepted to be magnetic in origin (Priest 2014). As the chromospheric and coronal fields are so complex, and magnetic footpoints in the photosphere are observed to fragment and be continuously dynamic, coronal structures are also in a state of constant change. This leads to very intricate interactions in the coronal magnetic field, suggesting that reconnection, leading to nanoflares, is a potential coronal heating theory (Parker 1972; Priest 2014).

Magnetic field lines in the lower corona are generally closed. Coronal loops arch
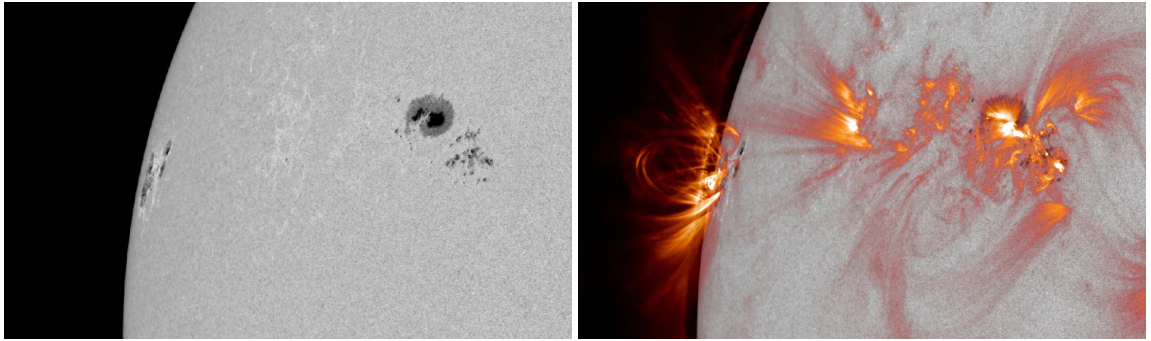
*(a)* HMI continuum                  *(b)* AIA 171/HMI continuum composite

***Figure 1.6:*** *The structure of coronal loops above the solar photosphere. Figure b) shows how the location of footpoints of these loops correspond with the location of sunspots.*

out of the photosphere and into the corona, and join two footpoints which correspond to sunspots or pores within active regions, or the plage field (figure 1.6). Coronal loops can be small (contained within a single active region) or large (loops that connect sunspots in different active regions), and can reach temperatures of up to 4 MK. In the upper corona, magnetic field lines tend to be more open, stretched out by the solar wind, giving rise to phenomena such as helmet streamers (Golub & Pasachoff 2013). Although not the subject of this thesis, it should also be noted that active region magnetic fields may also arise from the magnetic network, rather than sunspots or pores.

### 1.3.4   Solar Wind

The solar wind is generally categorised as either slow or fast solar wind. The slow solar wind travels away from the Sun at between 300 and 400 km/s, whereas the fast solar wind moves at much higher velocities, between 700 and 750 km/s (Priest 2014). The slow solar wind originates from coronal hole/streamer boundaries at solar minimum, and small coronal holes and active regions at solar maximum.

CHAPTER 1

In portions of the solar corona, the magnetic field may be "open". As opposed to coronal loops, which are considered closed magnetic fields, coronal holes are open portions of the solar magnetic field, with the field extending out into the solar atmosphere. The fast solar wind originates solely from regions of open magnetic field, such as large coronal holes, as shown in figure 1.7. Coronal holes appear much darker as they are cooler and less dense than the surrounding coronal material, and their open magnetic field allows easier passage for the plasma to escape, and hence leads to a faster solar wind.
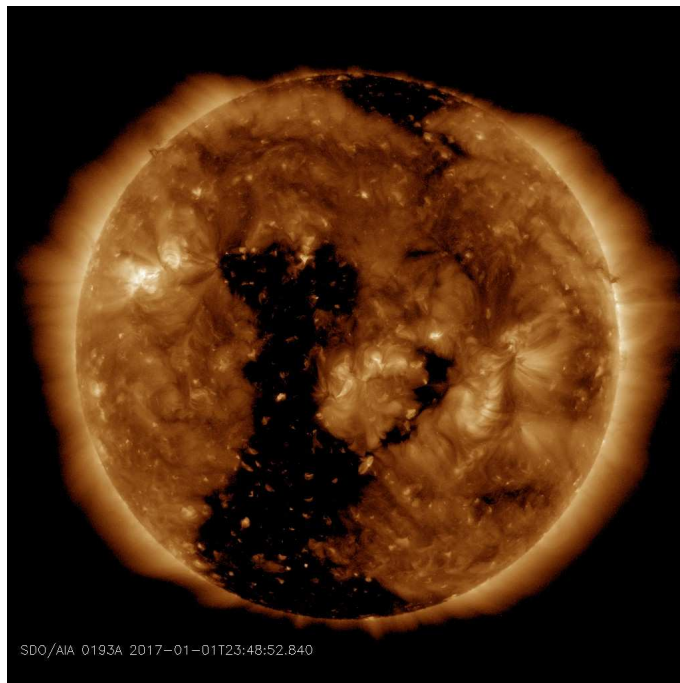


**Figure 1.7:** *A 193 Å image of the corona taken by SDO/AIA. The dark regions are coronal holes, regions of large-scale open magnetic field, and the origin of the fast solar wind. Image credit: NASA*

## 1.4   Solar Activity

Solar activity is manifest in various forms, the most widely studied of which are solar flares, coronal mass ejections and energetic particle events. Solar activity is best observed in the solar corona, particularly in the case of solar flares and coronal mass ejections. This section covers the basics of solar flares and coronal mass ejections.

### 1.4.1   Solar Flares

A solar flare is defined as a sudden brightening of solar irradiance, generally in X-rays. Solar flares are categorised in ascending order from A-, B-, C-, M- and X-class based on their peak 1-8 Å X-ray flux, as measured by GOES, with X-class flares peaking at $10^{-4}$ W m$^{-2}$ or greater (figure 1.8). Solar flare classification is a magnitude scale, such that a X1.0 flare is ten times greater in peak flux than a M1.0 flare, and one hundred times greater in flux than a C1.0 flare. The number of flare occurrences varies with the solar cycle, but on average there are between 1-10 X-class and 20-300 M-class solar flares per year. Solar flares are the most energetic events in the solar system; a large X-class solar flare can radiate over $2 \times 10^{32}$ erg of energy (Foukal 2013).

It is widely accepted that solar flares are triggered by the sudden release of magnetic energy via magnetic reconnection, where a highly complex and twisted magnetic field reconfigures into a less energetic state. Several models have been proposed regarding the build-up and triggering of solar flares. However, one big problem lies in the link between solar flares and coronal mass ejections, as there is not a one-to-one relationship between the two. This means there are potentially several mechanisms through which solar flares are triggered. One such flaring model is known as the standard flare model, and is discussed in section 1.4.3 (Golub & Pasachoff 2013).
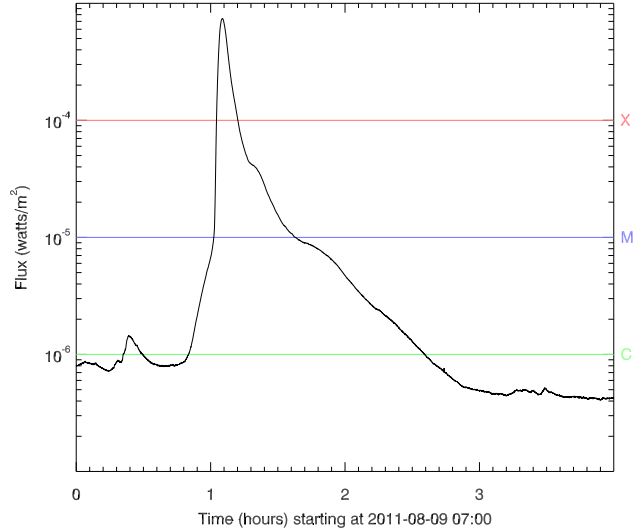
**Figure 1.8:** *GOES 1-8 Å full-disc X-ray flux over a four-hour period showing the X6.9 flare associated with AR11263, the largest observed flare of solar cycle 24. The red horizontal line represents the X-class flare classification, the blue horizontal line represents the M-class flare classification, and the green horizontal line represents the C-class flare classification.*

## 1.4.2 Coronal Mass Ejections

Coronal mass ejections (CMEs) are essentially bubbles of magnetised plasma that escape the Sun and expand out into interplanetary space, as shown in figure 1.9. These eruptions can have many adverse effects on Earth, potentially causing geomagnetic storms and solar energetic particle events.

CMEs typically eject a mass of between $10^{11}$ and $4 \times 10^{13}$ kg at speeds of several hundreds to thousands of kilometres per second. The angular width of CMEs ranges from as low as 20° up to 360°, and their average width is larger at solar maximum than solar minimum. Coronal mass ejections can carry up to $10^{32}$ erg of kinetic energy, which is comparable to the radiative energy of solar flares. The frequency of CMEs is also dependent upon the solar cycle, with fewer than 1 per day at solar minimum and up to 6 per day at solar maximum (Priest 2014).
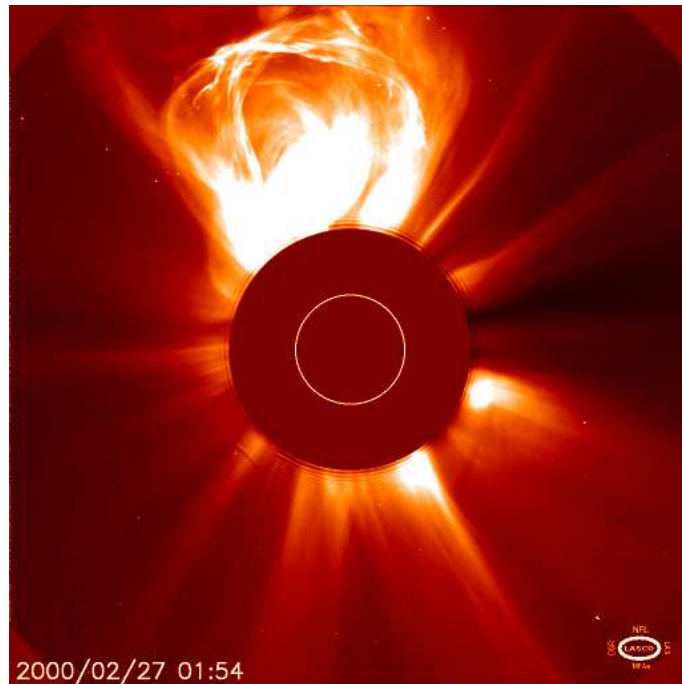
**Figure 1.9:** *A coronal mass ejection imaged by the SOHO/LASCO coronagraph. The dark central disc is an occulting disc, used to block out direct photospheric light, allowing the fainter corona to be imaged. The white circle within the occulting disc indicates the position and size of the Sun. Image credit: NASA*

As with flares, not all CMEs are associated with other events but almost certainly occur as a result of magnetic reconnection. CMEs may erupt from filaments, such as active region filaments (typically associated with large flare events), or non-active region filaments such as polar crown filaments.

### 1.4.3   The Standard Flare Model

Although flare phases and CME structures have been studied extensively, the precise mechanisms through which flares and CMEs are triggered are not fully understood, although magnetic reconnection is believed to play an important role in both events. In this section, the standard flare model is discussed, an illustration of which is shown in figure 1.10. It is worth noting that there are many flare models, and it would be

impossible to list them all here (Priest 2014).



Reconnecting
Magnetic Field Line

New Reconnected
Magnetic Field Lines

Large Coronal
Loop

Inflowing
Magnetic Field

Hot Flare
Loop

New Reconnected
Magnetic Field Lines
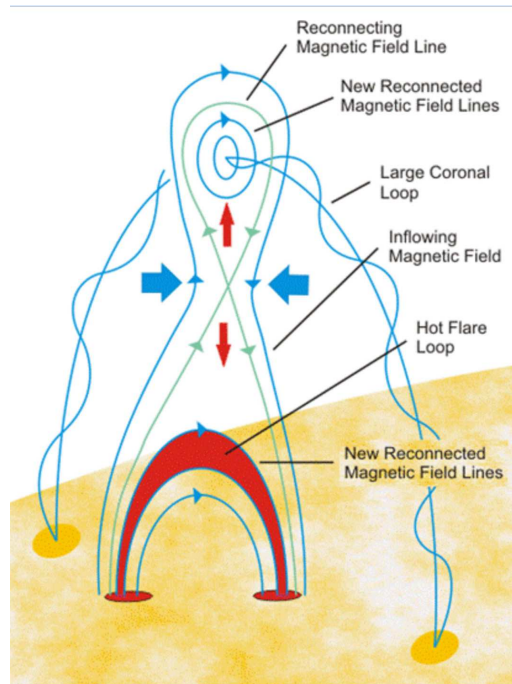
***Figure 1.10:*** *A schematic of the standard flare model. The region of magnetic reconnection is illustrated by the blue and red arrows, indicating the direction of the plasma flow. This reconnection may release the top portion of the magnetic field, in which some coronal plasma is suspended, releasing a CME. Image credit: NASA*

This model applies to two-ribbon flares. These ribbons are brightenings seen in H$\alpha$ that appear as elongated bands of emission on either side of the magnetic neutral line. Flares typically occur above active regions, where the local magnetic field is the most complicated, triggering magnetic reconnection in the corona. The presence of H$\alpha$ emission on either side of the neutral line during the impulsive phase implies that the magnetic field is closed (a loop), which arches over the neutral line, typically from one sunspot, pore, or region of plage, to another of opposite polarity (Golub & Pasachoff 2013). Although, this H$\alpha$ emission may extend beyond sunspots, into the plage field. It is this information from which the standard model

is based.

There are several stages of the standard model, listed below.

1. An excess of energy is built in the corona through one (or more) of several potential processes (such as photospheric motions or flux emergence);

2. A filament forms, consisting of cool, dense plasma and is suspended by the magnetic field;

3. An instability forms, causing the filament to erupt, sending chromospheric or coronal plasma into interplanetary space;

4. As the plasma is ejected, the unstable field suspending the plasma begins to reconnect to return to a more relaxed state, releasing magnetic free energy for heating and particle acceleration - a solar flare.

This release of plasma is typically described as a coronal mass ejection, and as such, the standard model is a standard model for both flares and CMEs. The main drawback with this model is that it is observed that not all flares are associated with CMEs and vice-versa, these events can occur independent of one another.

Generally a solar eruption is understood to occur as a result of a magnetic instability (in this context, a flux tube instability). Hood & Priest (1979) perform a magnetohydrodynamic stability analysis of a model loop anchored in the photosphere. It is found that slow photospheric motions twist or stretch the coronal loop into a kink unstable state. For a purely force-free field, kink instability was reached when the twist exceeded $3.3\pi$.

## 1.5 Magnetohydrodynamics

Magnetohydrodynamics (MHD) is the study of how a plasma behaves in a magnetic field, and is fundamental in our understanding of how a magnetised fluid interacts

and evolves. Although the work carried out in this thesis is mostly observational, a basic knowledge of MHD is required to understand the implications of the results presented in chapters 3-6. As such, the basic equations of MHD will be covered here, as well as some background regarding helicity.

## 1.5.1 The Basic Equations of MHD

A simplified form of Maxwell's equations are used in conjunction with Ohm's Law to describe the behaviour of a continuous plasma. The simplified Maxwell's equations are stated as follows,

$$\nabla \times \mathbf{B} = \mu \mathbf{j} + \frac{1}{c^2} \frac{\partial \mathbf{E}}{\partial t}, \tag{1.1}$$

$$\nabla \cdot \mathbf{B} = 0, \tag{1.2}$$

$$\nabla \times \mathbf{E} = -\frac{\partial \mathbf{B}}{\partial t}, \tag{1.3}$$

$$\nabla \cdot \mathbf{E} = \frac{\rho}{\epsilon}, \tag{1.4}$$

where $\mathbf{B}$ is the magnetic induction, $\mathbf{E}$ is the electric field, $\mathbf{j}$ is the current density, $\mu$ is the magnetic permeability, $\rho$ is the charge density, and $\epsilon$ is the permittivity of free space (Priest 2014).

Ohm's Law is used to describe the current density, and asserts that it is proportional to the total electric field, and is given by

$$\mathbf{j} = \sigma(\mathbf{E} + \mathbf{v} \times \mathbf{B}), \tag{1.5}$$

where $\sigma$ is the electrical conductivity, and $\mathbf{v}$ is the velocity of the plasma.

By eliminating $\mathbf{E}$ and $\mathbf{j}$ among equations 1.1, 1.3 and 1.5, one can define the induction equation, commonly written as

$$\frac{\partial \mathbf{B}}{\partial t} = \nabla \times (\mathbf{v} \times \mathbf{B}) + \eta \nabla^2 \mathbf{B}, \tag{1.6}$$

where $\eta = 1/(\mu\sigma)$ is the magnetic diffusivity. From the induction equation, the magnetic Reynolds number can be defined by dividing the magnitude of the convective

term, $\nabla \times (\mathbf{v} \times \mathbf{B})$, by the magnitude of the diffusive term, $\eta \nabla^2 \mathbf{B}$. The magnetic Reynolds number is

$$R_m = \frac{l_0 V_0}{\eta}, \tag{1.7}$$

where $V_0$ is the plasma speed and $l_0$ is the length scale.

The induction equation determines the behaviour of the magnetic field relative to the plasma, which depends on whether $R_m \ll 1$ (the diffusive limit) or $R_m \gg 1$ (the ideal limit). The diffusive limit reduces the induction equation to a simple diffusion equation,

$$\frac{\partial \mathbf{B}}{\partial t} = \eta \nabla^2 \mathbf{B}, \tag{1.8}$$

which implies that field variations on a length scale of $l_0$ are destroyed over a diffusion time-scale (Priest 2014). On the other hand, the ideal limit reduces the induction equation to

$$\frac{\partial \mathbf{B}}{\partial t} = \nabla \times (\mathbf{v} \times \mathbf{B}), \tag{1.9}$$

which, in short, implies that the magnetic field is tied to the plasma. This means that both magnetic flux and magnetic field lines are conserved in regions with a high magnetic Reynolds number, and the magnetic topology is conserved.

This has implications for the conditions necessary to trigger solar flares. Flares are powered by the release of energy from the magnetic field as it reconfigures during a reconnection event. The region at the site of reconnection must be dominated by diffusion, to allow the magnetic topology to change. However, on the large scale, the plasma must be dominated by the convective term, which acts to draw the magnetic field lines together. This implies that in regions of solar flare occurrence there is a small diffusive region at the site of reconnection within a largely advective region.

All equations stated in this section are correct for SI units. This is not always the case over the remainder of the thesis, but units will be clarified where necessary.

## 1.5.2 Helicity

Magnetic helicity, as stated in Priest (2014), 'is a topological quantity lying at the core of 3D reconnection'. Magnetic helicity represents the amount of twist and kink of a flux tube (self-helicity) and the linkage between separate flux tubes (mutual helicity). The importance of magnetic helicity in the context of the solar corona was first documented by Heyvaerts & Priest (1984) and Berger (1984). They suggested that having magnetic flux threading the photosphere and rising up into the corona implies that the photospheric dynamics of footpoints (sunspots and pores) feed energy into the corona. In the context of this work, these photospheric dynamics are observed as sunspot rotation. Mathematically, the magnetic helicity in a closed volume $(V)$, bound by a surface $(S)$, is defined as

$$H_0 = \int_V \mathbf{A} \cdot \mathbf{B} \ dV, \tag{1.10}$$

where $\mathbf{A}$ is the vector potential and $\mathbf{B}$ is the magnetic field density. However, in the context of this thesis, only the helicity of flux tubes is considered.

In terms of time-varying magnetic helicity, the rate of change of magnetic helicity is given by

$$\frac{dH}{dt} = -2 \int_V \mathbf{E} \cdot \mathbf{B} \ dV + 2 \int_S \mathbf{A}_p \times \mathbf{E} \cdot \mathbf{n} \ dS, \tag{1.11}$$

where $\mathbf{A}_p$ is a gauge, chosen to satisfy $\nabla \cdot \mathbf{A}_p$ and has $\mathbf{A}_p \cdot \mathbf{n} = 0$. If, now, footpoint motions on the surface are taken into account, the injection or removal of helicity from this motion can be deduced as

$$\frac{dH}{dt} = 2 \int \int (\mathbf{B} \cdot \mathbf{A}_p) v_z - (\mathbf{v} \cdot \mathbf{A}_p) B_z \ dx dy \tag{1.12}$$

in the ideal limit, integrating over the $xy$-plane. The first term accounts for only motions in the $z$-direction, and so accounts for the emergence of magnetic structures carrying helicity through the surface. The second term describes motions in the $xy$-direction, accounting for helicity injection due to motions of the footpoints along the surface (Priest 2014).

Now, considering a plane surface, $S$, threaded by $N$ thin footpoints with flux $\phi_i$, where the motion of the footpoints consists of a translation and a uniform rotation rate of $\omega_i$, the rate of helicity change is given by

$$\frac{dH}{dt} = -\frac{1}{2\pi} \left[ \sum_{i=1}^{N} \omega_i \phi_{m(i)}^2 + \sum_{i=1}^{N} \sum_{j=1}^{N} \dot{\theta}_{ij} \phi_{m(i)} \phi_{m(j)} \right], \qquad (1.13)$$

where $\dot{\theta}_{ij}$ is the time derivative of the angle between footpoints $i$ and $j$ (Berger 1984; Priest 2014). The first term in the equation represents the rotation of individual footpoints, injecting one unit of twist into a flux tube every $2\pi/\omega$ seconds, and the second term is the rate at which footpoints rotate about one another, essentially acting to braid the flux tubes.

The total helicity of a magnetic configuration consists of the self-helicity, $H_s$, of each flux tube due to its own internal twist (representing the first term in equation 1.13), and the mutual helicity, $H_m$, due to the linking of flux tubes (representing the second term in equation 1.13). As sunspot rotation only contributes to the first term, which can be described as self-helicity, and is only dependent upon twist of the footpoint, the second term is assumed to be zero for the purpose of this thesis. Assuming flux tubes are straight with uniform twist, the self-helicity of a flux tube can be calculated based on the twist (sunspot rotation), $\theta$, and the magnetic flux, $\phi$, using the following equation

$$H = \frac{1}{2\pi} \theta \phi^2. \qquad (1.14)$$

This implies, that in a perfect case such as a single straight cylindrical flux tube threading the photosphere, the self-helicity can be calculated by observing the rotation of the sunspot (footpoint), $\theta$. This helicity is transferred into the corona, increasing the complexity of the magnetic field in a localised region.

As well as contributing towards the helicity of a flux tube, twist can act to cause an instability in a loop. In the force-free case, the critical value of twist, above which an instability occurs, is approximately $2.5\pi$ (Hood & Priest 1981).

## 1.6 Observing the Sun

This section will cover a brief history of solar observations (focussing on sunspot observations), from the first observations of sunspots to current space-based missions, with particular emphasis on the SDO and Geostationary Operational Environment Satellite (GOES) missions, which provide the data required to carry out the majority of the work detailed in this thesis.

### 1.6.1 The History of Solar Observations

The first recorded telescopic observations of sunspots were made by Galileo in the early 17th century, although observations of dark markings on the Sun's surface with the naked eye were recorded by the Chinese over 15 centuries prior (Foukal 2013). In 1814, the first spectroscope useful for quantitative analysis was built by J. Fraunhofer, who observed over 500 dark lines in the solar spectrum. Almost 50 years later, Kirchhoff formulated the laws governing line emission from light, leading to advances that now allow the observed lines to be associated with chemical elements.

In 1859, Carrington (1859) reported upon observing 'two patches of intensely bright and white light' on the solar photosphere, near an active region. Carrington later commented at a Royal Astronomical Society meeting that a geomagnetic storm occurred following this event, but he was reluctant to assert any connection between the two phenomena. Following this work, further observations have indicated that a very strong correlation between large sunspot groups and geomagnetic activity does indeed exist (Foukal 2013).

Just after the turn of the 20th century, using the Mt. Wilson telescope, Hale observed vortex-like dark features in the chromosphere (in H$\alpha$) around sunspots, resembling iron filings around a bar magnet. This, coupled with the work undertaken decades earlier by Zeeman (1897), involving the analysis of spectral line splitting due to the magnetic field, led to Hale obtaining some umbral spectra for analysis.

Hale found line-splitting due to magnetic fields in sunspot umbrae, with such fields reaching values in excess of 3 kG (Hale & Nicholson 1938).

Up until the mid 20th century, the solar magnetic field outside of sunspots had not been studied in detail and was poorly understood. However, the development of the photoelectric magnetograph in 1951 led to measurements of a 1-5 G polar solar magnetic field. This field was observed to change in polarity every 11 years, along with the fields of the leading sunspots (Babcock 1961). Leading on from this, a pattern of photospheric magnetic field cells, with widths varying between 20,000 and 40,000 km, was observed in the 1960s with an improved version of Babcock's magnetograph (Foukal 2013).

Also in the mid 20th century, Leighton used the spectrograph at the Mt. Wilson tower to measure periodic velocity signals on the Sun. Leighton, along with his graduate students (Noyes and Simon) were the first to detect the 5 minute oscillation of the photosphere (Leighton et al. 1962). This was interpreted to be a result of standing acoustic waves trapped in resonant cavities below the photosphere in the 1970s by Deubner (1975) and Ulrich (1970) independently.

With the advent of space-based instrumentation, solar observations are now available 24 hours a day, every day, particularly with the launch of the Solar and Heliospheric Observatory (SOHO) spacecraft and its successor, SDO. This opens new avenues of research, allowing the scientific community to study the Sun in more detail than ever before.

## 1.6.2   The Solar Dynamics Observatory

The SDO satellite was launched on 11th February 2010, and began returning science data on 1st May 2010. The satellite is in a circular geosynchronous orbit inclined by 28° about the longitude of the SDO ground station, based in New Mexico (Pesnell et al. 2012). It remains in this orbit such that it is always above the ground station,

and is inclined such that the Sun can be imaged 24/7, barring brief gaps in the occasional eclipse season. The main science goals of SDO are to determine how the Sun's magnetic field is generated and structured, and how the magnetic energy stored in the magnetic field is released into the solar atmosphere.
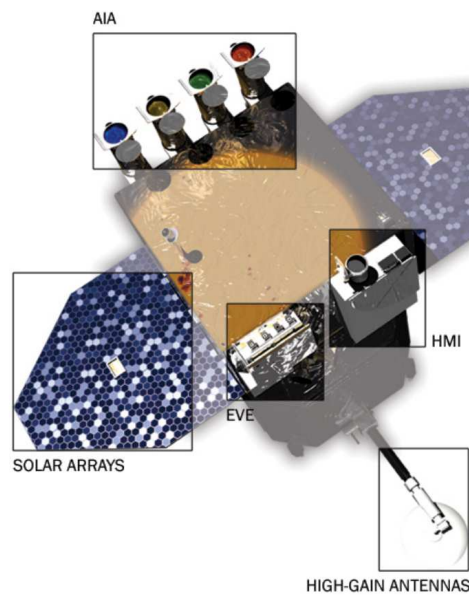


**Figure 1.11:** *The SDO satellite, with all three instruments labelled. Image credit: NASA*

There are three science instruments aboard SDO, the Atmospheric Imaging Assembly (AIA), the Extreme Ultraviolet Variability Experiment (EVE) and the Helioseismic and Magnetic Imager (HMI). For the most part, only HMI is relevant to the work carried out in this thesis, but AIA and EVE will also be briefly described. The location of each instrument onboard the SDO satellite is illustrated in figure 1.11.

The AIA instrument consists of four telescopes that observe the surface and atmosphere of the Sun, and takes 4096 by 4096-pixel full-disc images of the sun with a field of view of at least 40', with a two-pixel resolution of 1.2". Filters on these telescopes cover ten different wavelength bands, seven covering extreme ultraviolet,

two ultraviolet and one visible-light band. AIA produces images of seven out of these ten wavebands with a cadence of 12 seconds (the 1600 Å and 1700 Å wavebands have a cadence of 24 seconds, and the 4500 Å waveband has a cadence of 45 minutes). This allows events to be observed from the solar surface into the solar atmosphere at high spatial and temporal resolutions (Lemen et al. 2012).

The EVE instrument measures fluctuations in the extreme ultraviolet and ultraviolet output of the Sun in wavelength ranges from 0.1 to 105 nm as well as 121.6 nm. EVE provides full-Sun integrated data. There are three components of EVE: MEGS, ESP and SAM. MEGS combines CCDs with grating spectrometers to record spectra in different wavelength ranges. These are combined to obtain the spectrum between 6.5 to 105 nm at 0.1 nm spectral resolution. ESP measures the irradiance in five wavelength bands, ranging from 0.1 to 38.1 nm, using a series of radiometers placed behind a transmission grating. SAM measures individual X-ray photons from 0.1 - 7 nm using a pinhole camera with a MEGS CCD (Schou et al. 2012).

The HMI instrument was built to measure the Doppler shift, line-of-sight magnetic field, intensity and vector magnetic field of the solar photosphere using the 6173 Å Fe I absorption line (Schou et al. 2012). HMI is an instrument known as a filtergraph; it takes a series of images at various wavelengths (in the Fe I line) and polarisations and combines them to derive physical parameters (such as the Stokes parameters used for deriving the vector magnetic field).

This work uses HMI continuum data to calculate the rotation of sunspots, as well as to estimate the area of sunspots, used to derive the flux, and therefore the amount of magnetic energy injected into the solar atmosphere through sunspot rotation. Continuum full-disc 4096 x 4096 pixel images are produced every 45 seconds with a spatial resolution of 0.504 arcseconds per pixel (Schou et al. 2012).

### 1.6.3 The Geostationary Operational Environment Satellite

The GOES satellite has gone through many replacements over the last four decades, from GOES-1 up to the current satellite, GOES-15. X-ray solar irradiance has been monitored nearly continuously by GOES satellites since 1975. GOES measures the total full-disc solar irradiance in in two X-ray wavebands $0.5 - 4$ Å and $1 - 8$ Å. Since the advent of GOES, solar flares have been categorised by their peak flux in the $1 - 8$ Å band. (Donnelly et al. 1977).

## 1.7 Sunspot Rotation

Sunspot rotation in the context of this thesis is defined as the torsional motion of a sunspot about its own umbral centre (figure 1.12). Literature pertaining to sunspot rotation dates back to the early twentieth century. Ever-improving technology and space-based white light imagers have allowed extensive studies of sunspot rotation due to the high resolution and 24-hour coverage of space-based observatories.

This thesis investigates the link between sunspot rotation and flaring activity. From a contextual point of view, as a sunspot is a concentrated area of magnetic flux, any rotation of a sunspot would act to twist a large amount of flux. If it is assumed that sunspots are footpoints of active region coronal loops, sunspot rotation would transfer twist into the active region magnetic field. This twist increases the helicity of the active region, and creates a much more complex active region magnetic field. This leaves the field in a more energetic state, which provides a larger reservoir of energy to be released in the form of solar activity, such as solar flares.

This section outlines the history of sunspot rotation observations, and the advancements in our understanding of the role sunspot rotation plays in solar activity.
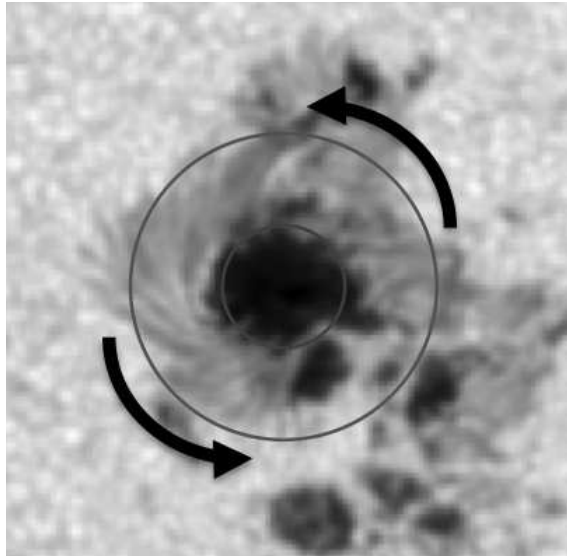
**Figure 1.12:** *The trailing sunspot in AR11158. The solid circles represent the umbral and penumbral boundaries. The arrows indicate the direction of rotation defined as positive (anti-clockwise).*

## 1.7.1 Historical Observations

Rotational motions in and around sunspots were first reported by Evershed (1910) in the form of line displacements in sunspot spectra. With a sample consisting of all large sunspots in 1909, results suggested the presence of radial movement parallel to the solar surface (and about the sunspot's centre) of the material within sunspots, with the velocity increasing as a function of sunspot radius, up to a maximum of around $2 \, \text{km s}^{-1}$ at the edge of the penumbra. This work was followed up by St. John (1913), who confirmed Evershed's hypothesis, and concluded that the line shift was due to the Doppler effect, indicating that the observed effect is indeed a flow of material.

Almost twenty years later, Abetti & Colacevich (1932) found that the velocity of material in different sunspots varied, indicating that there is a significant variation in the physical conditions of sunspots. Maltby (1964) studied 4600 spectra from

62 different sunspots, some from single-sunspot regions, and some from multiple-sunspot regions. The results indicated that multiple-sunspot regions are more likely to exhibit a higher velocity field variance over time than isolated sunspots.

The importance of sunspot dynamics in the build-up and release of energy in solar flares was first discussed by Stenflo (1969), and later, independently, by Barnes & Sturrock (1972). The rotation of the magnetic footpoint of an already twisted flux tube is likely to add twist (but may subtract twist if twisting in the opposite direction to the pre-existing twist) and helicity to the system, increasing the complexity of the magnetic field, and hence the total magnetic energy stored in the field.

With the advent of space-based missions such as TRACE (Transition Region and Coronal Explorer) and SOHO, sunspot rotation was directly observed in white light by Nightingale et al. (2001, 2002). In a more detailed study, Brown et al. (2003) observed seven rotating sunspots that exhibited rotations of up to 200° over periods of 3-5 days. Six of these sunspots were in active regions associated with significant flaring activity, and two of which were associated with soft X-ray sigmoids. Furthermore, Brown et al. (2003) demonstrated that sunspot rotation is unlikely to be a result of differential rotation or projection effects, as the potential contribution of rotation from these effects is an order of magnitude less than the observed rotation speeds.

Following the work carried out by Brown et al. (2003), a significant amount of literature pertaining to sunspot rotation has been published. Several authors have confirmed the rotation values quoted in Brown et al. (2003), as well as the presence of significant flaring activity linked to sunspot rotation, particularly in AR10030 (Li et al. 2005; Georgoulis & LaBonte 2006; Tian et al. 2008).

Sunspot rotation has been calculated using several methods. Brown et al. (2003) use white-light observations, in which an annulus about the sunspot's centre is defined, uncurled, and motions of penumbral features are tracked over subsequent

images. An updated version of the Brown et al. (2003) method is used in this thesis, and is described in detail in chapter 2. The DAVE and DAVE4VM methods on the other hand use line of sight and vector magnetogram data, respectively, to solve the induction equation (equation 1.6) and calculate flows of the magnetic footpoints (Schuck 2006, 2008). Other methods include measuring the rotation of individual penumbral fibrils (Koza et al. 2007), observing and measuring the rotation of pores and fragments in and around sunspot penumbrae (Yan et al. 2009, 2012; Louis et al. 2012) and modelling sunspots as torsional oscillators (Gopasyuk & Gopasyuk 2005; Gopasyuk & Kosovichev 2011).

The cause of sunspot rotation is currently an open question. Some authors observe that sunspot rotation is associated with flux emergence (Tian & Alexander 2008; Yan et al. 2012; Sturrock et al. 2015), possibly indicating that sunspot rotation is the effect of a twisted flux tube emerging through the photosphere. Time-distance helioseismology studies have indicated that the presence of subsurface flows, which appear to be present near regions with rotating sunspots (Jain et al. 2012), may be responsible for sunspot rotation, or perhaps the twisting of flux tubes as they rise through the convective zone (Jain et al. 2015). A substantial amount of work on subsurface flows has also been carried out by Rudi Komm and collaborators, from case studies of the subsurface helicity of active regions (Komm et al. 2015b) to the study of subsurface flows over solar cycles (Komm et al. 2015a).

There are many case studies linking sunspot rotation to a variety of solar phenomena and events. Sunspot rotation has been linked to sigmoid formation, with a prime example being AR10930, a region studied by several authors, some of whom have linked sunspot rotation with sigmoid and flaring activity (Zhang et al. 2007; Yan et al. 2009; Min & Chae 2009; Ravindra et al. 2011; Jain et al. 2012). This region also happens to contain a sunspot with the highest currently observed sunspot rotation value of 540° (Min & Chae 2009). Sunspot rotation has also been linked to

kink instabilities (Srivastava et al. 2010; Török et al. 2013), filament eruptions (Yan et al. 2012, 2015) and coronal mass ejections (Yan et al. 2012; Török et al. 2013; Vemareddy et al. 2016).

## 1.7.2   The Link to Solar Flares

Sunspot rotation has been strongly linked to solar flares, first theoretically by Stenflo (1969) and Barnes & Sturrock (1972), independently. Following Brown et al. (2003) associating sunspot rotation with solar flares, Régnier & Canfield (2006) present an active region, AR8210, in which the slow rotation of a sunspot appears to enable a solar flare by triggering a reconnection process close to a separatrix surface. Tian et al. (2008) observe a large rotating sunspot in AR10030, around which five M-class and two X-class solar flares occurred within a 6-day period. The authors theorise that the source of the sunspot rotation originate below the photosphere, and that the emergence of twisted fields may not always result in sunspot rotation, but still plays an important role in the accumulation of coronal helicity and magnetic free energy. Following these studies, there is a notable increase in the amount of literature pertaining to case studies of sunspot rotation.

Active region 10930 is one of the first to be subject to rigorous sunspot rotation related studies by several authors, in which a sunspot rotates rapidly, by up to 8° per hour, exhibiting a total of 260° rotation over 3 days. This region gives rise to an X3.4 solar flare, which several authors claim is a result of sunspot rotation (Zhang et al. 2007; Yan et al. 2009; Ravindra et al. 2011). Zhang et al. (2007) observe 200° of rotation of the fast rotating sunspot before the X3.4 solar flare occurs. They claim that the interaction between the fast rotating sunspot and the smaller ephemeral regions around the area of the magnetic neutral line is most likely the cause of the flare and associated CME. Yan et al. (2009) observe the rapid rotation of the same sunspot, and using a series of vector magnetograms, find

that the magnetic force lines are sheared along the neutral line accompanying the sunspot rotation. They determine that sunspot rotation twists the magnetic field lines in the photosphere, which can then be transported into the corona, triggering solar flares. Another region of particular interest in the literature is AR11158, a very magnetically complex region that gives rise to over 30 C-class, five M-class and one X-class solar flare. The literature associated with this region will be discussed further in chapter 3, but overall the general consensus from the literature regarding this region is that sunspot rotation is linked to the unusually high amount of flaring activity (Jiang et al. 2012; Su et al. 2012; Vemareddy et al. 2012; Wang et al. 2014).

There have been many other case studies linking sunspot rotation to solar flares. In the majority of studies, the flare is determined to be a result of the rotation (Kumar et al. 2013; Török et al. 2013; Ruan et al. 2014; Vemareddy et al. 2016; Wang et al. 2016). Kumar et al. (2013) associate the flare with sunspot rotation, which in turn they claim is caused by emerging twisted flux. Török et al. (2013) suggest that sunspot rotation triggered a solar eruption by expanding the magnetic field above a filament in AR10898. They test the scenario by twisting an initially potential field over a pre-existing flux rope using zero-$\beta$ MHD simulations. The twisting is found to lead to an expansion of the overlying magnetic field, reducing the magnetic tension and causing the flux rope to slowly rise, eventually becoming unstable. Ruan et al. (2014) observe rapid sunspot rotation (approximately 10° per hour) of a sunspot within AR11283, which is associated with a sigmoidal filament eruption, coronal mass ejection and a GOES X2.1 flare. The sunspot reached peak rotation velocity during a period 6 hours prior to the flare, and the authors claim that this study provides evidence that sunspot rotation plays an important role in providing energy into the corona, as well as destabilising the filament-flux rope system. Vemareddy et al. (2016) use SDO/HMI vector magnetic field measurements and AIA EUV observations to determine that an erupting inverse-S sigmoid was

rooted at the location of a rotating sunspot within AR12158. The authors propose that the slow rotation of the sunspot transforms the flux tube into a highly twisted structure, eventually exceeding the critical twist, causing the flux rope to become unstable and triggering two eruptions. Wang et al. (2016) investigate the X1.4 solar flare associated with AR11520 and its association with sunspot rotation using the differential affine velocity estimator for vector magnetograms (DAVE4VM) method. A high correlation between sunspot rotation speed and the change in the accumulated helicity is reported, and further results by means of a nonlinear force-free field extrapolation indicated that this flare was connected with the sunspot rotation.

Not every study linking sunspot rotation to solar flares determine that the former is the cause of the latter. Wang et al. (2014) observe the X2.2 flare associated with AR11158, and report that during the impulsive phase of the flare, two main sunspots undergo a sudden change in rotational motion. This study only covers a 50-minute duration about the time of the X2.2 flare, and as such does not discuss any potential triggering processes. Liu et al. (2016) observe the differential rotation of a sunspot (up to 50° per hour) following an M6.5 flare within AR12371. The sunspot is observed to rotate clockwise approximately 3.5 minutes following the flare peak time, rotating for approximately 2 hours. The authors do, however, state that this event is distinct from 'almost all previously studied events, where sunspots undergo a rotation before the flare initiation in SXR' (Liu et al. 2016).

It is clear from studying the literature that the vast majority of work pertaining to the effect of sunspot rotation on flaring activity is limited to case studies, and in many cases only one flare or sunspot is analysed, usually over a brief period of time. This work expands on these case studies by undertaking arguably the most complete case study of an active region (AR11158, chapter 3) in the context of sunspot rotation and its association to solar flares. There is also a distinct lack of statistical studies associating sunspot rotation to flares. This thesis contains two

statistical studies, one focused on high flare energy active regions (chapter 4), and one focused on a sample of active regions over a four month period (chapter 5).

### 1.7.3 Helicity Transfer

Regardless as to whether the sunspot rotation causes the flare or vice versa, the rotation of sunspots can be interpreted as a twisting (or un-twisting) of the magnetic flux tube anchored in the photosphere. This implies that there is some transfer of helicity (and therefore magnetic energy) occurring which can be estimated from the rotation of the footpoint. Depending upon the situation, this helicity can either be interpreted as transferring twist into the corona and adding to the potential energy for solar activity, e.g. solar flares, or it can be interpreted as the magnetic field reconfiguring into a less energetic state (essentially implying that energy has been taken out of the corona, and that the rotation of the flux tube is an observable effect of this).

Many authors have associated sunspot rotation with an injection of helicity into the solar corona (Yan & Qu 2007; Zhang et al. 2008; Min & Chae 2009; Srivastava et al. 2010; Ravindra et al. 2011; Jiang et al. 2012; Vemareddy et al. 2012; Ruan et al. 2014; Yan et al. 2015; Wang et al. 2016; Vemareddy et al. 2016). This increase in helicity is observed to result in the formation of sigmoids (Min & Chae 2009; Vemareddy et al. 2012) and filaments (Yan et al. 2015), and in nearly every case, appears to induce, or at least be strongly associated with solar flares.

In one particular study carried out by Kazachenko et al. (2009), 34° of rotation of the leading polarity sunspot of AR10759 was observed over 40 hours. This region then erupted, giving rise to a M8.0 solar flare. Including this rotation in the minimum current corona model acts to triple the modelled helicity and flare energy, bringing the model in line with observations, suggesting that the M8.0 flare is caused by sunspot rotation. This study suggests that a small rotation of just 34° is enough

to provide the majority of the energy required to power an energetic flare event.

## 1.7.4   Sunspot Rotation in Simulations

Although sunspot rotation has been observed many times, to understand the intricacies and implications that sunspot rotation has on flux tubes and the solar atmosphere, several authors have employed simulations. It is encouraging that simulations of sunspot rotation can produce similar results to those seen in observations (Botha et al. 2008). More recent simulations carried out by Sturrock et al. (2015) produce sunspots that rotate by 540° over 40 minutes. Although these values are substantially higher than observed values, follow up work by the same authors suggests that the initial amount of twist of the flux tube dictates the amount of photospheric rotation observed. This implies that flux tubes that emerge twisted will rotate significantly more than those that do not (Sturrock & Hood 2016).

Observationally, sunspot rotation has been associated with helicity injection and sigmoid formation. Sigmoids can be re-produced in simulations by rotating emerged sunspots (Fan 2009; Hood et al. 2012), and in several simulations, the amount of helicity injected from sunspot rotation has been calculated (Fan 2009; Kazachenko et al. 2009; Gordovskyy et al. 2014).

Simulations of rotating sunspots have also led to suggestions that the twist can cause flux tubes rising from sunspots to become kink unstable after as little as 40° rotation (Gibson et al. 2004). Simulations carried out by Fan (2009) suggest that sunspot rotation may be caused by nonlinear torsional Alfven waves along the flux tube, causing the twist from inner portions of the tube to transfer to the outer coronal portion. Selwa et al. (2013) show that the fast rotation of sunspots can trigger EUV waves (large scale wave-like coronal disturbances, generally appearing as broad and diffuse bright features, followed by expanding dimming regions (Moses et al. 1997)) whereas slow rotation does not. This may imply that fast rotation

triggers a more impulsive release of energy, which may take the form of EUV waves or even potentially solar flares. In the simulations carried out by Gordovskyy et al. (2014), sunspot rotation is reported to lead to the triggering of SEP events.

Regarding flaring activity linked to sunspot rotation, Hood et al. (2012) simulate emerging flux tube rotation and associate this with the generation of sigmoids and increased flaring activity. As mentioned in the previous section, Kazachenko et al. (2009) use their minimum current corona model to reproduce observations of AR10759 and find that adding rotation into the picture increases the amount of flare energy available.

### 1.7.5 Statistical Studies

Statistical studies of sunspot rotation is a part of the literature which is relatively lacking. The few studies that have been carried out are documented in this section.

In a study undertaken by Yan et al. (2008a), 182 rotating sunspots are analysed between 1996 and 2007. It was found that there were 12% more rotating sunspots overall in the northern hemisphere, but there was no preference with hemisphere as to the direction of rotation. However, there did seem to be a polarity preference in each hemisphere, with significantly more positive polarity rotating sunspots in the northern hemisphere, and vice versa. Yan et al. (2008b) build on this work by classifying rotating sunspots based on rotation direction and type of rotation (such as torsional rotation which is the subject of this thesis, or rotation of two sunspots about one another).

Upon selecting 20 events (7 X-class and 13 M-class solar flares), Li & Zhang (2009) suggest that a mixture of emergence, sunspot rotation and shear motions of sunspots cause the flare ribbon to sweep across the sunspot (the sample was selected such that only events where the flare ribbon is observed to sweep across the umbra of a sunspot were selected). It is noted that the sunspots in these regions appear to

always rotate prior to the flare event.

Arguably the most quantitative statistical analysis of sunspot rotation was performed by Zhu et al. (2012), in which the DAVE method is employed to analyse a sample of 132 sunspots. Firstly a comparison between the values obtained by Brown et al. (2003) is presented, indicating good agreement between the methods. Out of the sample of 132 sunspots, 82 are seen to emerge, and 50 are analysed post-emergence. Out of the 82 observed to emerge, 63 show a rotation velocity greater than $0.4°\text{h}^{-1}$, whereas only 14 out of the 50 post-emergence sunspots are observed to rotate by $0.4°\text{h}^{-1}$ or more. This strongly indicates that sunspot rotation and flux emergence are linked.

## 1.7.6 Energy Balance

The work undertaken in this thesis is but a small step towards understanding the energy input and output processes at work in solar active regions. Equation 1.7.6 lists the possible input and output processes, of which this work studies one input ($E_{rot}$) and one output ($E_{fl-rad}$) process.

The energy balance regarding solar activity, pertaining to active regions can be expressed simply as $E_{in} = E_{out}$, but when this is broken down into the different possible input and output processes, it can be expressed as

$$E_{rot} + E_{shear} + E_{emerge} + E_{other} = E_{fl-rad} + E_{CME} + E_{c-heat} + E_{other}. \tag{1.15}$$

In terms of input energy: $E_{rot}$ is the energy input from sunspot rotation; $E_{shear}$ is the energy input from shearing motion; $E_{emerge}$ is the energy input from flux emergence; and $E_{other}$ is the energy input from other sources. In terms of output energy: $E_{fl-rad}$ is the energy output from flare radiation; $E_{CME}$ is the energy output from CMEs; $E_{c-heat}$ is the energy contributed to coronal heating; and $E_{other}$ is the energy output through other sources. This thesis explores the link between the input energy, $E_{rot}$, and the output energy, $E_{fl-rad}$ in detail.

## 1.8 Thesis Outline

It is apparent from the literature that photospheric dynamics, particularly sunspot rotation, is linked to solar flares through the injection of helicity into the solar corona. As such, the aim of this thesis is to provide a robust and complete (full disc transit) sunspot rotation study that determines the role that sunspot rotation plays in the onset of solar flares.

Chapter 2 will discuss the analysis techniques commonly used throughout each of the results chapters of the thesis. This includes the technique used to calculate sunspot rotation from white light intensity images as well as the technique used to calculate the flare energy from the radiated energy loss.

Discussed in chapter 3 is the case study of NOAA AR11158. This particularly energetic active region is analysed in detail, from which analysis methods are defined and carried over to two statistical studies presented in chapters 4 and 5. The sunspot dynamics of AR11158 are compared to 'typical' low-energy active regions, allowing comparisons between abnormally high energy regions and regular regions to be drawn. Sunspot rotation results are compared to literature rotation values for this region.

The first of two statistical studies is presented in chapter 4. This is a study of all X-class flaring active regions that have been observed by NASA's Solar Dynamics Observatory, from launch (February 2010) to the present day (March 2017). This analysis provides valuable insight into the dynamics of sunspots in regions that are particularly active, with each one producing at least one X-class flare during its transit across the solar disc.

The second statistical study is presented in chapter 5, in which all active regions present on the Sun between 1 May 2013 and 31 August 2013 are analysed. This removes any bias towards high-energy active regions that was present in chapter 4, allowing a sample of low-energy active regions to also be studied.

CHAPTER 1

The two statistical samples are brought together to highlight the relationship between sunspot rotation and solar flares in chapter 6, where the implications of the results from these samples are discussed.

The concluding section, chapter 7, summarises the results from chapters 3 through 6. This chapter covers the implications of this work and discusses the open questions resulting from it.

# Chapter 2

# Analysis

This chapter describes the method employed to calculate sunspot rotation, sunspot rotation energy, and flare energy. Figure 2.1 shows the process flow of the sunspot rotation calculation, providing a clear overview of the tool.
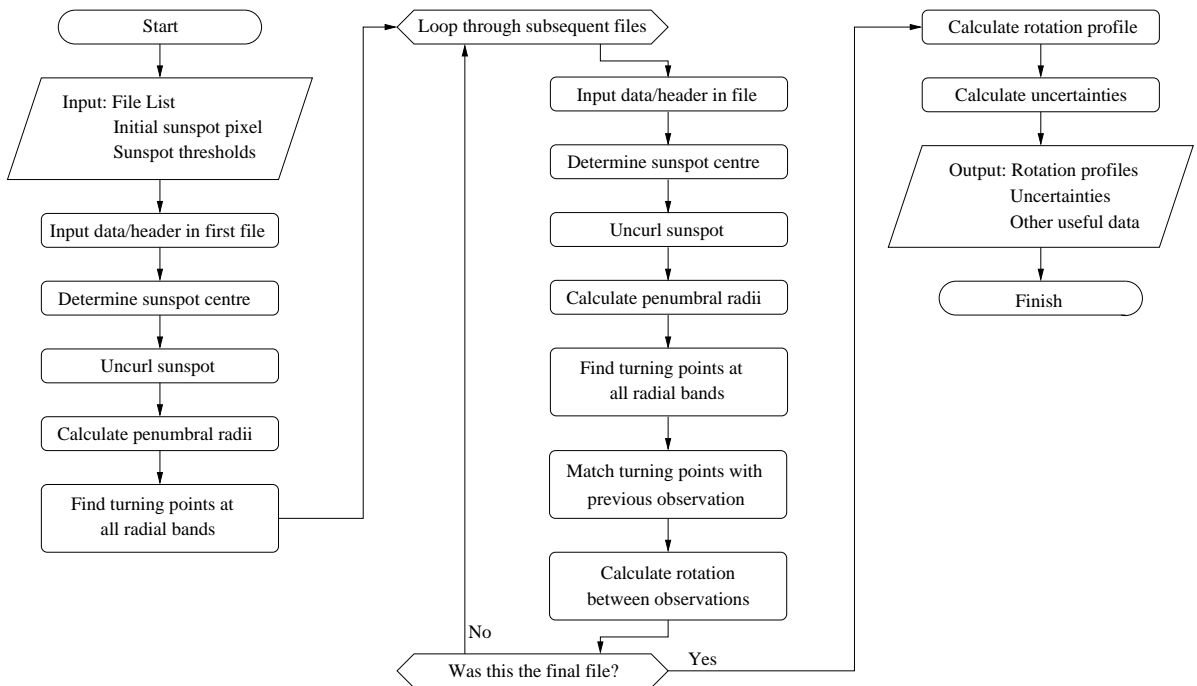
**Figure 2.1:** *Method flow chart of the sunspot rotation calculation tool.*

CHAPTER 2

## 2.1 Data

This method of sunspot rotation calculation uses white light images taken by SDO/HMI. More specifically, data is taken from the `hmi.Ic_45s` data series, which produces continuum images of the Sun's photosphere every 45 seconds from the 6173 Å, FeI absorption line.

As a sunspot may be observed for up to 10 days transiting the solar disc, every fourth image (one image every 3 minutes) is used as this is a reasonable balance between data management and tracking the movement of penumbral features. Sunspot rotation rates typically range from $0 - 3°$ h$^{-1}$ (very rarely above $2°$ h$^{-1}$), corresponding to a maximum rotation of $0.15°$ in a 3 minute period. As such, a 3 minute cadence will easily capture rotation at this rate.

Three criteria are used to determine when to analyse a sunspot. A sunspot cannot be tracked over the full transit, as projection effects reduce the accuracy of the analysis as the sunspot approaches the solar limb. The first criterion is therefore that the sunspot must be between an effective $-60°$ and $60°$ longitude, according to the following equation,

$$\frac{\sqrt{(x - x_c)^2 + (y - y_c)^2}}{R_s} \leq \sin(60°), \tag{2.1}$$

where $x$ and $y$ is the position, on the Sun, of the sunspot centre, $x_c$ and $y_c$ is solar centre, and $R_s$ is the radius of the Sun, all in arcseconds. This means the projected sunspot area is no less than 50% of what it would be at disc centre.

The second criterion is a minimum size criterion of the sunspot under analysis. The pixel-to-degree resolution is low at small radii (see equation 2.5), and so an area limitation on the reprojected area of the umbra of the sunspot is defined. This minimum size is defined based on the radius of an ideal circular sunspot, with a soft limit of 7-pixels (around 2.5 Mm) radius, giving a $49\pi$ pixels$^2$ (around 40 Mm$^2$) area. This radius is around half of the minimum typical sunspot radius quoted by
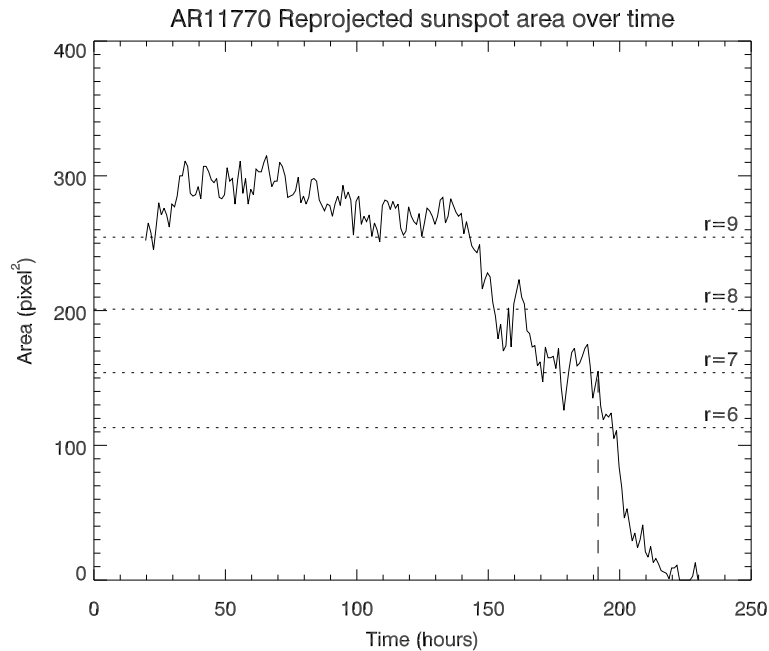
***Figure 2.2:*** *Umbral area of the sunspot in AR11770 over time. Time is measured from the beginning of 14-Jun-2013. The dotted r lines indicate the areas for perfectly circular sunspots with the specified radius (in pixels).*

Thomas & Weiss (2008). If the sunspot's umbral size drops to below this value for up to a few hours before rising back up above it again, then the analysis of the spot is continued. If the sunspot does not rise back above this value then the analysis of the sunspot is terminated as soon as it drops below $49\pi$ pixels$^2$. In cases where the umbral area does drop below the soft limit of $49\pi$ pixels$^2$, a hard limit of $36\pi$ pixels$^2$ (a 6-pixel radius circle) is applied, and the analysis of the sunspot is cut off as soon as the area drops below this value. The third criterion is that the sunspot must remain above the size criteria for at least one day to be considered for analysis.

An example of a sunspot that does drop below this limit is shown in figure 2.2 for AR11770. This spot traverses the solar disc into the analysis area after approximately 19 hours, and has a reprojected area between $250 - 300$ pixels$^2$ for around 145 hours of analysis before beginning to shrink. It then plateaus at around

$49\pi$ pixels$^2$, dipping below this soft limit three times, before finally dropping below
the soft limit permanently at around 192 hours. The vertical dashed line in figure 2.2
indicates the analysis cut-off point in this particular case. This illustrates that in-
cluding the soft limit can extend the analysis period of a sunspot by a significant
amount of time, and is preferable to splitting the sunspot into separate analyses.

## 2.2   Calculating Sunspot Rotation

A brief outline of the sunspot rotation calculation method is included here, with a
more in-depth description following in subsequent subsections.

SDO/HMI continuum data is used to calculate sunspot rotation by comparing
subsequent observations. The images are first corrected for limb darkening (sec-
tion 2.2.1), and then umbral and penumbral pixel count thresholds are determined
(section 2.2.2). The sunspot is then re-projected to disc centre, and an estimate
of the sunspot centre in the initial image is used to calculate the real centre by
employing a centre of mass algorithm (section 2.2.3). This centre is tracked over
subsequent images automatically, using the previous centre as the initial guess for
the next observation (the centre of the sunspot has a proper motion that follows the
spot as it traverses the solar disc). In each image, once the centre is defined, the
sunspot is uncurled about its centre from $x-y$ Cartesian coordinates into $r-\theta$ polar
coordinates (section 2.2.4). Any rotational motion of the sunspot is then observed
as lateral motion in the $\theta$ direction.

To track this lateral motion, the intensity profile of each radial band of the
sunspot is investigated, and local minima and maxima are found (these typically
correspond to fibrils in the penumbra of the sunspot). These are then tracked
laterally in each subsequent image, comparing the angular discrepancy between
the current and previous image, which is used to calculate the amount of rotation
that has occurred in the time between the two observations. Features outside the

penumbra are much less reliable, as they tend not to have a radial structure, and may not be a part of the sunspot (and may not be influenced by the movements within the sunspot).

These calculations are performed for every image (at 3-minute cadence) over the analysis period and are combined to produce a cumulative rotation profile, complete with uncertainty values, for the sunspot.

The only inputs required to carry out the analysis are a sequence of SDO/HMI continuum observations that contain the sunspot (based on the selection criteria in section 2.1) and an approximation of the centre of the sunspot in the first observation of the sequence. Essentially any pixel within the sunspot umbra is a good enough estimate of the sunspot centre.

## 2.2.1 Limb Darkening

Limb darkening introduces issues when it comes to defining the umbral and penumbral intensity threshold, as the sunspot intensity varies as it traverses the solar disc. Towards the edge of the disc, the sunspot centre can no longer be calculated, as limb darkening causes all pixels beyond a certain longitude to be lower than the centre-of-disc sunspot umbra threshold. With the limb correction applied, fixed intensity thresholds can be defined for the umbra and penumbra.

Eighty-two observations taken from 28 June - 6 July 2010 are used to derive the limb correction using a fourth-order polynomial sum. These observations are averaged to remove noise and features such as sunspots that cause intensity fluctuations, and horizontal and vertical slices crossing the Sun's centre are extracted. For an in-depth explanation, see Brown and Walker (2017, in prep.).

Figure 2.3 shows how the limb correction compares to the uncorrected data. This figure shows a full-disc observation in its uncorrected (left) and corrected (right) forms. The plots above each image show the intensity cut along the solar equator,
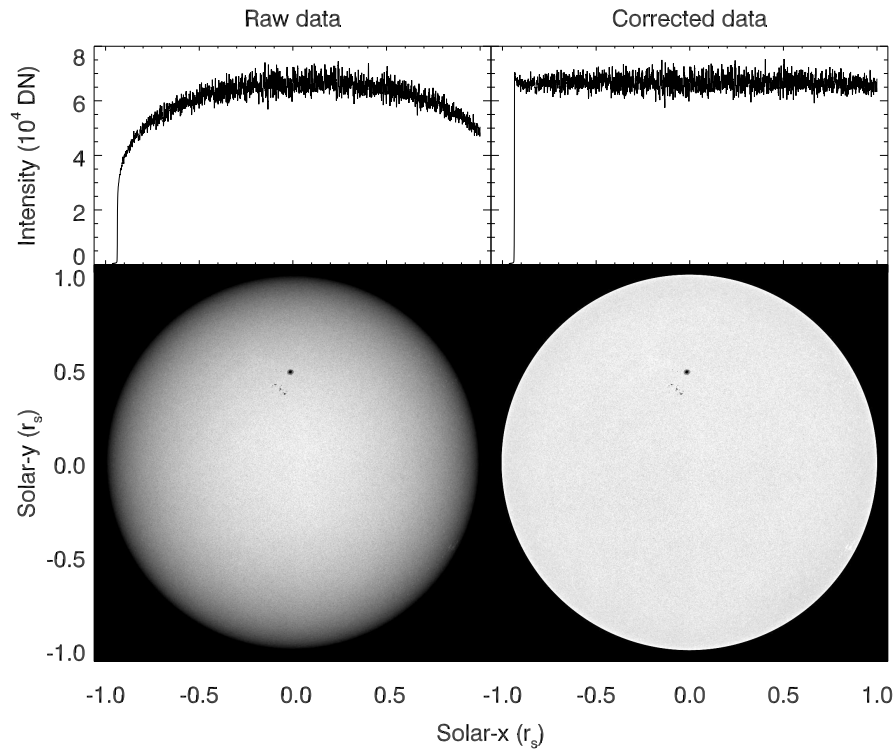
**Figure 2.3:** *The top panels show the intensity fluctuation along the solar equator. The left-hand-side panels show HMI data without limb correction, and the right-hand images show the limb corrected data. It can be seen that the limb correction maintains small-scale intensity fluctuations.*

and the effects of limb darkening can be seen clearly in the raw data plot. The corrected data intensity plot indicates that the correction has eliminated the large-scale intensity variation caused by limb darkening, whilst retaining small-scale variation due to photospheric features.

## 2.2.2 Defining Umbral and Penumbral Pixels

The analysis requires umbral and penumbral intensity thresholds, particularly for calculating the sunspot centre and tracking the sunspot as it traverses the disc, as well as calculating the penumbral size of the sunspot throughout the analysis. These

thresholds are obtained by extracting the `DATAMEAN` value (for the uncorrected data) from the FITS header of each image in the sequence and taking the average of these values:

$$\bar{I} = \frac{1}{N} \sum_{i=1}^{N} \texttt{DATAMEAN}_i, \tag{2.2}$$

where $N$ is the number of observations in the sequence and `DATAMEAN` is the mean pixel value of the FITS image, extracted from the image header.

This is multiplied by two scale factors to produce the following pixel thresholds (these factors are determined by examination of intensity profiles of several sunspots):

- Umbral pixel: $I_{pix} \leq 0.6\bar{I}$;

- Penumbral pixel: $0.6\bar{I} < I_{pix} \leq 1.05\bar{I}$.

These thresholds are generally in the range of $29,000 - 34,000$ DN for the umbra and $51,000 - 59,000$ DN for the penumbra. A minimum threshold of 1000 DN is also applied to ensure that off-limb and bad pixels are not detected as umbral pixels. The use of the `DATAMEAN` compensates for the long-term decline in sensitivity of observations due to the degradation of the instrument.

## 2.2.3   Finding the Sunspot Centre

The sunspot centre is found using limb corrected data, using the centre location of the sunspot from the previous observation as an initial estimate for the new observations. The user-input sunspot centre estimate is used for the first observation.

At the beginning of the centre-finding process for each image, the initial guess of umbral centre is checked. If the intensity value is not below the umbral threshold, then the nearest umbral pixel is used as the initial estimate prior to the employment of the centre-of-mass finding algorithm.
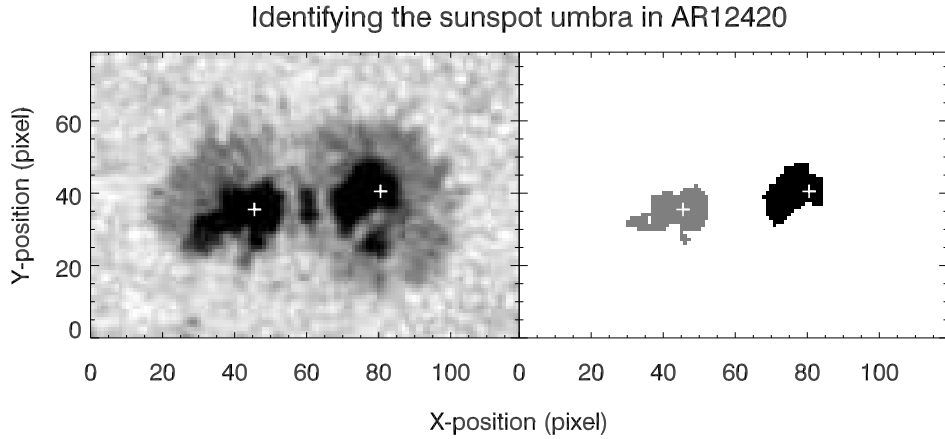
**Figure 2.4:** *The left panel shows limb-corrected HMI data with initial centre estimates, denoted by the white plus symbols, for each sunspot in AR12420. The right panel shows the grouping algorithm defining the sunspot umbrae based on the intensity thresholds.*

The neighbouring pixels of the start point are examined to determine whether they are also umbral pixels, these pixels also have their neighbours tested and so on until the edge of the umbra is found. Figure 2.4 illustrates two sunspots within the active region AR12420, with the left-hand image showing the reprojected SDO/HMI continuum image and the right-hand image showing a map of the identified umbrae of the two sunspots, calculated using the method described. This shows that the umbrae are picked out from the initial estimate without including the other sunspot or pores.

The centre of the sunspot is taken to be the mean location of the group of umbral pixels. So if the identified umbral pixels have locations given by $(x_k, y_k)$ where $k = 1, ..., N$ with $N$ being the number of pixels in the group, then the centre positions, in pixels, of the sunspot $(x_{cen}, y_{cen})$ are given by

$$x_{cen} = \frac{1}{N} \sum_{k=1}^{N} x_k, \qquad \text{and} \qquad y_{cen} = \frac{1}{N} \sum_{k=1}^{N} y_k. \qquad (2.3)$$

These have standard deviations $\sigma_x$ and $\sigma_y$, and standard error on the mean of

$$S_x = \sqrt{\frac{\sigma_x^2}{N} + \frac{\delta_x^2}{12}} \qquad \text{and} \qquad S_y = \sqrt{\frac{\sigma_y^2}{N} + \frac{\delta_y^2}{12}}, \tag{2.4}$$

where $\delta_x$ and $\delta_y$ are the basic quantised scale error of 1 pixel and are assumed to follow a uniform distribution. The $\frac{\delta_y}{12}$ term is taken to be a scale error and takes its form from the variance of the uniform distribution (Barlow 1989). The spatial location of the intensity minimum in a sequence of pixels is taken to be the mid-point of the pixel with the minimum intensity. However, the (unknown) sub-pixel intensity profile may have its minimum located anywhere within the pixel, and as this profile is unknown, it is assumed that the probability of the minimum falling at any given location is uniformly distributed throughout the pixel. Hence, the underlying uncertainty associated with the scale error is taken to be the standard deviation of the uniform distribution over 1 pixel.

From this, a characteristic error of the location of the centre of the sunspot can be calculated, which reasonably approximates the individual errors. This is $S_x = S_y = 0.5$ pixels (Brown and Walker (2017), in prep.), and can be used to estimate the effect of the uncertainty in determining the centre location of the sunspot on the final rotation profiles. It turns out that the size of the sunspot does not affect the error significantly, but its deviation from being circular (ellipticity) does, and 0.5 pixels covers a reasonable degree of ellipticity, representing a spread more typically seen in sunspots.

### 2.2.4 Uncurling the Sunspot

Following the calculation of the centre of the sunspot, the $x - y$ clip containing the sunspot is transformed to the polar $r - \theta$ frame about the sunspot centre, where $r$ is the radius from the centre of the sunspot and $\theta$ is the anti-clockwise angle about the centre. The sunspot is uncurled from a westward pointing chord, using only limb-corrected SDO/HMI data.

(a) Original sunspot position    (b) Longitudinal transformation    (c) Latitudinal transformation
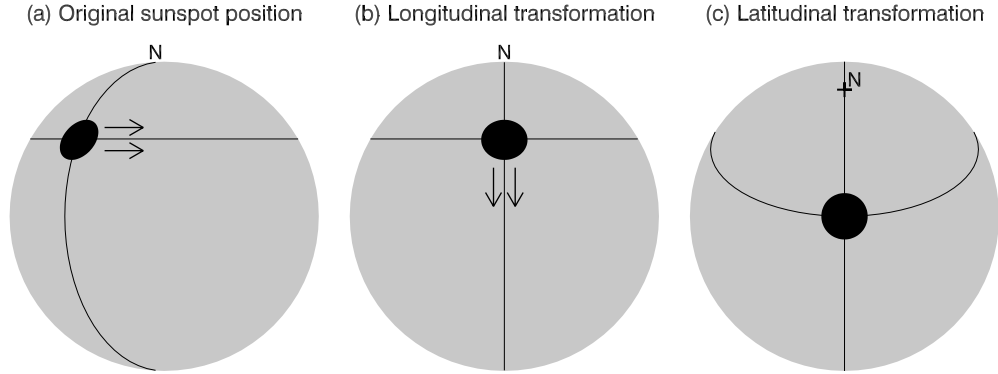
**_Figure 2.5:_** _Re-projection to disc centre: (a) the sunspot is mapped onto the surface of a sphere the size of the Sun, (b) this is rotated about the north-south axis to transform the sunspot to the central meridian, (c) this is in turn rotated about an east-west axis to transform the sunspot to disc centre._

Although limb darkening is accounted for, projection effects are present when the sunspot is near the solar limb. These are removed by transforming the sunspot to disc centre using spherical rotations that preserve solar north, as shown in figure 2.5. The sunspot image is mapped to a sphere the size of the Sun, and rotated about the north-south followed by the east-west axes to transform the sunspot's location to disc centre.

In practice, it is more useful to perform these steps in reverse, i.e., define a series of $r - \theta$ locations about disc centre and convert these to Cartesian coordinates at the sunspot. The spherical rotations are calculated using the position of the centre of the sunspot relative to solar centre, $(x_{cen}, y_{cen})$, via their longitudinal and latitudinal positions.

The resolution of the $r - \theta$ plots is chosen to be 1 pixel in the radial direction and $1°$ in the angular direction. The full $360°$ is sampled in $\theta$, but the range of pixels defining the annulus is chosen in $r$. A 5-pixel radius is defined as the minimum limit, as at this radius the resolution of the resulting ring in the $r - \theta$ plot is very poor (as $10\pi$ pixels need to be converted into a $360°$ circumference). A maximum radius
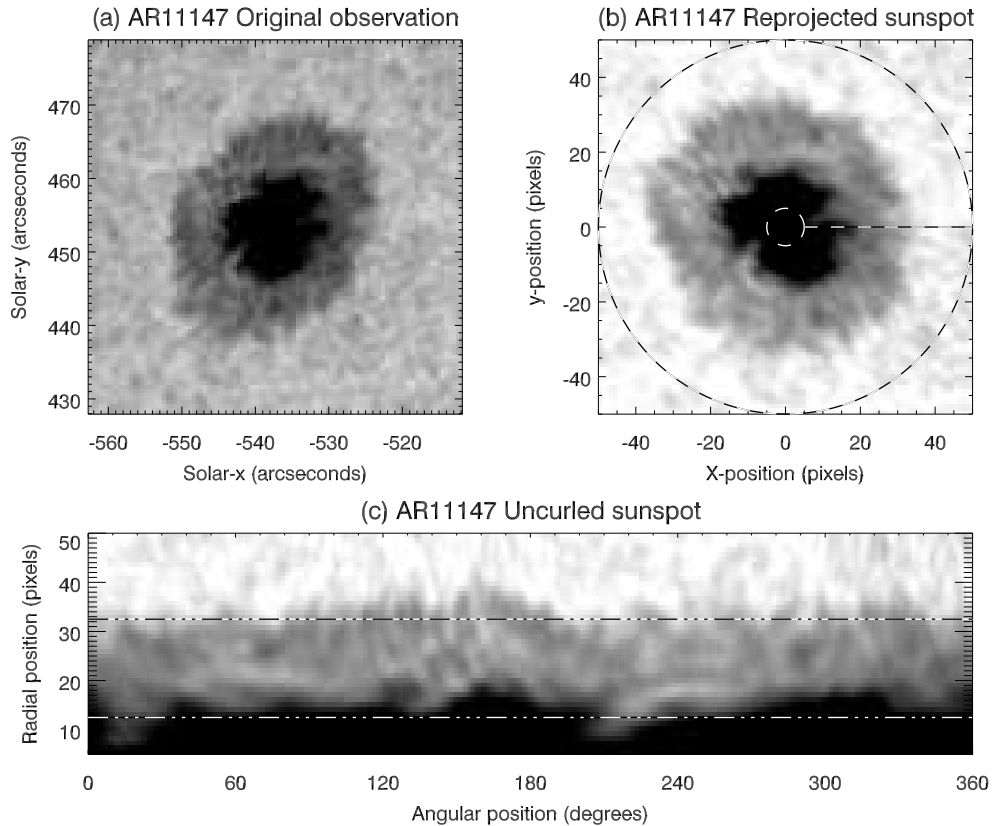
**Figure 2.6:** *Example from AR11147 showing the effect of reprojecting and un-curling a sunspot: (a) the non limb-corrected HMI image of the sunspot which in this observation has its centre located at N38 E28; (b) the limb-corrected and reprojected sunspot, the overlying annulus shows the region to be uncurled (anti-clockwise from the horizontal chord); (c) the uncurled sunspot, with horizontal dot-dash lines indicating the refined penumbral annulus.*

is defined such that the penumbra is completely contained within the sunspot.

The re-projection to disc centre and uncurling of sunspots have consequences regarding the resolution of the sunspot post-processing. The re-projection to disc centre does not have a very large effect, as the longitude limit for analysis is $-60°$ to $60°$, which results in a loss of half of the sunspot area, but the majority of the analysis is performed closer to disc centre. The uncurling of the sunspot does cause

a significant resolution loss following pixel re-binning, particularly at smaller radii. Very small radii (such as the 5-pixel lower limit) can have as many as 12° mapped to one pixel. This is where the main source of uncertainty in the analysis arises.

The size of the annulus is defined in each observation, chosen based on the size of the penumbra. The penumbral pixel intensity threshold is used to determine the number of penumbral pixels in each radial band in the $r - \theta$ image, working from the inner radius outward. The lower boundary of the annulus is defined as the region where the proportion of penumbral pixels in a radial band first goes above a quarter. The upper boundary of the annulus is defined as the radius at which the proportion of penumbral pixels first drops below a half. These different proportions are selected to take into account for different features at each location. The inner umbral/penumbral boundary uses a lower threshold as features such as fibrils and partial light-bridges may be present. The higher threshold at the penumbral boundary is defined to eliminate features outside of the penumbra that may not be rotating with the sunspot.

## 2.2.5  Tracking Lateral Motion

Sunspot rotational motion is calculated by tracking the horizontal motion of features in the sunspot's penumbra. Intensity peaks and troughs, corresponding to penumbral fibrils, are tracked over subsequent observations, allowing the angular difference of each feature between each image to be tracked and converted into a rotation value. The peaks and troughs are found using a running 5-pixel window, such that if the centre pixel in this window is a maximum/minimum value pixel, it is defined as a peak/trough. This is shown in figure 2.7; the bottom figures shows a series of slices from a sequence of 200 images, each taken at $r = 22$ pixels from the associated $r - \theta$ plot. The dashed lines correspond to seven slices, shown as intensity versus angle plots in the top panel of figure 2.7, with the (diagonally) vertical lines

showing the tracking of minima and maxima between each slice.
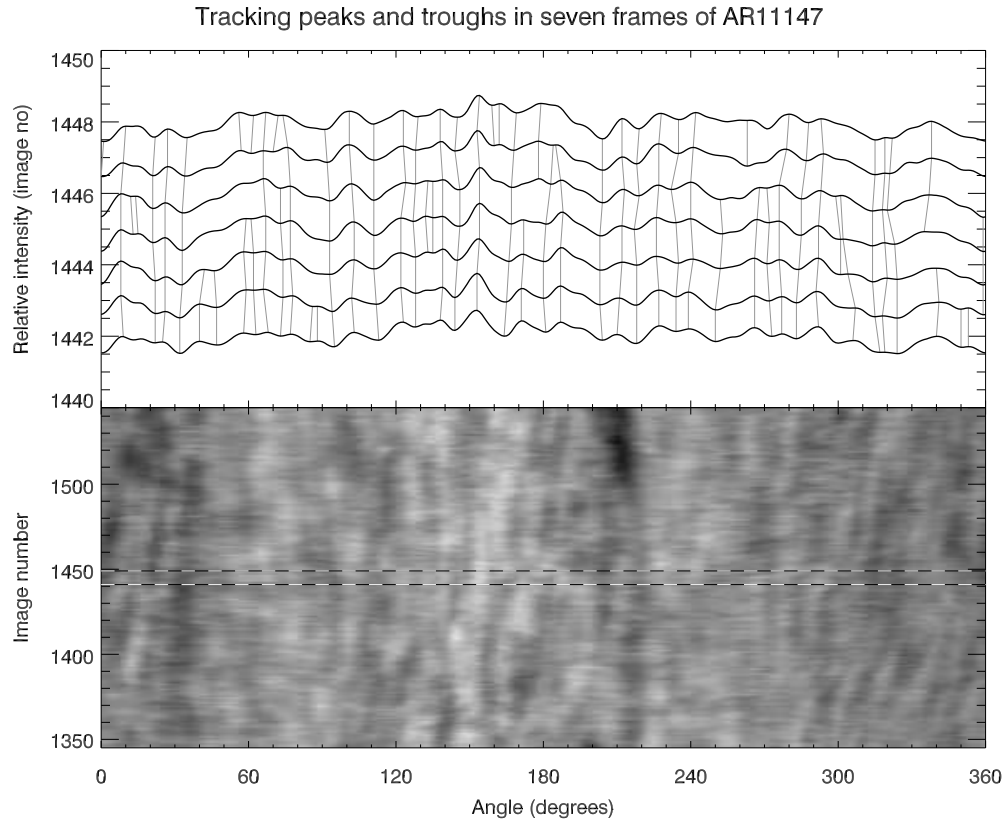


**Figure 2.7:** *Peaks and troughs tracked over seven images for a given radial slice. The lower panel shows stacked radial slices (r = 22 pixels) over 200 observations, with the horizontal dashed lines representing the seven images used in the top panel as an example of how the rotation is tracked. The light and dark streaks in the lower panel indicate the features that are tracked. The vertical and diagonal lines in the top panel represent the tracking of these features by the analysis tool, which is used to calculate the rotation of the sunspot. Peaks and troughs are tracked over subsequent images, until the feature ceases to exist.*

Presented below is a plot equivalent to the the lower panel in figure 2.7, showing a more convincing case of sunspot rotation for the trailing sunspot within the active region AR11158.

**r = 20**
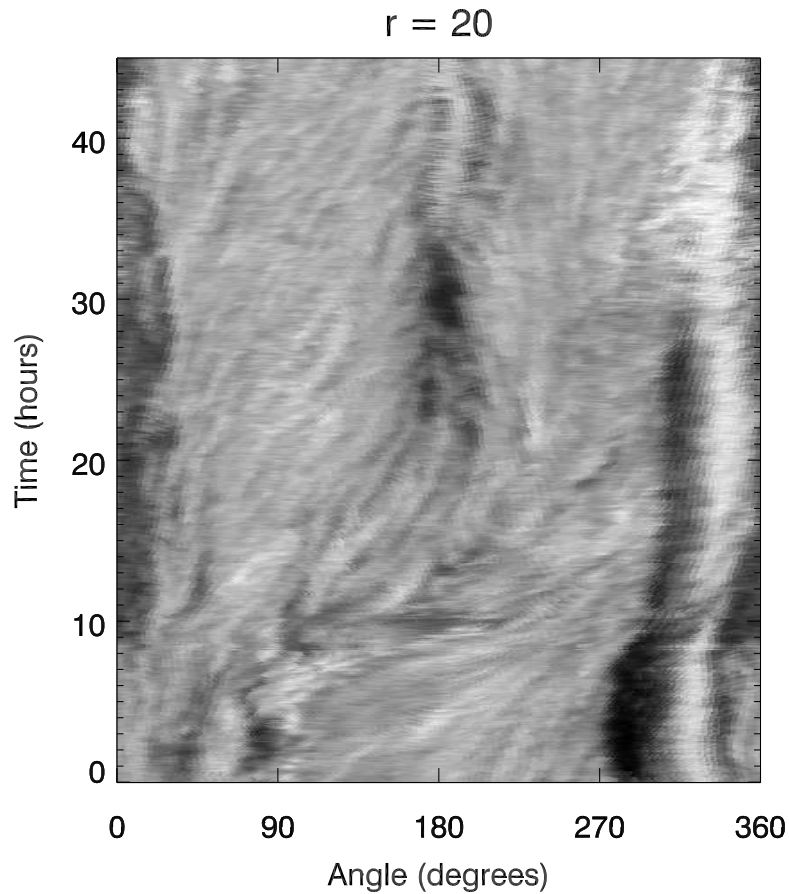
***Figure 2.8:*** *Stacked images of constant radius (r = 20 pixels) of the trailing sunspot within the active region AR11158 over an analysis period of approximately 45 hours. Sunspot rotation can be observed in the form of diagonal streaks.*

As mentioned in the previous section, the conversion from the $x - y$ frame to the $r - \theta$ frame requires different pixel circumferences (depending on radius) to be converted to degrees. A boxcar smoothing with a width of 5 pixels is applied to reduce noise, and a periodic boundary is applied so the boxcar smooths across the $0°$ and $360°$ boundaries. A 5 pixel window centred on an angular location is analysed, and if the maximum/minimum intensity value is within this window, it is designated as a turning point. This is refined by fitting a quadratic to the profile at the point and its immediate neighbouring pixels, and finding the turning point of

CHAPTER 2

the quadratic.

Once all turning points for each radial location have been found for an observation, they are compared to the turning points of the previous observation and are matched if the following conditions hold true:

1. The two turning points are of the same type (i.e., match peaks with peaks and troughs with troughs);

2. The time between the two observations is less than 10 minutes (to allow for the occasional gap in observation sequences);

3. The two turning points are on radial bands of the same radius;

4. The angular positions of the two turning points are within $\pm 3°$ of each other.

Not all turning points must be matched. A penumbral fibril may dissipate over time, and as such its related peaks or troughs would merge and disappear.

There are two scale errors associated with sample scales in the data, assumed to be uniformly distributed. The first scale error arises from sampling the data into $360 \times 1°$ bins, giving a scale of $\delta_1 = 1°$. The second scale error occurs as a result of sampling from the original image. The basic scale of the image is 1 pixel, which must be converted into degrees. The conversion factor depends on the radial position, such that a small radial slice will produce a small ring with a smaller pixel extent and vice versa. The conversion factor can be estimated by dividing the angular size of the ring by the circumference of the ring in pixels, giving the scale

$$\delta_2 = \left( \frac{360}{2\pi r} \text{ ° pixel}^{-1} \right) \times 1 \text{ pixel} = \frac{360}{2\pi r}°. \tag{2.5}$$

The second scale error is larger than the first when $r < 58$ pixels. This is the case for the majority of sunspots in SDO/HMI (for example, the sunspot in figure 2.6 has a penumbral range from around $15 - 30$ pixels), and in these cases the second scale error will dominate. This justifies not sampling at a higher resolution (e.g.,

$720 \times 0.5°$ angular bins) when uncurling the sunspot as this reduces the first scale error but does not affect the second.

A weighted average over all angular and radial locations is calculated to obtain a characteristic rotation for the sunspot at a given time. The refined annuli calculated based on the penumbral size are applied to restrict the calculation to penumbral rotations. To reduce noise brought about by the change in annulus size, an average of the penumbral radii from frames taken within $\pm 30$ minutes from frame $n$ is calculated, along with its associated standard deviation. The size of the annulus can vary significantly over the lifetime of the sunspot as the penumbra may deform, but it typically does so on time scales greater than $\pm 30$ minutes.

Finally, a cumulative rotation profile over the observed lifetime of the sunspot is calculated (figure 2.11), along with an associated cumulative error, by summing the calculated rotation between observations.

## 2.3 Uncertainties Associated with Rotation

The uncertainties in the calculation of the rotation originate from three main sources: the cumulative error (described above), the penumbral error and the centre error. This section discusses the penumbral and centre errors, and the contributions of each individual error on the total error on the cumulative rotation profile.

### 2.3.1 Uncertainty Associated with Varying Penumbra Size

Introducing the varying annulus size to account for the ever-changing penumbral size and the associated running averages introduces additional uncertainties, as the portion of the sunspot being analysed may vary over the analysis period. A series of cumulative rotation profiles are generated for annuli slightly perturbed by $1-2\sigma$ from the running average calculated in the analysis. These alternate penumbral annuli are

used to calculate the rotation profiles as described in section 2.2.5, and the residuals between these perturbed profiles and the original profile are calculated.

A weighted average of the residuals is taken and used as the characteristic uncertainty associated with the penumbral annulus.

This uncertainty is typically larger in sunspots that deviate from being circular. Typical uncertainties from the varying penumbral size are of the order of 0.5° for close to circular sunspots, but may rise to upwards of 5-6° for highly elliptical sunspots (Brown and Walker, 2017, in prep.).

## 2.3.2 Uncertainty Associated with Calculating the Sunspot Centre
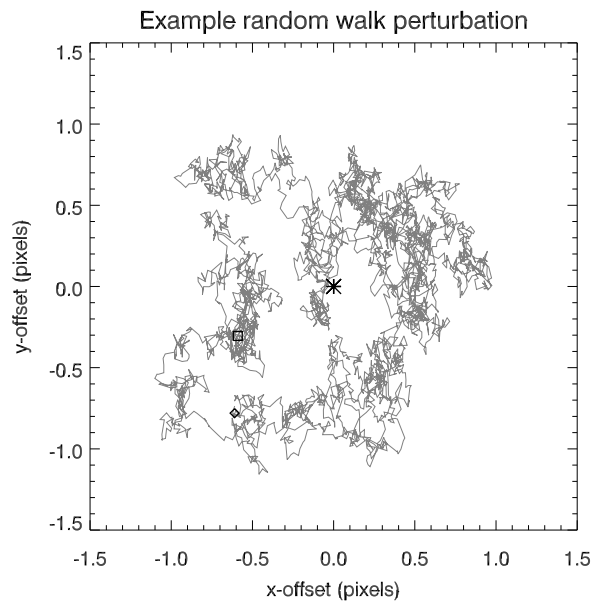


***Figure 2.9:*** *Example of a random walk about the sunspot centre. The asterisk marks the sunspot centre, the diamond the start of the random walk, and the square the end of the random walk. This particular random walk comprises 4000 steps.*

To evaluate the errors associated with calculating the centre position of the

sunspot, a Monte-Carlo approach is employed, using a random walk about the calculated centre of the sunspot, so the sunspot rotation is calculated using a sunspot centre deviated by the random walk. A cumulative rotation profile is generated using the method described above, but using each perturbed sunspot centre instead. This profile is interpreted as being a $1\sigma$ deviation from the unperturbed cumulative rotation profile. A series of cumulative rotation profiles are generated from a set of different random walks, and the residuals between these and the unperturbed profile are calculated. The characteristic uncertainty due to the error on the centre of the sunspot is then taken to be the average of the residuals over the different random walks. Twenty-five random walks are used in the example case to analyse the contribution of the centre error on the total error of the cumulative rotation profile.

The overall error on the unperturbed cumulative rotation profile is taken to be the three error components $(\sigma_{\Theta^n}, \sigma_{p^n}, \sigma_{c^n})$ added in quadrature, i.e.,

$$\sigma_n^2 = \sigma_{\Theta^n}^2 + \sigma_{p^n}^2 + \sigma_{c^n}^2, \qquad (2.6)$$

where $\sigma_{\Theta^n}$ is the error associated with the conversion from pixels to degrees explained in section 2.2.5, $\sigma_{p^n}$ is the uncertainty in the changing penumbral size, and $\sigma_{c^n}$ is the uncertainty due to the sunspot centre. Typical uncertainty contributions from these three main sources of uncertainty are $\sigma_{\Theta^n} = 10°$, $\sigma_{p^n} = 0.5°$ and $\sigma_{c^n} = 1°$.

## 2.3.3   The Overall Contribution of Uncertainties

In this section, the single sunspot active region NOAA 11147 (figure 2.10) is used to demonstrate the contribution from the cumulative error, the varying penumbral size error and the centre error on the total error of the cumulative rotation profile.

Figure 2.10 shows the sunspot within AR11147, with the the intensity profiles of slices through the centre of the sunspot in the x- (top plot) and y-axes (right-hand plot). Intensity thresholds for the penumbra ($59,000$ DN) and umbra ($34,000$ DN)

are indicated by the dotted lines on the intensity profiles. The pixel values at which the intensity value crosses these thresholds are the boundaries of the penumbra and umbra, indicated by the dot-dashed and dashed lines respectively.

Figure 2.11 shows the cumulative rotation of the sunspot within AR11147 over the 200 hours of analysis, with the shaded area representing the total uncertainty associated with the profile. The sunspot rotates by just over 30° anti-clockwise, before rotating approximately 50° anti-clockwise, with a final uncertainty of 11°.
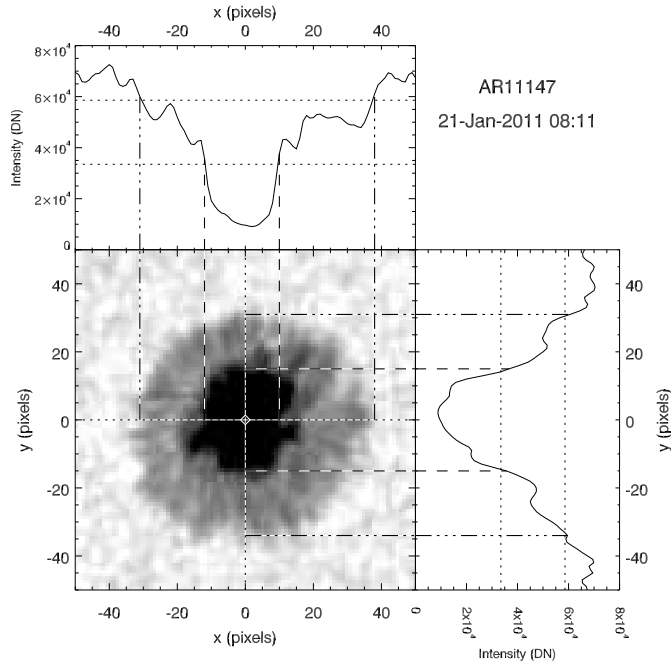


**Figure 2.10:** *A reference image from AR11147 showing the reprojected, limb-corrected sunspot along with intensity profiles in the horizontal and vertical directions through the centre of the sunspot. The defined umbral and penumbral thresholds are plotted on the intensity profiles as dotted lines.*

The errors associated with each method are presented in figure 2.12. These errors have been calculated for several active regions in Brown and Walker (2017, in prep.), but only AR11147 is presented here, as it is the most simple sunspot and illustrates the point effectively.
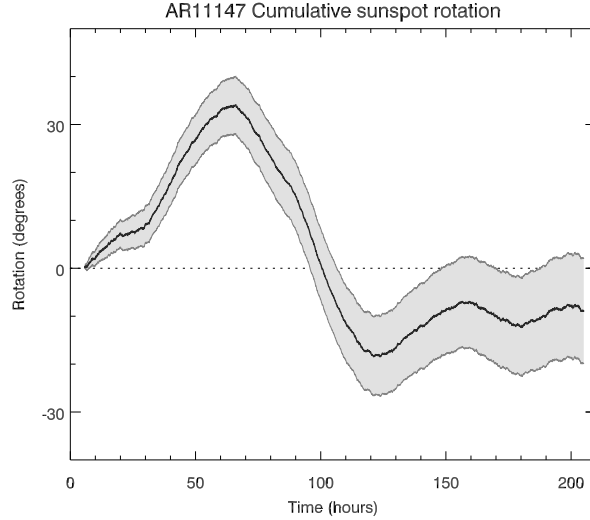
**Figure 2.11:** *Cumulative rotation profile of the sunspot in AR11147 with associated total error. The time axis is measured from the reference time of 17-Jan-2011 at 00:00.*

Overall, the uncertainties associated with the varying penumbral size (figure 2.12(b)) and the uncertainties associated with the calculating the sunspot centre (figure 2.12(d)) are very small compared to the cumulative error. The cumulative error essentially arises from the limiting resolution of small radii in the $r - \theta$ frame, and as such is limited by instrument resolution. In a sense this is reassuring as it suggests that the analysis is robust, with the limiting factor in the analysis arising from the instrument, rather than the method. The breakdown of the relative contributions of the uncertainties is shown in figure 2.12(a) illustrates how the cumulative error is the dominant source of uncertainty in the profile. Figure 2.12(c)) shows a histogram of uncertainties on the error calculation for the sunspot in AR11147. The uncertainty in the sunspot centre rarely rises to above 0.5°, and so its contribution to the overall uncertainty is very small.

The sunspot calculation method is also detailed in Brown and Walker (2017, in prep.), in which the code is tested in both simple and complex active regions. These
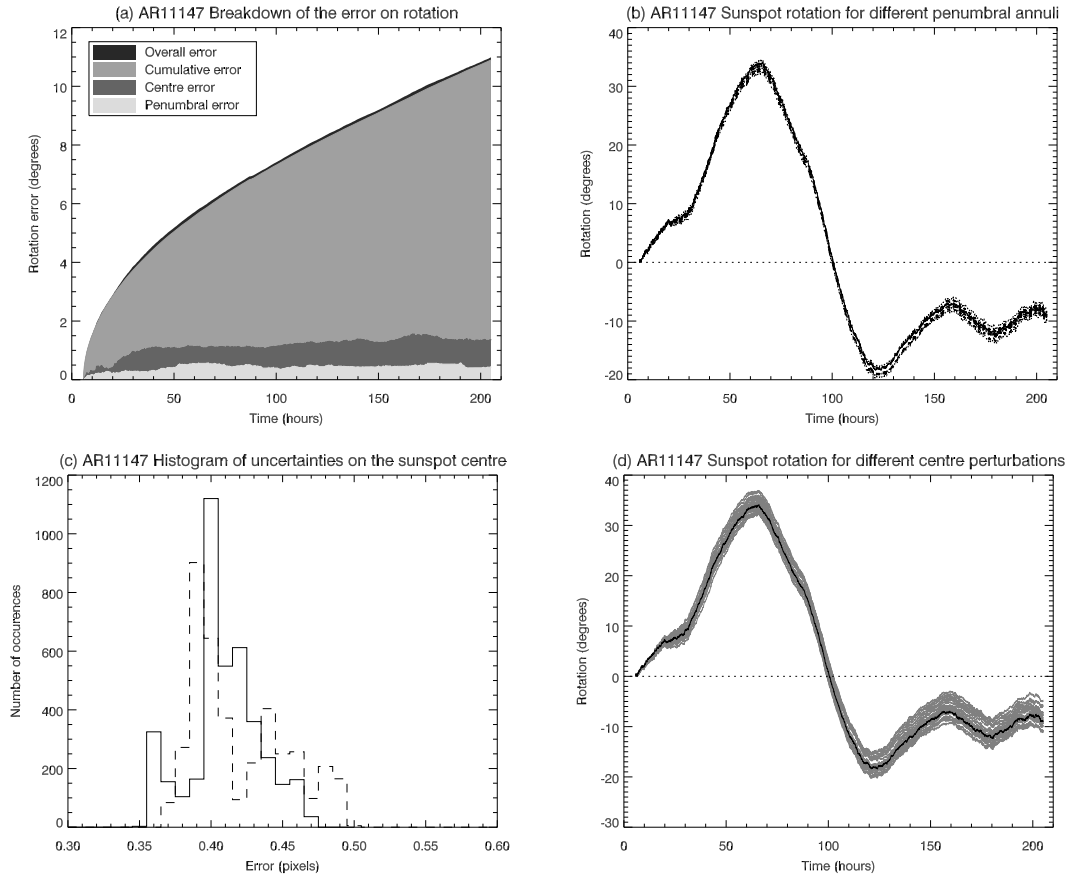
**Figure 2.12:** *(a) Total error and a breakdown of the contributions to the total error from the cumulative error, the error due to uncertainty on the centre of the sunspot, and the error due to variation of the penumbral annuli; (b) Cumulative rotation profiles for the perturbed penumbral annuli; (c) A histogram of the uncertainties on the centre of the sunspot, where the solid histogram lines are the errors in x and the dashed histogram lines are the errors in y; (d) Cumulative rotation profiles for random walk perturbed sunspot centre locations. The time axis in all plots is measured from the reference time of 17-Jan-2011 at 00:00.*

tests confirm that the cumulative error is the dominant error, even in cases containing complex sunspots with largely varying penumbra sizes. Overall the method is robust, and can handle even extremely complicated active regions very well (see chapter 3 - the case study).

As the error contribution from the centre position is so small, the Monte Carlo random walks are not performed in the calculation of sunspot rotation in this thesis, as for each step of the random walk, the computation time dramatically increases.

## 2.4 Solar Flare Integration

One aspect of the analysis that is performed in each piece of work documented in this thesis, along with the sunspot rotation calculation, is the radiated flare energy integration.

### 2.4.1 Radiative Energy Loss

The GOES satellite provides 24-hour X-ray intensity data in the $0.5 - 4$ Å (B4) and $1 - 8$ Å (B8) wavebands. The two-channel GOES data is converted to a temperature and emission measure using relations from White et al. (2005). An optically thin radiative loss rate versus temperature function is taken from the CHIANTI database (Dere et al. 1997, 2009) is inferred from the temperature and emission measure for coronal abundances and Mazzotta et al. (1998) ionisation equilibrium. The optically thin radiative loss rate in erg s$^{-1}$ is based on the following equation, derived by Cox & Tucker (1969),

$$L_{rad} = 10^{49} EM \frac{6 \times 10^{-22}}{(T/10^5)^{\frac{1}{2}}},$$
(2.7)

where $EM$ is the emission measure and $T$ is the temperature. The emission measure should be provided in units of $10^{49}$ cm$^{-3}$ and the temperature provided in Kelvin. This calculation assumes that the hot plasma is isothermal at all times.

The radiative loss rate is then summed over the duration of the flare to give a total optically thin radiative energy loss in ergs. The flaring energy is calculated following background subtraction.

The optically thin radiative energy loss is converted to a radiated bolometric energy loss (in ergs) based on work by Emslie et al. (2012), who analyse 38 X- and M-class solar flares, and calculate the contributions of the flare energy from a variety of sources. Comparing the difference in the total optically thin radiative energy loss and the bolometric radiative energy loss, the bolometric energy loss is, on average, 5.2±2.3 times larger than the optically thin radiative energy loss. Thus, this factor is applied to the optically thin radiative energy loss values to convert them to an estimated bolometric radiative energy loss. The uncertainty arises from the standard deviation of the ratios between the bolometric and optically thin flare radiation for the 38 flares analysed by Emslie et al. (2012). This factor is applied to the optically thin flare energy of each active region, such that we are making the assumption that the flare energy comes from one dominant flare.

## 2.4.2   Defining the Flare Duration

The optically thin flare energy calculation described in the previous section is built into `SSWIDL`, making the flare integration process reasonably simple for individual flares. However, when determining the flare energy for an active region with multiple flaring events, there are factors that complicate the process:

1. GOES X-ray emission data is full-disc, meaning that in particularly active periods, such as solar maximum, contamination from flaring from other active regions may affect the integrated flare energy;

2. In regions that are particularly active, flares may occur in quick succession, meaning a flexible integration time, dependent upon the start time of the following flare, is required.

The first complication can be improved by using the Heliophysics Events Knowledgebase (HEK) to query all flare events associated with the active region under scrutiny. This provides start, peak and end times for each flare associated with that region, as well as flare class. This allows the integration time for each flare to be defined based on these parameters, with the only complication arising when there is another flare from a different active region within the same integration window.

The second complication is resolved by defining the integration end point. The end time acquired from the HEK is the time at which the $1-8$ $\mathring{A}$ flux has dropped to half of the peak flux of the flare. This is not a very good parameter to use for the flare integration end time, as a significant portion of the flux would be missed. Instead, the flare integration ends when the flux either reaches 5% above the background level, or another flare occurs in the same active region. Every flare associated with the active region during the analysis period is integrated, and the energy contribution from each flare is summed and converted into a radiated bolometric flare energy value.

Radiation is not the only form of energy generated by solar flares. Other phenomena such as coronal loop heating, particle acceleration, Alfven wave generation and coronal mass ejections may also be associated with particularly energetic solar flares. As such, the radiated flare energy represents a minimum energy output from flaring.

## 2.5 Sunspot Rotation Energy

To obtain a quantity to compare the calculated rotation to the observed flaring energy more directly, an estimate of the energy contribution from sunspot rotation is calculated. To carry this out, a three-step approach is employed, detailed in this section.

Firstly, the average sunspot area is converted into an average magnetic flux for

the sunspot. The flux value is calculated using the empirical relationship determined by Li et al. (2001), calculated from a sample of over 1000 sunspots and pores, and is given as

$$\phi = 10^{12.17} A^{1.09}, \tag{2.8}$$

where $\phi$ is the magnetic flux in Maxwells, and $A$ is the sunspot area in km$^2$. This relationship is shown graphically in figure 2.13.
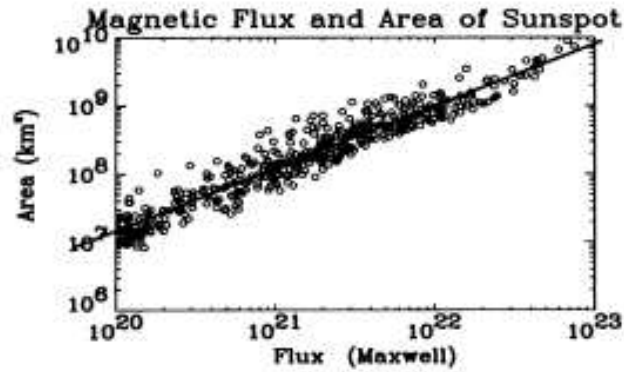


*Figure 2.13:* *Relationship between sunspot area and total sunspot flux. Image credit: (Li et al. 2001)*

The sunspot area is defined by the size of the outer annulus boundary as it traces the penumbral size, as described in chapter 2. An average sunspot size throughout the duration of the analysis is calculated in pixels$^2$. This can be converted to km$^2$ using the accepted value of 725.27 km per arcsecond at 1 AU, combined with the spatial resolution of HMI of 0.504 arcseconds per pixel in both $x$ and $y$, giving a conversion factor of 133619 km$^2$/pixel$^2$. As part of the analysis, this method is validated by using line-of-sight magnetogram data from SDO/HMI to determine the average sunspot flux (from observations close to the solar centre) for the five sunspots in AR11158.

Secondly, as the energy contribution from sunspot rotation is assumed to come from the amount of helicity injected into the corona. As the rotation of a sunspot

is assumed to add to the self-helicity of a flux tube, this is calculated using

$$\Delta H = -\frac{1}{2\pi}\Delta\theta\phi^2.$$

(2.9)

Where $\Delta H$ is the change in helicity due to rotation and $\Delta\theta$ is the total rotation of the sunspot. Although this equation assumes a straight flux tube with a uniform twist, it has been confirmed by Vemareddy et al. (2012) to be a very good estimate, and is consistent with values obtained through more complex methods. The helicity is essentially a flux-weighted measure of rotation. As the helicity is proportional to the square of the flux, a small amount of rotation of a large sunspot will contribute a lot of helicity, whereas a large amount of rotation of a small sunspot may have a lower helicity contribution.

Following the calculation of magnetic helicity from the sunspot rotation and sunspot flux, the last step is to calculate an estimate of the magnetic energy injected. The relationship between magnetic helicity and magnetic energy has been determined empirically by Tziotziou et al. (2012), and is given by

$$|H| = 1.37 \times 10^{14} E^{0.897}.$$

(2.10)

Where $|H|$ is the unsigned helicity and $E$ is the magnetic energy. This relationship is shown graphically in figure 2.14.

Although no uncertainty on the magnetic free energy value is stated, there is substantial scatter, particularly in the X-class flaring regions.
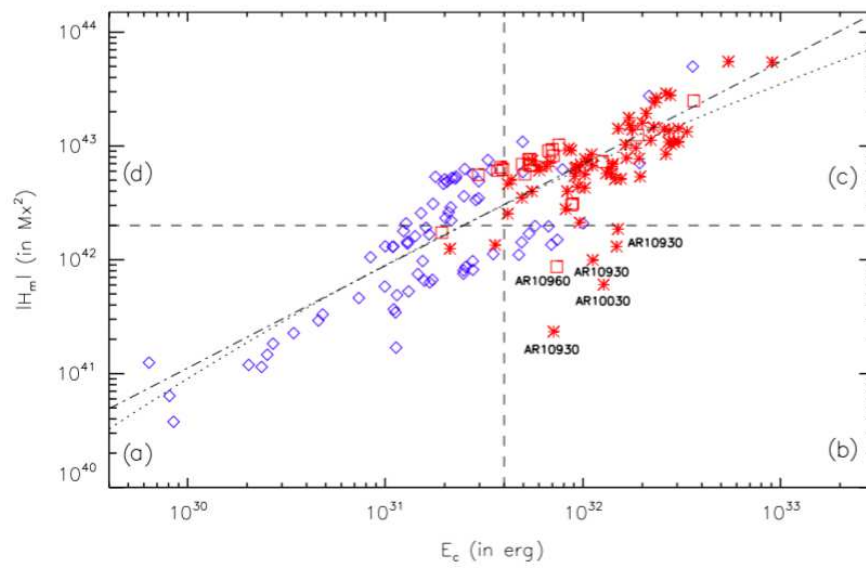
**Figure 2.14:** *Relationship between magnetic energy and helicity used to derive equation 2.10. Each point corresponds to an active region, blue diamonds correspond to non-flaring regions, red squares correspond to M-class flaring regions, and red asterisks correspond to X-class flaring regions. Image credit: Tziotziou et al. (2012).*

# Chapter 3

# AR11158: The Case Study

## 3.1 Context

The case study presented in this chapter uses the analysis tool described in chapter 2 and develops further analysis techniques in preparation for the statistical studies presented in chapters 4 and 5.

NOAA active region 11158 (henceforth referred to as AR11158) is a region which has been subject to much analysis. This region emerged on 11 February 2011, and gave rise to an X2.2 flare, five M-class flares and over 30 C-class flares. Several authors have analysed the rotation of sunspots within AR11158, but in each case, the subject of analysis has been one or two sunspots, generally over a short period of time (most commonly around 15 February, as this is when the X2.2 flare occurred). Table 3.1 lists the literature pertaining to sunspot rotation on this region, illustrating the point. It is clear from this table that there is no case study offering a complete, full-disc transit analysis of every sunspot in this region.

This chapter presents the first complete analysis of the rotational dynamics of an active region, with AR11158 selected as the case study due to both its complex nature and the amount of literature available for comparisons to be drawn. This is the first step in the ultimate goal of determining the relationship between sunspot

**Table 3.1:** *Literature pertaining to the rotation of sunspots within AR11158. This table only includes papers that explicitly analyse sunspot rotation, quoting values of either total rotation or rotation rates. The spot(s) column refers to the spots analysed, defined in figure 3.2, the date(s) column lists the analysis period, the method column refers to the analysis method used and the rotation column refers to either the total rotation value or rotation rate of the sunspots.*

| Paper | Spot(s) | Date(s) | Method | Rotation |
|-------|---------|---------|--------|----------|
| Jiang et al. (2012) | B | 14-15 Feb 2011 | Brown03 | $38 - 107°$ |
| Vemareddy et al. (2012) | B, E | 13-15 Feb 2011 | Brown03 | $110°, 170°$ |
| Wang et al. (2014) | B, D | 15 Feb 2011 01:05-02:45 | DAVE | $3\text{-}37°\ \text{hr}^{-1}$ |
| Li & Liu (2015) | E | 13-17 Feb 2011 | Brown03 | $200°$ |

rotation and solar flare production.

The overall aim of this chapter is to analyse AR11158 using the methods described in chapter 2, and develop further analysis tools to aid in the interpretation of these results. The methods developed in this chapter will be used in a semi-automatic fashion in the statistical analyses that follow (chapters 4 and 5).

## 3.2   Data

The analysis period of AR11158 ranges from 2011-02-12 00:00 to 2011-02-19 23:59, as this covers the emergence of the region and its transit across the solar disc. This time range is refined using the selection criteria listed in detail in section 3.3.2 to determine the analysis period for each sunspot. SDO/HMI continuum images are used at a three-minute cadence to calculate the sunspot rotation. The longitude (-60° to 60°) and size criteria also discussed in chapter 2 are used to determine whether a sunspot is suitable for analysis, as this covers the emergence of the region

and its transit across the disc. The actual analysis period of the sunspot rotation of this region will be shorter, as the sunspots do not reach a size large enough to analyse until around midday on the 12th.

Flare data for this region is obtained primarily through the Heliophysics Events Knowledgebase (HEK), which provides information such as flare class, start time, peak time and end time, as well as an associated active region (Hurlburt et al. 2012). This allows events associated only with the active region of interest to be queried, and from the information provided, a flare integration time can be determined.

Using the information pulled from the HEK in conjunction with GOES $1-8$ Å X-ray data, allows the optically thin radiation of each flare associated with AR11158 to be integrated (over time) individually. As the GOES data is full-disc, integrating the flares separately reduces the chance of contamination from flares from other active regions present on the solar disc at the same time. The optically thin flare energy calculated through this method is converted into a bolometric energy, as described in section 2.4.1 using the conversion factor derived from work undertaken by Emslie et al. (2012).

## 3.3 Analysis

The analysis of the rotational properties and their link to the flaring activity of AR11158 is comprised of three main stages: Sunspot selection; rotation calculation and flare integration, described in chapter 2.

### 3.3.1 AR11158

The full disc image in figure 3.1 is taken at 2011-02-14 00:00. The white box represents the region of the Sun imaged in the strips on the right hand side. Other than the small active region forming in the north-west quadrant of the disc, the Sun is
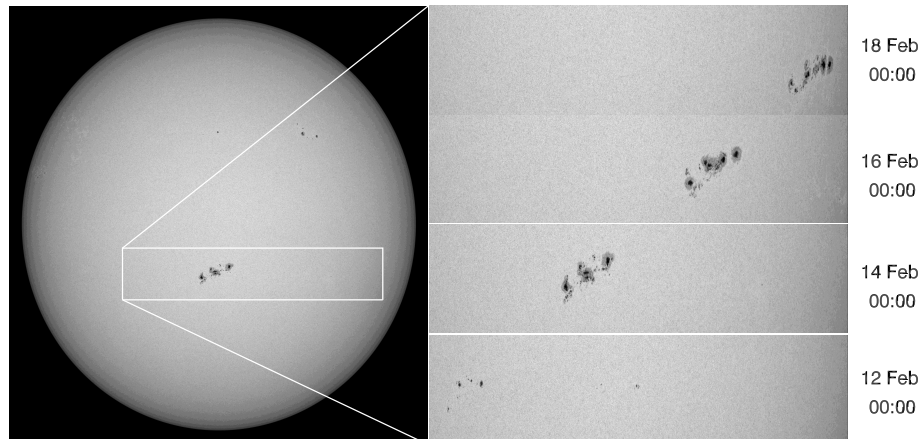
**_Figure 3.1:_** _Full disc image taken 2011-02-14 00:00. The white box on the full disc image indicates the region imaged in the horizontal strips on the right. Strips on the right hand side in ascending order of date show the evolution of the active region over 6 days._

quiet at this time. The strips on the right of figure 3.1 show, in ascending order of time, the evolution of AR11158 as it makes its way across the solar disc, from small, newly emerged spots to just greater than 60° longitude.

AR11158 and its sunspots, referred to as sunspots A-E throughout this chapter, are shown in figure 3.2, with the sunspots labelled from leading to trailing. This active region emerged at solar coordinates S19E11, on the 11th February 2011, with a $\beta\gamma$ magnetic configuration. Significantly more flux emergence began at approximately 20:00 on 12th February, and the leading sunspot, labelled A, begins to form at 00:00 on the 13th. The two trailing sunspots, E and D, begin to form at approximately 07:00 and 14:00, respectively, on the 13th. Sunspots B and C both form at a similar time, at around 20:00 on the 13th. Figure 3.2 is taken on 14th February 2011 at 00:00, when all sunspots analysed in this work are visible.

Throughout the lifetime of the active region, the sunspots are observed to drift and interact with pores, and in some cases, disperse. Spots A and B survive until

AR11158 snapshot on 2011/02/14 at 00:00
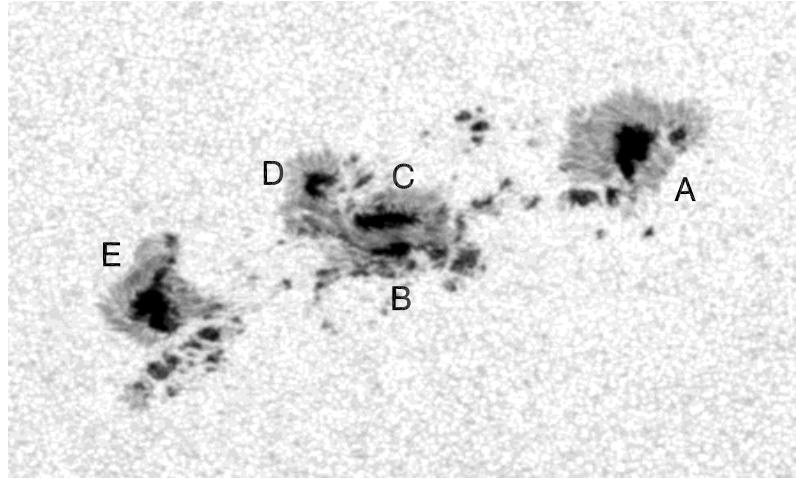


**Figure 3.2:** *NOAA active region 11158 snapshot taken at 2011-02-14 00:00 by SDO/HMI. All five sunspots analysed in this region are visible, labelled A-E from leading to trailing.*

they reach the edge of the western limb, whereas spots C, D and E are all observed to disperse during the transit across the solar disc. Of particular note are spots B and C; B exhibits significant drift, moving significantly closer to A throughout the evolution of the active region, and C interacts strongly with D, leading to a shared penumbra and the formation of a light bridge between the two before D disperses. Sunspots B and C also experience strong shear as they emerge. This emergence and subsequent shearing most likely triggers some flaring activity. On the 16th February 2011, the active region was reclassified to a $\beta\gamma\delta$ region as a result of its magnetic complexity.

### 3.3.2   Sunspot Selection Criteria

In an attempt to remove as much subjective bias from the sunspot selection process as possible, the following criteria are used to determine the analysis period of each

CHAPTER 3

sunspot (the first two of which are described in chapter 2, but are included here for completeness):

1. The sunspot umbra must contain more pixels than a circle of seven-pixel radius. The umbral size may drop to an area with an equivalent radius of between six and seven pixels for a maximum of three hours, before returning to above seven pixels.

2. The sunspot must have an effective longitude of between -60° and 60° for the analysis period, as per equation 2.1.

3. The sunspot must not interact with another sunspot in such a way that interferes with the analysis (sunspot mergers for example). In this case, the sunspot is analysed up to the point of interaction.

4. The sunspot must meet the above three criteria for a period of at least 24 hours.

The umbral size of each sunspot labelled in figure 3.2, and how they vary over time, is shown in figure 3.3. The start and end times, calculated based on the selection criteria, are indicated by vertical dotted lines on the plot. The horizontal dashed and dotted lines represent the umbral area of a seven- and six-pixel radius circle.

The remaining issue lies in that the process is not fully automatic, and as such the location of the sunspot and the starting time from when to calculate the umbral size, must be provided as input before the sunspot rotation can be calculated.

Another issue with the sunspot selection is that in some cases, such as spots B and C in AR11158, the sunspots move so close to one another that their umbrae merge for a short period of time. As a result, the analysis start time of sunspot B has been pushed back by 12 hours, when it stops interacting with C (as per the
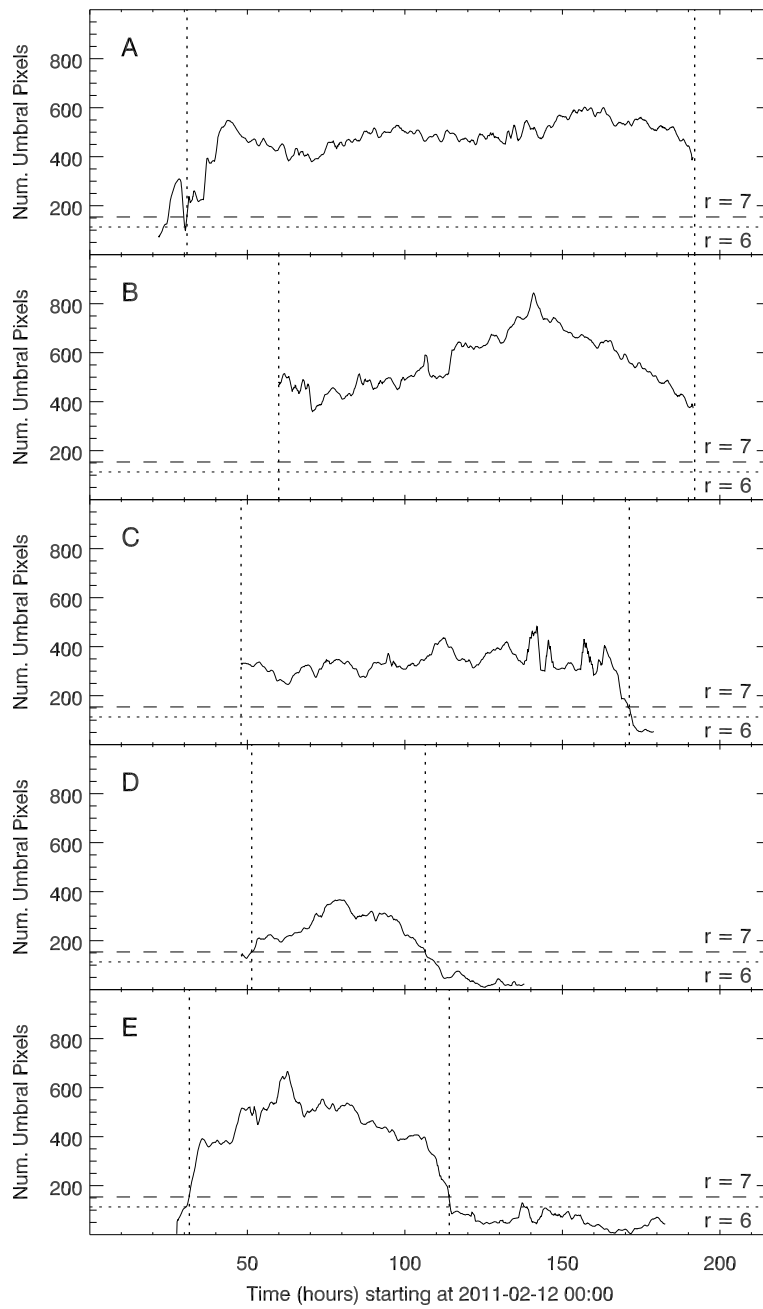
***Figure 3.3:*** *Sunspot umbral areas over time. The sunspot to which the profile belongs is displayed in the upper-left corner of each plot. The horizontal lines indicate umbral areas of circles of six (dotted) and seven (dashed) pixel radius. The dotted vertical lines indicate the start and end time of sunspot analysis based on their umbral size from the selection criteria.*
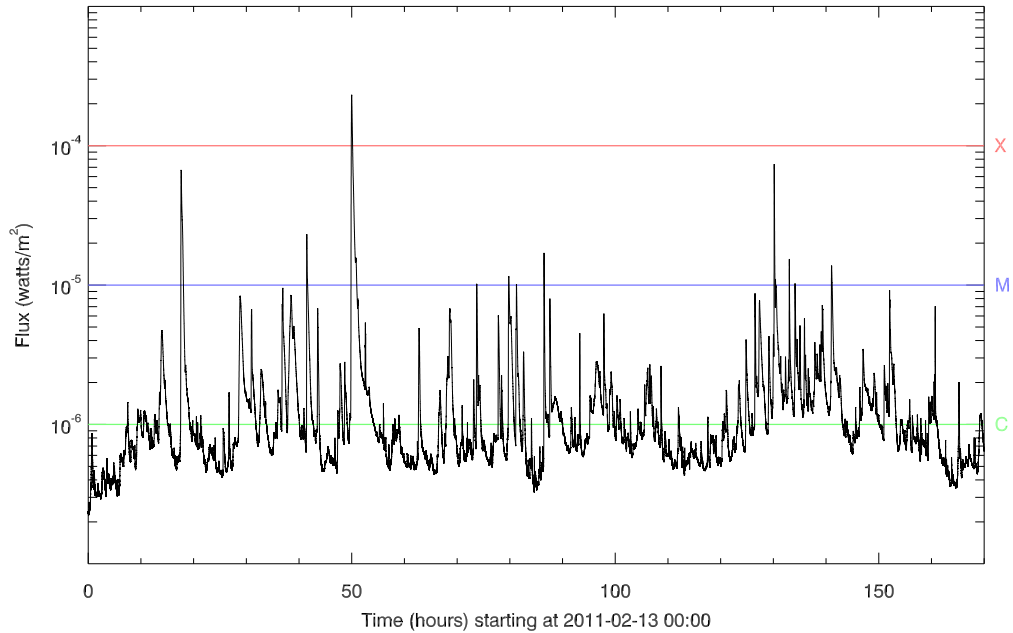
**Figure 3.4:** *GOES 1-8 Å full-disc X-ray flux over a 7-day period. The red horizontal line indicates the X-class flare classification, the blue horizontal line indicates the M-class flare classification, and the green horizontal line indicates the C-class flare classification. Over this period, there are five M-class flares and one X-class flare originating from AR11158.*

selection criteria). Regardless, five clear sunspots are identified for analysis, each with a duration longer than 24 hours.

### 3.3.3 Flare Integration

Figure 3.4 shows the GOES 1-8 Å full-disc X-ray flux over the analysis period. The HEK data indicates that the X-class flare, five of the seven M-class flares and 48 C-class flares are associated with AR11158 during its transit across the solar disc. The flare energy is calculated using the methods described in chapter 2, using GOES routines built into `SSWIDL`.

# 3.4   Results

Presented in this section are the sunspot rotation and flaring properties of AR11158.

## 3.4.1   Sunspot Rotation Properties

**Rotations**

Figure 3.5 shows the cumulative rotation of each of the five sunspots labelled in figure 3.2. Each line shows the cumulative rotation of the corresponding sunspot, with the shaded regions indicating the associated uncertainties. The vertical lines represent solar flares, limited to flares associated with AR11158 only, with red indicating X-class, blue indicating M-class and green indicating C-class flares. For clarity, the M- and C-class flare lines are confined to the box above the graph.

Two sunspots rotate in the positive (anti-clockwise) direction, and three rotate in the negative (clockwise) direction. The sunspot with the largest positive cumulative rotation is sunspot E, which rotates by $124° \pm 11°$, and the sunspot with the largest negative cumulative rotation is sunspot B, which rotates by $-146° \pm 12°$. Sunspot rotation and flaring occur throughout the analysis period, with the peak in flare power – which in this case is the X2.2 flare – occurring at 01:44 on 15th February 2011, following a significant amount of anti-clockwise rotation from sunspots C and E.

The first M-class flare (M6.6) and several C-class flares occur following the emergence of spots B, C and D. The M2.2 and X2.2 solar flares occur following a period of large positive (anti-clockwise) sunspot rotation, with spots C and E being the main contributors. Following the X2.2 flare, the rotation of spots C and E slow, with C slowing more significantly. Eventually anti-clockwise rotation ceases and E disperses. Negative (clockwise) rotation from spots A, B and D dominates from around 75 hours into the analysis. Shortly after, at around 86 hours, a M1.6 flare
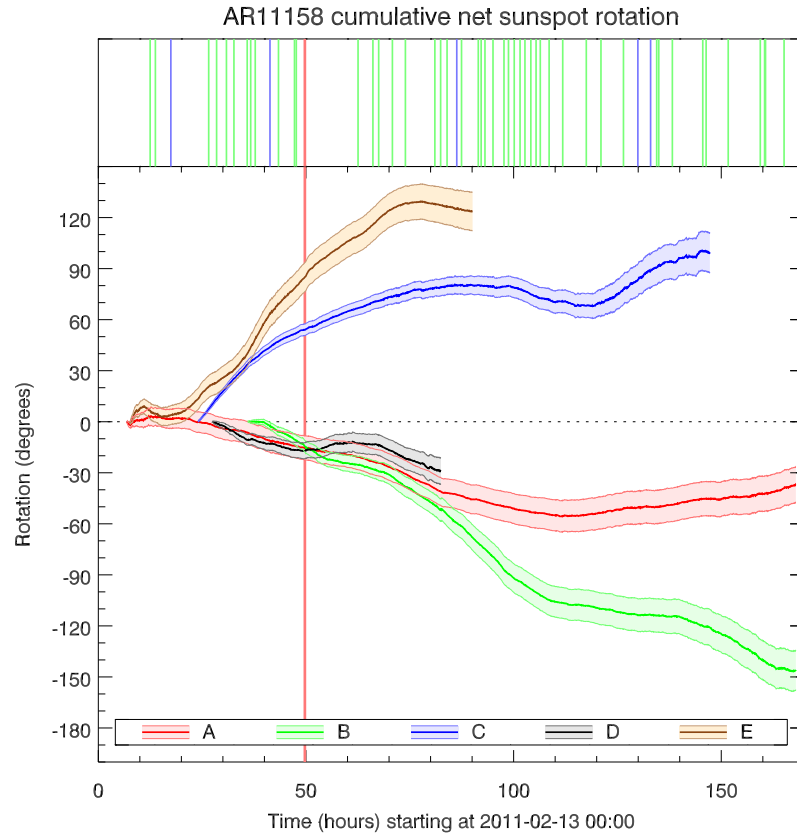
**Figure 3.5:** *The rotation profiles for each sunspot in AR11158 as labelled in the legend at the foot of the plot. The shaded regions indicate the uncertainties associated with each profile, and the zero rotation line is shown by the horizontal dashed line. The vertical lines in the box at the top of the graph represent the start times of solar flares during the analysis period. The red line, which extends down into the graph, indicates the X-class flare. The blue and green lines confined to the upper box indicate M- and C-class flares respectively.*

occurs, followed by a series of 14 C-class flares over the next day. During this flaring, sunspot B's rate of clockwise rotation is increased, levelling out as flaring activity decreases. Sunspot C rotates anti-clockwise following this, and two M-class (M6.6 and M1.4) flares occur in quick succession. Sunspot C then dissipates, and sunspot B increases in rotation velocity once again until the active region traverses the western limb.

It is clear from this plot that the behaviour of sunspot rotations and the link to flaring activity is not simple, especially in a region such as AR11158 where there are several sunspots. High power flares and bursts of flaring activity (such as between 90 and 110 hours into the analysis) appear to occur during or shortly after episodes of high sunspot rotation. This is discussed further in the following section.

**Velocities**

Figure 3.6 shows the rotation of each sunspot defined within AR11158 over time, with the start time of each flare event associated with AR11158 represented by the vertical lines.

The first M(6.6)-class flare occurs prior to any significant rotation, however, the second M(2.2)-class flare occurs following a spike in rotation of sunspot E (which peaks at 5° per hour) and following significant rotation of sunspot C. The X2.2 flare occurs following significant rotation of sunspots B, C and E, and shortly after this flare, there is a quick spike in the rotation velocity of sunspot E (perhaps signifying a sudden un-twisting of the magnetic field following a rapid release of energy). The third M(1.6)-class flare occurs following the decay of sunspot D, and in the decay phase of sunspot E. However, sunspot B is rotating at 5° per hour when the flare occurs, and another 12 C-class flares occur in quick succession during an increased rotation rate of this sunspot. The final two M(6.6 and 1.4)-class flares occur within four hours of one another, during an increase in rotation of sunspot C.
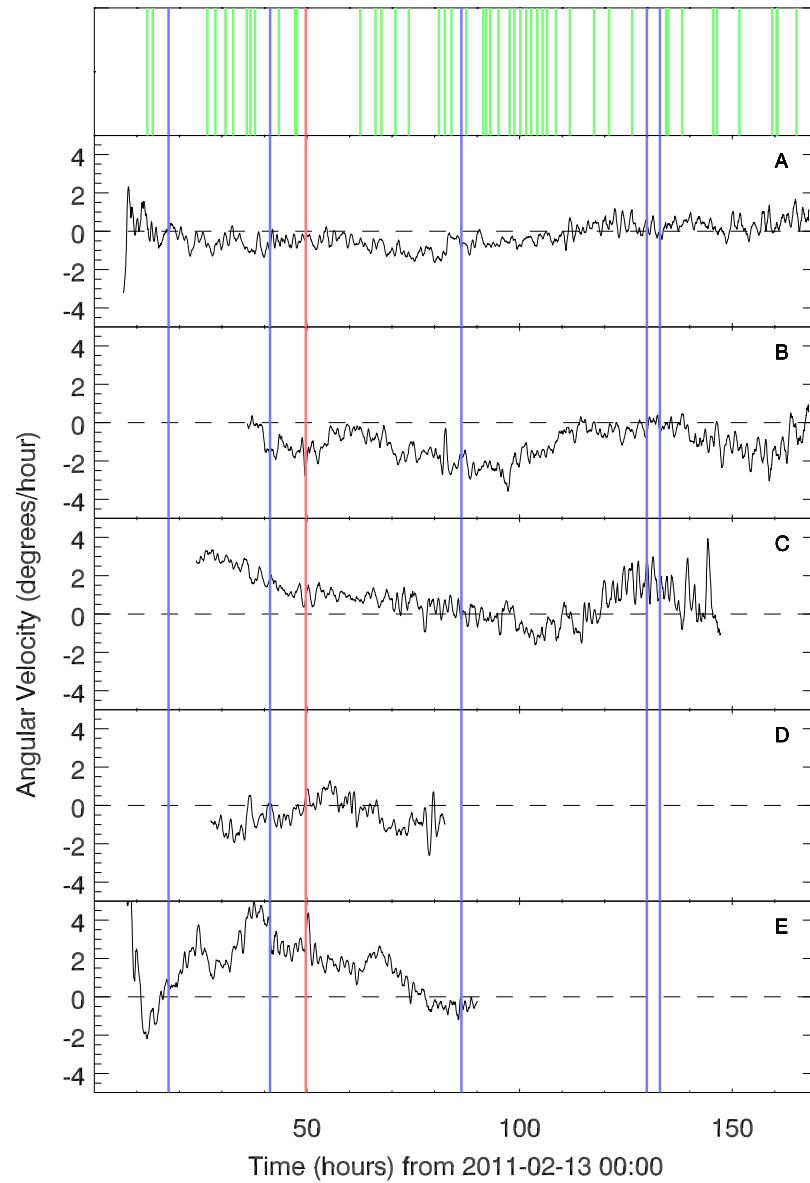
***Figure 3.6:*** *Velocity profiles for each sunspot - labelled A to E from top to bottom - defined within AR11158. The green vertical lines represent C-class flares, blue vertical lines represent M-class flares and the red vertical line represents the X-class flare. The dashed horizontal line on each plot signifies zero rotation.*

CHAPTER 3

**Spatial Flare Association**

Sunspot velocities seem to be linked with larger flares and bursts of flaring activity. However, it is also important to examine the position of the flares relative to the rotating sunspots, to determine whether there is a clear relationship between the quickly rotating sunspots and the location of the flare.
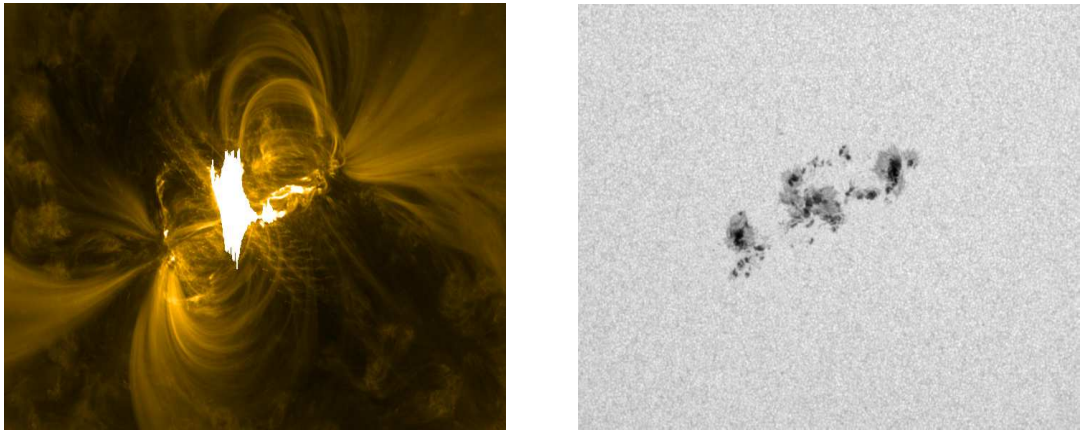


**(a)** *AIA171 Å, 2011-02-13 17:38.*      **(b)** *HMI continuum, 2011-02-13 17:38.*

***Figure 3.7:*** *AIA 171 Å (left) and HMI continuum (right) images of the M6.6 flare at the flare peak time, 2011-02-13 17:38.*

Figure 3.7 shows the peak of the M6.6 flare that occurred at 17:28 (peaked at 17:38) on 2011-02-13, which corresponds to the first blue vertical line in figure 3.6. Spots A and E are well-formed at this point, and are both connected to the emerging flux that will eventually form spots B, C and D. The flare occurs in the region of emerging flux, and spot A has not exhibited any significant rotation prior, whereas spot E exhibits a peak clockwise rotation of 2° per hour approximately 10 hours prior to the flare. The flare occurs in a region of emerging and shearing flux, so the majority of the energy for this particular flare is likely to have been injected via these processes, rather than rotation.
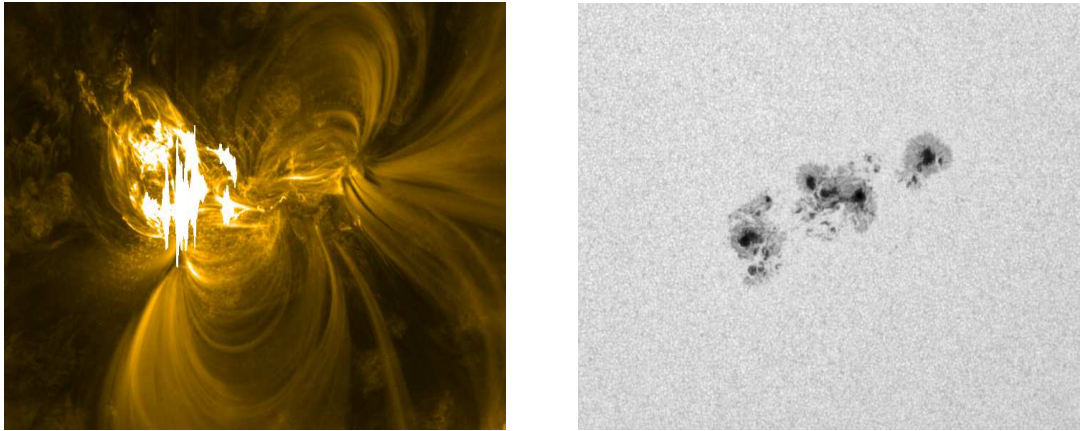
(a) AIA171 Å, 2011-02-14 17:26.　　　　(b) HMI continuum, 2011-02-14 17:26.

**Figure 3.8:** *AIA 171 Å (left) and HMI continuum (right) images of the M2.2 flare at the flare peak time, 2011-02-14 17:26.*

Figure 3.8 shows the peak of the M2.2 flare that occurred at 17:20 (peaked at 17:26) on 2011-02-14, and corresponds to the second blue vertical line in figure 3.6. This flare occurs much closer to sunspot E, following a period of fast rotation (peaking at 5° per hour). Following the flare, there is a significant decrease in the rotation speed of sunspot E, as it drops from around 4° per hour to 2° per hour. In this case, it would be reasonable to assume that this flare is the result of (or at least partially) sunspot rotation.

Figure 3.9 shows the peak of the X2.2 flare that occurred at 01:44 (peaked at 01:56) on 2011-02-15, and corresponds to the red vertical line in figure 3.6. The brightening occurs primarily in the vicinity of spots B, C and D, but secondary, dimmer brightening occurs at spots A and E. The flare occurs during 2° per hour clockwise rotation of sunspot B, which continues rotating at this velocity for 5 hours after the flare. Sunspot E is rotating at 2-3° per hour when the flare occurs. The velocities of sunspots C, D and E spike shortly after the onset of the flare, all in the anti-clockwise direction, whereas spots A and B do not exhibit clear velocity
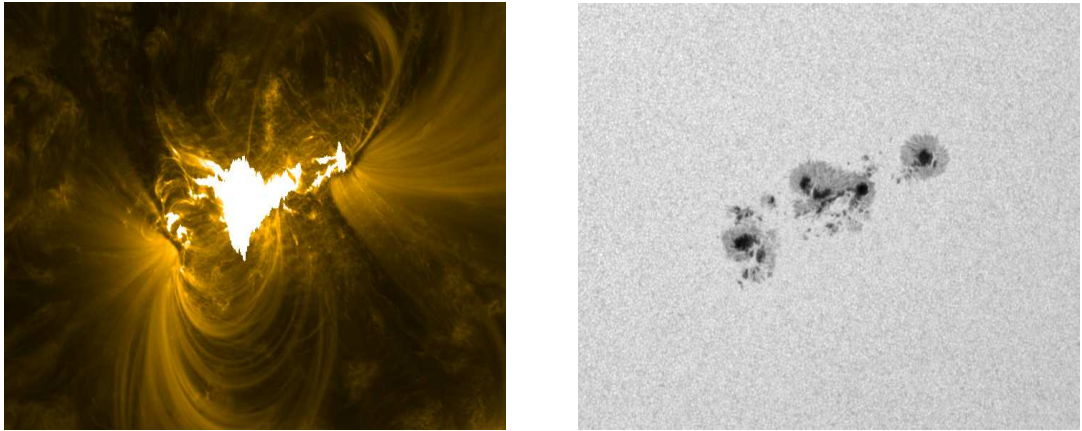
*(a)* *AIA171 Å, 2011-02-15 01:56.*   *(b)* *HMI continuum, 2011-02-15 01:56.*

***Figure 3.9:*** *AIA 171 Å (left) and HMI continuum (right) images of the X2.2 flare at the flare peak time, 2011-02-15 01:56.*

spikes (arguably the velocity of spot B spikes just prior and during the flare, in the clockwise direction). Shearing is also occurring between sunspots B and C during the flare, so it is difficult to pin down the exact energy injection process in this case, although it is most likely a combination of sunspot rotation and shearing.

Figure 3.10 shows the peak of the M1.6 flare that occurred at 14:19 (peaked at 14:25) on 2011-02-16, and corresponds to the third blue vertical line in figure 3.10. The flare appears to occur along the loops joining spots D and E. This is interesting, as spot D is too small to analyse at this point in time, and spot E is decaying, no longer exhibiting more than 1° per hour rotation. Sunspot B is rotating by 2-3° per hour during the flare, but does not appear to be closely linked to the flaring region itself (it does however appear to be linked to sunspot E). The cause of this flare is difficult to pin down.

Although a further two M-class flares occurred in this region (an M6.6 and M1.4), these are not included in the spatial analysis, as the region is close enough to the solar limb that projection effects would significantly affect the analysis.
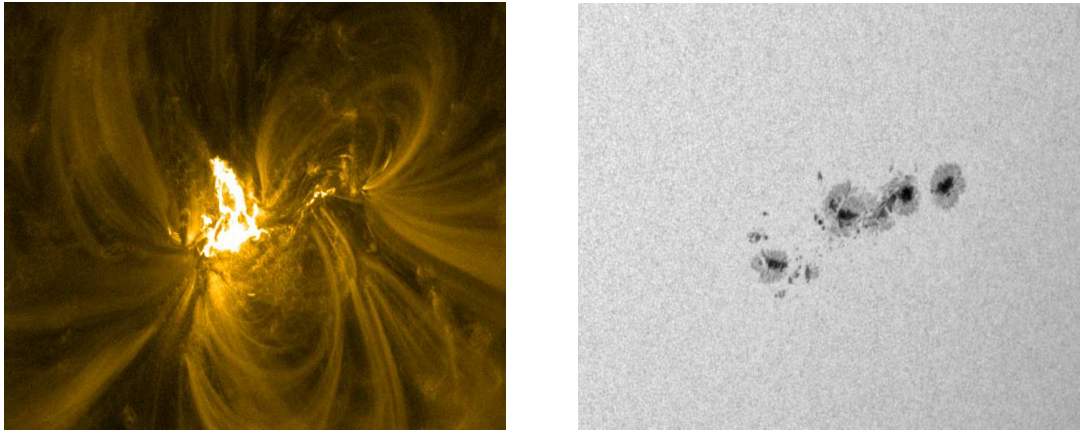
(a) AIA171 Å, 2011-02-16 14:25.        (b) HMI continuum, 2011-02-16 14:25.

**Figure 3.10:** *AIA 171 Å (left) and HMI continuum (right) images of the M1.6 flare at the flare peak time, 2011-02-16 14:25.*

### 3.4.2 Definitions of Rotation

**Sunspots**

The effect of sunspot rotation can be interpreted in different ways, with a key issue being the direction in which the sunspot rotates and whether energy is being injected into or removed from the system. Consider a sunspot, analysed for 100 hours that rotates by 50° in the first 50 hours of analysis, and rotates by -50° in the final 50 hours of analysis. In this case, the net rotation of the sunspot would be 0°, and the absolute rotation would be 100°. If the sunspot rotates by the initial 50°, causing a reconnection event which dissipates all injected energy, and then rotates by -50°, then the effective injection is from the summed absolute rotation value of 100°, as, in this case, the energy from the initial rotation is assumed to be used in a reconnection event, and not removed by the negative rotation. This is an approximation of the maximum possible energy injected by rotation, as it assumes none is removed by un-twisting. If there is no reconnection event during the analysis, the twist is

summed regularly, such that negative rotation cancels out positive rotation (giving the sunspot a net rotation of 0°), as there is no observable means by which the energy from the initial twist can be dissipated. Realistically, the actual amount of energy released depends on when flares occur and how large they are, and lies between these two extremes. Section 1.7.2 discusses cases where sunspot rotation is observed both before and after flares. This implies that scenarios where the rotation is adding energy to the system, and scenarios where the sunspot rotation is removing energy from the system, are both possible.

The net rotation of the sunspot can be considered a minimum amount of rotation, whereas the absolute rotation can be considered a maximum, at least in terms of the sunspot's contribution to the amount of magnetic free energy stored in the corona. So, for each sunspot two types of rotation are defined:

- Cumulative absolute sunspot rotation: the cumulative rotation of a single sunspot, summing the absolute values of rotation.

- Cumulative net sunspot rotation: the cumulative rotation of a single sunspot, taking into account both positive and negative rotation directions. Negative rotation cancels out any positive rotation.

Both of these profiles are presented in Figure 3.11 for sunspot C, as this spot exhibits rotation in both directions. The cumulative net sunspot rotation profile is displayed in the upper panel, and the cumulative absolute sunspot rotation of the same sunspot in the lower panel. The direction of rotation is determined by the bulk direction over 1 hour periods to ensure that small scale noise does not artificially inflate the rotation.

Table 3.2 shows the final rotation total, using the above definitions, as well as the analysis times of the five sunspots in AR11158. Of particular note is sunspot A, which has a cumulative net rotation of -37° ± 10°, but has a cumulative absolute rotation of 88° ± 10°.
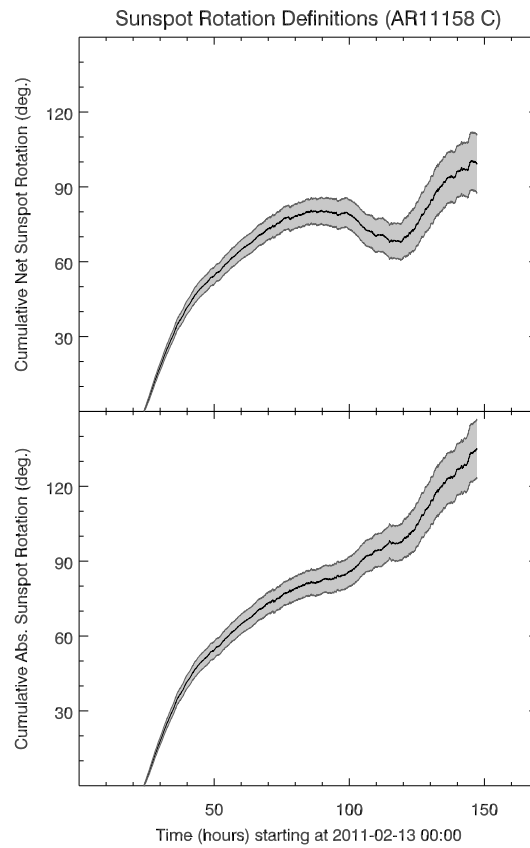
**Figure 3.11:** *AR11158 C rotation profiles. Top panel: The cumulative net rotation. This profile takes into account the direction of rotation and indicates the minimum possible rotation exhibited by the sunspot. Lower panel: The cumulative absolute rotation - the rotation of the sunspot calculated neglecting the direction of rotation. This defines the maximum possible amount of twist injected by the sunspot.*

**Table 3.2:** *Sunspot analysis times and rotation properties. The Sunspot column contains the name of the sunspot as defined in figure 3.2. the Start and End columns contain start and end analysis dates/times respectively, and the Cumulative Rotation columns contain the Absolute and Net rotation values of each sunspot over the analysis period.*

| Sunspot | Start | End | Cumulative Rotation (°) | |
|---|---|---|---|---|
| | | | Absolute | Net |
| A | 2011-02-13 06:51 | 2011-02-19 23:59 | 88 ± 10 | −37 ± 10 |
| B | 2011-02-14 11:57 | 2011-02-19 23:59 | 152 ± 12 | −146 ± 12 |
| C | 2011-02-14 00:00 | 2011-02-19 03:15 | 135 ± 12 | 100 ± 12 |
| D | 2011-02-14 03:24 | 2011-02-16 10:30 | 41 ± 8 | −29 ± 8 |
| E | 2011-02-13 07:36 | 2011-02-16 18:06 | 147 ± 11 | 124 ± 11 |
| **Cumulative active region spot rotation:** | | | 563 ± 24 | 12 ± 24 |

**Active Regions**

It is important to understand how sunspots interact with one another in the context of multi-sunspot active regions. In some cases the rotation of sunspots may combine or counteract each other, depending on how well they are connected and in what directions they rotate. These interactions determine the overall energy contribution from sunspot rotation into the active region. Consider two sunspots that are perfectly connected to each other, and both rotate in the opposite direction by the same magnitude, then the net change in twist of the flux tube is zero as the rotation of one removes the helicity/energy injected by the other. However, if both sunspots rotate in the same direction by the same magnitude, the total twist of the flux tube is essentially doubled. To take into account these sunspot-sunspot interactions, definitions of the rotation of all spots within each active region are defined:

CHAPTER 3

- Absolute cumulative spot rotation: the cumulative absolute rotation of each sunspot within the active region is summed. This represents a maximum possible injection of twist from rotation.

- Net cumulative spot rotation: the cumulative net rotation of each sunspot within the active region is summed taking the direction of rotation into account. This represents a minimum possible injection of twist from rotation.

The net cumulative spot rotation for AR11158 is $12° \pm 24°$ and the absolute cumulative spot rotation is $563° \pm 24°$ (table 3.2).

The net cumulative rotation and absolute cumulative rotation profiles of AR11158 over time are shown in the bottom and middle panels of figure 3.12, respectively. The top panel of the figure shows the radiative energy loss from flaring over time, obtained by integrating the flares associated with AR11158 within figure 3.4 using the method described in section 2.4. The vertical lines represent solar flares, with the red line indicating the X-class flare and the blue lines indicating M-class flares. The corresponding flare classification is given above the plot. The period of high positive spot rotation prior to the X-class flare is apparent in both plots.

The absolute cumulative spot rotation shows that rotation is present at nearly all times throughout the analysis, and the total rotation increases steadily after the large amount of rotation prior to the X2.2 flare. As the total rotation of the active region increases, so too does the total radiated bolometric flare energy. The large jump in flare energy at 50 hours into the analysis is due to the X-class flare, and smaller jumps can be seen from M-class and high-energy C-class flares.

Studying the net cumulative spot rotation plot, it is apparent that after the X2.2 flare there is a change of direction of rotation of the active region as a whole following the peak of just over $120°$ at about 70 hours into the analysis. This is down to the dissipation of sunspot E, and the slowing of positive rotation of C, meaning that the negative rotation of sunspots A, B and D dominates. The net rotation steadily
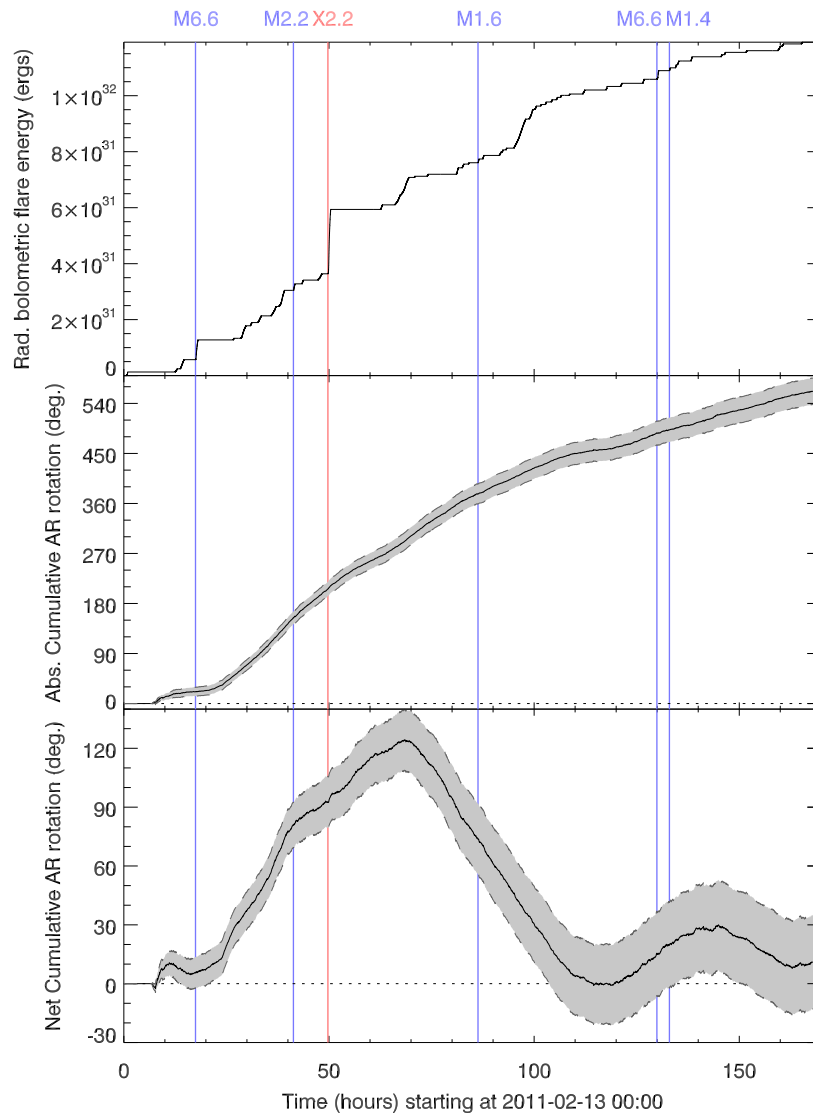
**Figure 3.12:** *Total spot rotations in comparison to radiative bolometric flare energy. The rotation profiles in this figure are the summed values of absolute cumulative and net cumulative sunspot rotations in the active region (see Table 1). The top plot shows the total bolometric flare energy radiated by AR11158, extrapolated from the X-ray flux, with baseline X-rays assumed from the non-flaring Sun. The middle plot shows the absolute cumulative spot rotation, and the bottom plot shows the net cumulative spot rotation over time. The red vertical line represents the start time of the X-class flare and the blue vertical lines represent the start times of the M-class flares.*

approaches zero, before reversing direction again at approximately 120 hours into the analysis. Two more M-class (M6.6 and M1.4) flares occur during this period of positive rotation, which peaks at 28°, before reversing direction one last time. By the end of the analysis, the final net cumulative spot rotation is 12° ± 24°.

Inspection of the absolute cumulative spot rotation shows that the active region is constantly dynamically active, which may be continuously driving the flaring activity observed throughout the analysis period.

Ultimately the question comes down to whether opposite rotations are cancelling each other out and removing helicity (and hence magnetic free energy), or are summed together and injecting helicity into the system. The absolute cumulative and net cumulative spot rotations can be interpreted as a minimum and maximum possible amount of rotation that provides the helicity required for flares to draw energy from. Realistically, the actual amount of rotation that contributes flare energy to draw from is most likely somewhere in between these two values, as spots are not likely to be perfectly interconnected.

To calculate the energy contribution from sunspot rotation, one must consider the amount of helicity injected into the corona, and convert this into a magnetic free energy value. To do this in a convincing manner, the best approach would be from the modelling side (such as nonlinear force-free coronal field extrapolations). However, there is literature on the subject in the context of this active region, in which Vemareddy et al. (2012) calculate sunspot rotation and the available energy as a result of this rotation over time. From AR11158, sunspot E has a flux of $3.16 \times 10^{21}$ Mx and an absolute rotation of 147° ± 11°. Using equation 2.9, this is converted into a helicity of $\Delta H = (4.08 \pm 0.31) \times 10^{42}$ Mx$^2$, and, using equation 2.10, is converted into an energy of $E_E = (5.54 \pm 0.41) \times 10^{31}$ erg. The helicity value calculated using this method agrees well with the value of $4.35 \times 10^{42}$ Mx$^2$ calculated by Vemareddy et al. (2012), for the same sunspot. This is
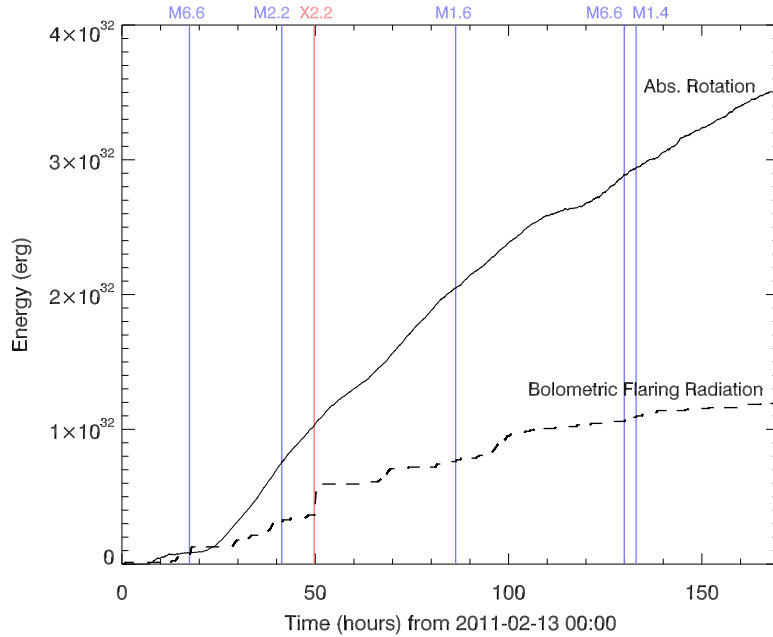
**Figure 3.13:** *The energy contribution from absolute rotation (solid line) and bolometric flare radiation (dashed line) over the analysis period. The vertical lines represent solar flares, with the corresponding flare classification stated above the plot.*

repeated for each sunspot in the region, and the sum of the energy contributions from each spot represents the total active region energy contribution from sunspot rotation. The energy contribution from the net rotation is $(-0.14 \pm 0.17) \times 10^{32}$ erg and the contribution from the absolute rotation is $(3.53 \pm 0.18) \times 10^{32}$ erg for AR11158. The negative sign on the net energy contribution indicates the net helicity direction of the region (with negative being clockwise and positive being anti-clockwise).

Figure 3.13 shows the energy contribution from absolute rotation (solid line) and bolometric flare radiation (dashed line) over the analysis period. The energy from absolute rotation represents a maximum possible energy contribution from rotation, and is just under triple the radiated bolometric flare energy. The energy gap between

**Table 3.3:** *Literature values and analysis periods of the rotation of sunspots within AR11158 compared with values obtained and analysis periods covered using the method described in this thesis. The Method column lists the authors of the papers used as a comparison, the Spot(s) column lists the spots analysed (defined in this work), the T. Anlys column lists the duration of analysis, and the Literature and Thesis Rots. columns list the rotation values obtained from the method used in the corresponding paper and the method used in this work over the same (or as close to as possible) time period.*

| Method | Spot(s) | T. Anlys. | Literature Rots. | Thesis Rots. |
|--------|---------|-----------|------------------|--------------|
| Jiang | B | 2d | $38 - 107°$ | $35°$ |
| Vemareddy | B, E | 3d | $110°, 170°$ | $35°, 138°$ |
| Wang | B, D | 1h 40m | $3\text{-}37°$ $\text{hr}^{-1}$ | $1.9°$ $\text{hr}^{-1}$, $0.7°$ $\text{hr}^{-1}$ |
| Li | E | 5d | $200°$ | $138°$ |

these two values represents the amount of energy from rotation available for other solar activity such as coronal mass ejections and particle acceleration. The energy contribution from rotation remains above the radiated bolometric flare energy for the majority of the analysis period.

## 3.5   Conclusions

Table 3.3 compares the total rotation values and rotation rates of the literature with the values obtained by the method used in this thesis.

In general, the method used in this work appears to produce lower values of rotation than those listed in the literature, most likely because the method employed in this work calculates an average velocity across the whole sunspot.

This study shows that the rotational motions of sunspots within AR11158 appear

to follow a similar upwards trend over time as the bolometric flaring energy. The absolute cumulative spot rotation is $563° \pm 24°$, vastly more than enough to trigger an M8.0 flare as modelled by Kazachenko et al. (2009), and may account for the continuous flaring activity throughout the analysis. On the other hand, the net cumulative spot rotation at the end of the analysis period is just $12° \pm 24°$, as the initial positive rotation is cancelled out by the negative rotation towards the latter stages of the analysis. The true amount of rotation that contributed towards the energy reservoir from which solar flares draw their power is most likely somewhere in between these two values.

Although in this case, the high amount of flaring activity appears to be coupled to – or potentially caused by – sunspot rotation, to further our understanding of how energy is transferred into the corona, particularly via sunspot rotation, a statistical study is required.

A thorough and robust analysis tool, documented in chapter 2 has been developed, which is employed here to calculate the sunspot rotations. This study has built on this tool by defining more objective sunspot selection criteria, defining sunspot rotation properties, and developing a method with which to calculate the magnetic flux based on sunspot area, and magnetic energy due to rotation. The next chapters will focus on statistical studies of sunspots in two discrete samples, X-class flare producing regions (chapter 4) and an unbiased sample of all sunspots between 1 May 2013 and 31 August 2013 (chapter 5) using the definitions and work carried out in this chapter. These statistical studies will give an insight into the relationship between sunspot rotation and solar flares.

As the sunspot rotation calculation only determines rotation values for sunspot penumbrae, a substantial amount of active region flux is being neglected. This flux is neglected as the rotation of the missing flux (which mostly includes sunspot umbrae and pores) cannot be determined with any degree of confidence. The total

amount of flux being captured by analysing the penumbra is less than 46% of the total amount of flux in the active region. This indicates that following calculations of helicity and the magnetic energy contributed from sunspot rotation are likely to be under-estimates, as the magnetic helicity is proportional to the flux squared.

# Chapter 4

# X-Class Flare Sample

## 4.1   Introduction

Chapter 3 focused on a case study of AR11158, which developed the analysis tools required to understand the effect of sunspot rotation on flaring activity. This chapter builds on this by compiling a statistical sample of high flare-energy active regions, defined here as all regions that have given rise to an X-class solar flare since the launch of SDO. The purpose of this study is to determine to what extent sunspot rotation is present in these high flare-energy regions.

## 4.2   The Sample

Forty-two X-class solar flares have occurred since the launch of SDO, taking place between 15th Feb 2011 and 30th May 2015. This sample is restricted to the 26 active regions (containing a total of 76 sunspots) with which these X-class flares are associated.

Additionally, four X-class flare regions are presented in more detail in this chapter, along with two low flare-energy regions not from the sample. These regions were picked specifically because they all exhibit different rotation and flaring properties

***Table 4.1:*** *Properties of the six active regions analysed in detail. The four top regions are X-class flare producing regions and the lower two, separated by the horizontal line, are non-X-class flare regions. Columns: AR is the active region number; Start is the analysis start time; End is the analysis end time; The Hale class column shows the most complex Hale class assigned to the region over the analysis period; AR Rot Net is the net spot rotation; AR Rot Abs. is the absolute spot rotation; Flares, C M and X are the numbers of the corresponding class of flare associated with the active region.*

| AR | Start | End | Hale | Spot Rot (°) | | Flares | | |
|----|-------|-----|------|-----|------|---|---|---|
| | | | Class | Net | Abs. | C | M | X |
| 11166 | 2011-03-05 00:00 | 2011-03-13 23:59 | $\beta\gamma\delta$ | -81 | 212 | 25 | 4 | 1 |
| 11515 | 2012-06-29 00:00 | 2012-07-07 23:59 | $\beta\gamma\delta$ | 385 | 434 | 62 | 26 | 1 |
| 11944 | 2014-01-03 11:57 | 2014-01-11 23:59 | $\beta\gamma\delta$ | -96 | 204 | 28 | 5 | 1 |
| 12158 | 2014-09-06 11:57 | 2014-09-15 19:18 | $\beta\gamma$ | 207 | 207 | 6 | 1 | 1 |
| 11770 | 2013-06-15 00:00 | 2013-06-22 23:59 | $\alpha\delta$ | 16 | 35 | 0 | 0 | 0 |
| 11772 | 2013-06-18 00:00 | 2013-06-23 23:59 | $\beta\gamma$ | -29 | 118 | 6 | 0 | 0 |

and allow a comparison between high and low flare-energy regions to be drawn. These regions and their rotation and flaring properties are listed in table 4.1.

More specifically, the four X-class sample regions display the following differing properties. AR11166 contains four sunspots, all of which rotate and exhibit a reasonably large amount of rotation, with the only positive (anti-clockwise) rotator, B, emerging over five days after the first sunspot, A, traverses the eastern limb. AR11515 begins as a single sunspot, A, which splits after approximately 70 hours into sunspots AA and AB. Sunspots A and AA combined exhibit an extremely large amount of rotation. AR11944 contains three sunspots which all emerge at approximately the same time, with sunspots A and B rotating by comparable amounts in

opposite directions (potentially cancelling each other out), such that the majority of the net rotation of the active region as a whole, comes from sunspot C. Finally, AR12158 consists of a single sunspot, which exhibits 207° rotation over approximately 9 days.

The two active regions from outside the X-class sample were chosen because of their different properties. AR11770 is a simple single sunspot region which exhibits almost no rotation, and gives rise to no solar flares, and AR11772 is a bipolar sunspot region which exhibits a small amount of rotation and six C-class solar flares.

## 4.3    Analysis

The methods employed in this chapter are described in chapers 2 and 3. Briefly, the sunspot rotation is calculated using SDO/HMI continuum data and flare data is extracted from the HEK. The sunspot rotation is converted into magnetic energy by calculating the helicity contribution, and the GOES flare curve is integrated to obtain the radiated optically thin flare energy. This is converted into a bolometric flare energy using the conversion factor defined in chapter 2, derived from Emslie et al. (2012). These two quantities are compared to determine whether sunspot rotation provides enough energy to account for the flaring observed in each region.

The sunspot selection criteria are the same as stated in section 3.3.2, which aims to remove subjective bias for determining which sunspots within a region are analysed. The only addition to the criteria in this chapter is that each sunspot must be contained within an active region that gives rise to an X-class solar flare. All sunspots meeting this criteria are included in the sample.

This chapter approaches the problem from a statistical standpoint, rather than an in-depth analysis of each individual region. However, rotation profiles of each region (such as the profiles contained in figure 4.1) are included in the appendix.

### 4.3.1   Definitions of Rotation

The net and absolute spot rotations are defined in chapter 3, and are henceforth referred to as $R_{net}$ and $R_{abs}$ respectively. In addition to this, a third active region rotation quantity is defined in this chapter, the mid spot rotation, $R_{mid}$, and is defined as

$$R_{mid} = \frac{|R_{net}| + R_{abs}}{2}. \tag{4.1}$$

The mid rotation is introduced to take into account for the fact that no two sunspots within an active region are likely to be perfectly connected or disconnected from one another, and as such the real value of rotation is likely to be somewhere between $R_{net}$ and $R_{abs}$. The uncertainty on $R_{mid}$ is scaled by the difference $R_{net}$ and $R_{abs}$ for each region, and is given by

$$\delta R_{mid}^2 = \frac{1}{4}\left[\delta R_{net}^2 + \delta R_{abs}^2\right] + \frac{(R_{abs} - |R_{net}|)^2}{12}. \tag{4.2}$$

Regions such as AR11158 have large $\delta R_{mid}$ values, as the difference between its absolute spot rotation (563°) and net spot rotation (12°).

## 4.4   Results

Presented in this section are the sunspot rotation profiles for the six selected active regions, four from the X-class flare producing sample and two non-X-class flare producing regions. Statistical results are presented later in this section.

### 4.4.1   X-class Flare Producing Regions

As stated in section 4.2, the six active regions presented in this section were selected for presentation here because of their differences in structural, rotational and flaring properties. For information regarding analysis periods, rotation values and number of flares associated with each region, refer to table 4.1.

**(a)** *AR11166*



**(b)** *AR11515*



**(c)** *AR11944*



**(d)** *AR12158*
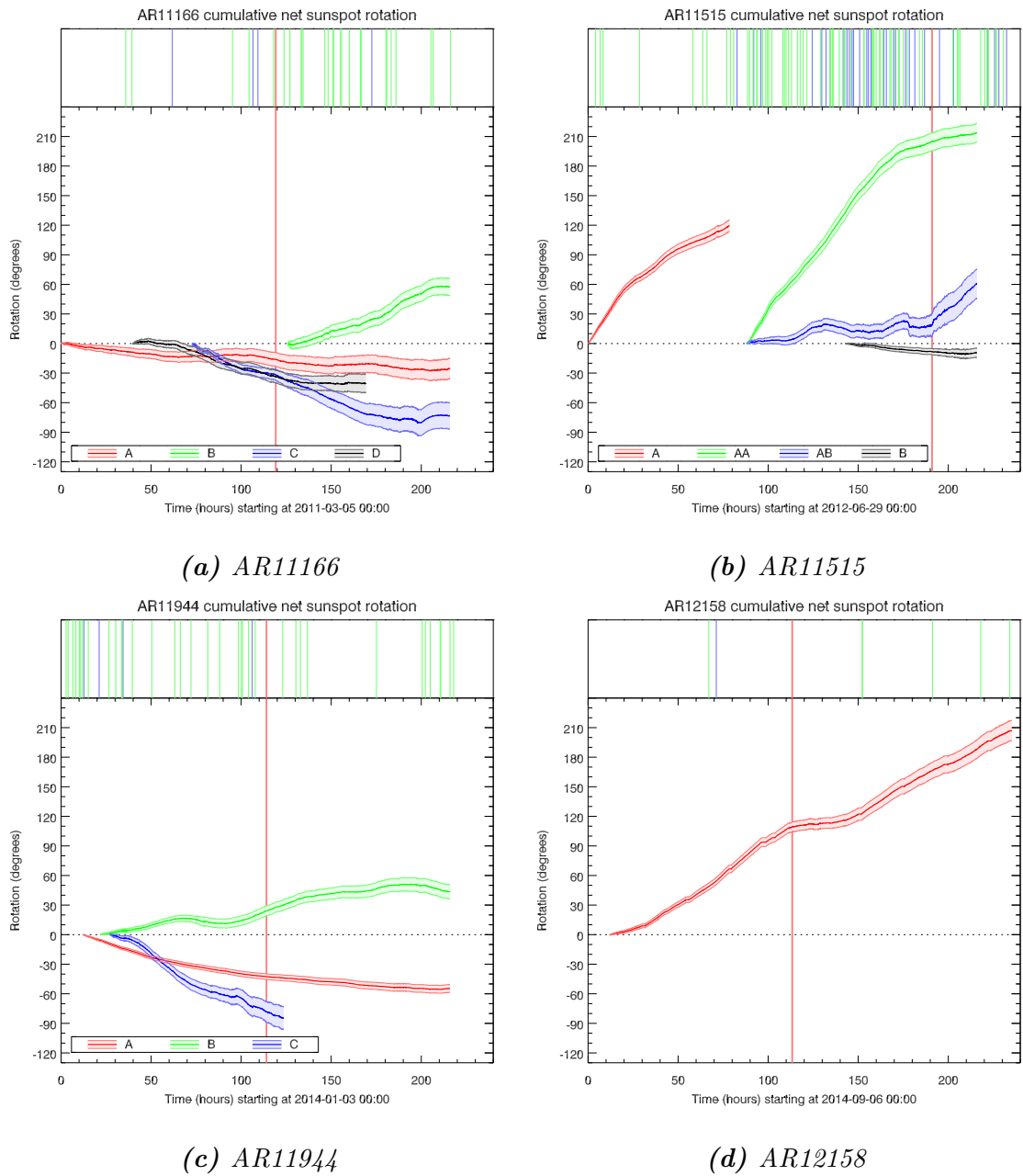
***Figure 4.1:*** *Rotation profiles for the X-class flare producing active regions examined in detail in this work. In each case, the X-class flare associated with these regions occurs during the analysis period. The label at the foot of the plot identifies the sunspot analysed, and the shaded area about the profiles represents the associated uncertainties. The vertical lines in the box above the plot represent solar flares, with green being C-class, blue being M-class and red being X-class. X-class vertical lines extend down into the plot area.*

CHAPTER 4

AR11166, presented in figure 4.1(a), gives rise to an X1.5 solar flare on 9th March 2011, at 23:13, as well as four M-class flares over the period of analysis. This region exhibits rotations of $R_{net} = -81° \pm 21°$, $R_{abs} = 212° \pm 21°$, and $R_{mid} = 147° \pm 48°$. Sunspot B emerges following the X-class flare, and is large enough to begin analysis at 05:45 on 10th March 2011. The X-class flare follows rotation from sunspots A, C and D, but may have been caused by the emerging flux, from which sunspot B is formed.

AR11515, presented in figure 4.1(b), gives rise to an X1.1 solar flare at 23:01 on 6th July 2012, as well as 26 M-class flares over the period of analysis. Exhibiting rotations of $R_{net} = 385° \pm 19°$ and $R_{abs} = 434° \pm 19°$, this region is the third highest rotator in the sample, and the highest rotator selected for in-depth discussion in this work. The mid rotation of this region is $R_{mid} = 409° \pm 30°$, making it the second highest mid rotation in the sample. This region traverses the eastern limb as a single sunspot, which rotates by over 120° in the space of approximately 75 hours, before splitting into sunspots AA and AB. Sunspot AA exhibits a further 210° rotation over approximately 120 hours, before the region traverses the western limb. Sunspot AB rotates by around 60°, but sunspot B, which emerges towards the end of the analysis period, rotates very little in comparison to the others. This region gives rise to 62 C-class and 26 M-class flares, many of which occur during the fast rotation of sunspot AA following the splitting. The X-class flare occurs as the rotation of AA slows, and following this X-class flare, the rotation velocity of sunspot AB increases. Whether this burst of flaring activity is caused by the splitting or the rotation is open to interpretation, although the answer is potentially a combination of both.

AR11944, presented in figure 4.1(c), gives rise to an X1.2 solar flare at 18:04 on 7th January 2014, and five M-class flares over the period of analysis. The region rotations are $R_{net} = -96° \pm 14°$, $R_{abs} = 204° \pm 14°$ and $R_{mid} = 150° \pm 37°$. This

region contains three sunspots, two of which (A and B) rotate in opposite directions by comparable amounts, potentially cancelling each other out. This would mean that sunspot C alone potentially provides the energy required for the X-class flare to occur, which occurs after C has rotated by around 80°. Sunspot C dissipates shortly after the X-class flare, and flaring activity reduces significantly.

AR12158, presented in figure 4.1(d), gives rise to an X1.6 solar flare at 17:21 on 10 September 2014, as well an M4.5 solar flare. This region consists of a single sunspot, which rotates by a total of 207° degrees. As the direction of rotation is positive throughout, and as A is the only sunspot in the region, $R_{net}$, $R_{abs}$ and $R_{mid}$ for this region are all 207° ± 10°. The X-class flare occurs after around 110° rotation. It is worth noting that the flat portion of the profile occurs when the sunspot elongates temporarily, calving off two pores, before returning to a circular shape for the rest of its duration on the solar disc. As there is no significant flux emergence in this region, it is reasonable to conclude that the flaring activity results from the sunspot rotation in this case.

## 4.4.2   Low Energy Active Regions

Figure 4.2 shows the two comparison regions, not taken from the X-class flare sample, neither of which give rise to an X-class solar flare. These two regions are included to provide a comparison to the X-class flare producing regions.

AR11770, shown in figure 4.2(a), is a single sunspot active region that exhibits very little rotation, with $R_{net} = 16° ± 14°$ and $R_{abs} = 35° ± 14°$, and the profile presented here is within error of zero for the majority of the analysis period. This region does not produce any solar flares during the analysis period, and is an excellent example of a simple low-energy active region that does not rotate significantly.

AR11772, shown in figure 4.2(b), is a bipolar region that exhibits some rotation. With $R_{net} = -29° ± 33°$ and $R_{abs} = 118° ± 33°$, the rotation is not inconsequential,

*(a) AR11770*　　　　*(b) AR11772*
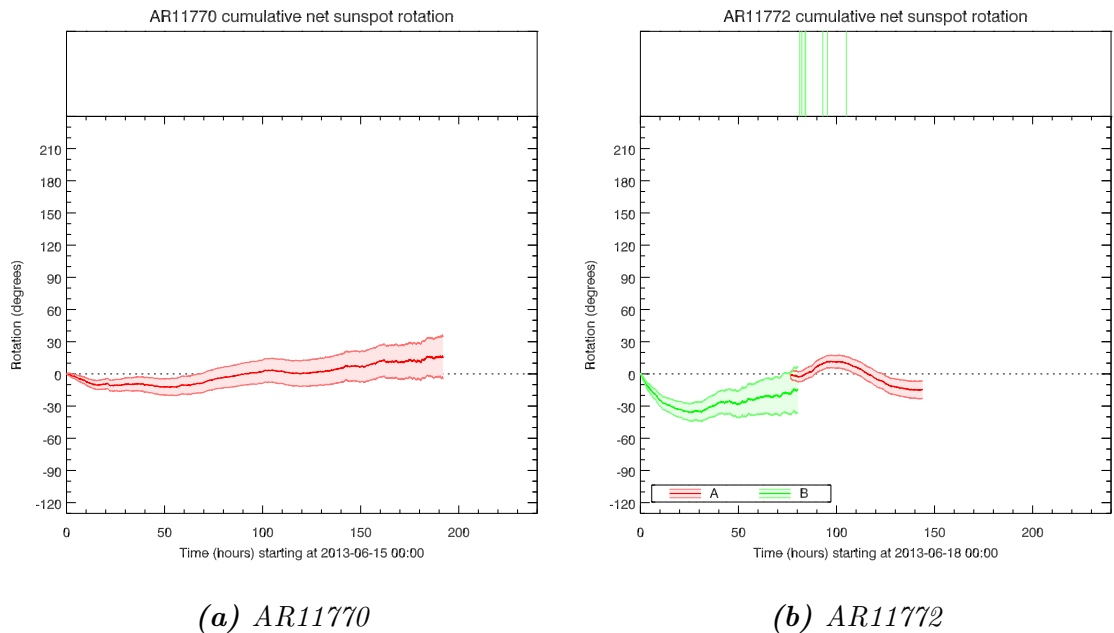
***Figure 4.2:*** *The profiles for two non-X-class flare related active regions. For a description of the features in the plots, see the caption of figure 4.1.*

but is still small compared to the X-class flare regions. This region produces six C-class solar flares over the analysis period; all following the emergence of sunspot A. It is difficult to conclude whether these flares are the result of sunspot rotation, flux emergence, or some other energy input.

There is a sharp contrast between the X-class flare producing regions and the comparison, low flare energy regions presented here. The X-class flare producing regions are generally more magnetically complex (Hale class), more dynamically complex, and produce more flares. The comparison regions both rotate significantly less than the X-class sample regions.

## 4.5   Statistical Results

This section details the statistical results of the study, using data from all 76 sunspots within the 26 active regions associated with X-class solar flares observed
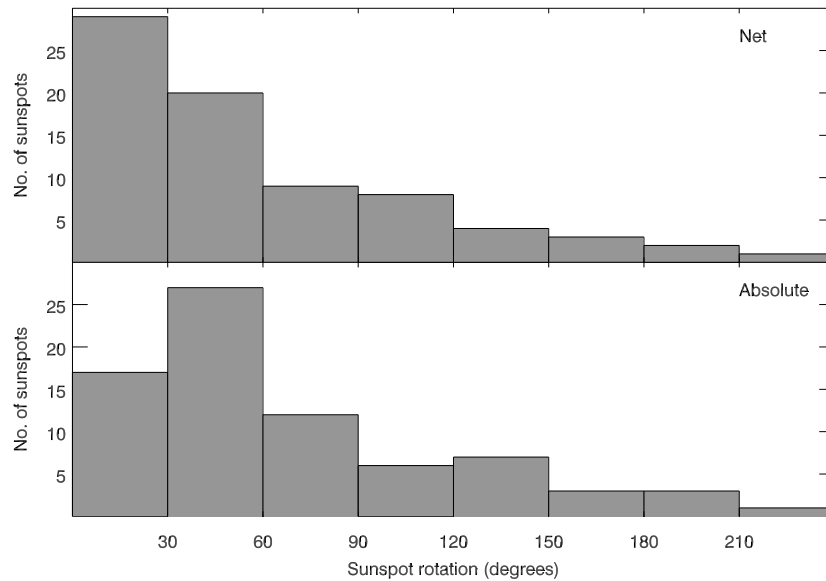
***Figure 4.3:*** *The distribution of sunspot rotations. The top plot shows the net sunspot rotation, and the lower plot shows the absolute sunspot rotation.*

by SDO/HMI.

## 4.5.1   Sunspots

Figure 4.3 shows the distribution of net and absolute sunspot rotations in the X-class flare sample.

Twenty-nine sunspots exhibit a net rotation of less than 30°, and 49 have less than 60° net rotation. On the other hand, only 17 sunspots exhibit less than 30° absolute rotation, and 42 exhibit less than 60° absolute rotation. The net rotation histogram shows a clear downwards trend, in that only a small proportion of sunspots exhibit higher rotation. The absolute sunspot rotation histogram, on the other hand, does show a downwards trend, but the sunspot rotation values are shifted towards the higher end, with a peak in the 30°-60° range.

Although the differences between the net and absolute sunspot histograms are of interest, it is difficult to draw conclusions regarding the magnitude of free magnetic

energy contributed from twist, as most X-class flare producing active regions are multiple sunspot regions, meaning that the sunspots will be magnetically connected and the rotation in the whole active region must be considered.

## 4.5.2 Active Regions

Table 4.2 lists all active regions in the X-class flare sample, along with their analysis periods, number of sunspots, $R_{net}$, $R_{abs}$ and $R_{mid}$ values, as well as number of C-, M- and X-class solar flares. Only five active regions have a $R_{abs}$ of less than $100°$ and the vast majority of regions give rise to over 10 C-class flares and at least 1 M-class flare. Of particular note are AR11515, AR12192 and AR12297. Each of these regions give rise to over 50 C-class flares and over 20 M-class flares (and AR12192 produces 6 X-class flares). AR11515 exhibits $R_{abs} = 434° \pm 19°$ and AR12297 exhibits $R_{abs} = 274° \pm 23°$, but arguably the most active (in terms of flaring) region, AR12192, exhibits only $R_{abs} = 139° \pm 11°$. However, this region is extremely large, containing more flux than any other X-class flare producing region, so the amount of energy generated from the rotation is still larger than any other region at $(6.7 \pm 0.6) \times 10^{33}$ erg (shown in table 4.3).

Uncertainties for $R_{abs}$ and $R_{net}$ values range from $10°$ to $28°$, but are typically around $20°$, whereas the uncertainties for $R_{mid}$ values range from as low as $10°$ up to $163°$ for AR11158 (as this region has a very high $R_{abs}$ and very low $R_{net}$), with typical uncertainties around $30°$.

***Table 4.2:*** *Active regions and their rotation and flare properties. The start and end columns indicate the start and end time of the analysis period for each active region, $N_S$ is the number of sunspots, AR Rot lists the $R_{net}$, $R_{mid}$ and $R_{abs}$ values, and the flare columns indicate number C-, M- and X-class solar flares associated with the active region.*

| AR | Start | End | $N_S$ | AR Rot (°) | | | Flares | | |
|---|---|---|---|---|---|---|---|---|---|
| | | | | $R_{net}$ | $R_{mid}$ | $R_{abs}$ | C | M | X |
| 11158 | 2011-02-13 06:51 | 2011-02-19 23:59 | 5 | 12 | 288 | 563 | 48 | 5 | 1 |
| 11166 | 2011-03-05 00:00 | 2011-03-13 23:59 | 4 | -81 | 147 | 212 | 27 | 4 | 1 |
| 11263 | 2011-07-30 00:00 | 2011-08-08 23:59 | 4 | -56 | 89 | 122 | 35 | 3 | 1 |
| 11283 | 2011-09-01 00:00 | 2011-09-10 23:59 | 2 | -121 | 124 | 127 | 13 | 5 | 2 |
| 11302 | 2011-09-24 00:00 | 2011-10-03 07:06 | 5 | 188 | 211 | 234 | 33 | 15 | 2 |
| 11339 | 2011-11-04 00:00 | 2011-11-13 05:51 | 5 | -32 | 114 | 196 | 38 | 9 | 1 |
| 11402 | 2012-01-17 00:00 | 2012-01-25 18:06 | 4 | 93 | 105 | 117 | 9 | 2 | 1 |
| 11429 | 2012-03-05 00:00 | 2012-03-13 14:27 | 4 | 450 | 460 | 470 | 32 | 14 | 2 |
| 11515 | 2012-06-29 00:00 | 2012-07-07 23:59 | 4 | 385 | 409 | 434 | 73 | 30 | 1 |
| 11520 | 2012-07-08 12:00 | 2012-07-16 23:59 | 4 | -164 | 168 | 172 | 26 | 6 | 1 |
| 11598 | 2012-10-23 00:00 | 2012-10-31 23:59 | 1 | 71 | 73 | 74 | 25 | 3 | 1 |
| 11748 | 2013-05-16 00:00 | 2013-05-21 01:18 | 1 | 107 | 136 | 166 | 19 | 5 | 4 |
| 11875 | 2013-10-19 11:57 | 2013-10-27 18:18 | 5 | 195 | 220 | 245 | 59 | 12 | 2 |
| 11882 | 2013-10-26 12:00 | 2013-11-02 23:59 | 2 | -19 | 59 | 99 | 9 | 11 | 2 |
| 11890 | 2013-11-04 11:57 | 2013-11-11 23:59 | 2 | 5 | 35 | 66 | 46 | 5 | 3 |
| 11893 | 2013-11-10 00:00 | 2013-11-19 10:48 | 1 | -125 | 127 | 128 | 17 | 1 | 1 |
| 11944 | 2014-01-03 11:57 | 2014-01-11 23:59 | 3 | -96 | 150 | 204 | 45 | 8 | 1 |
| 11990 | 2014-02-26 12:00 | 2014-03-07 10:51 | 1 | 92 | 92 | 92 | 6 | 2 | 1 |

**Continued on next page**

| AR | Start | End | $N_S$ | AR Rot (°) | | | Flares | | |
|---|---|---|---|---|---|---|---|---|---|
| | | | | $R_{net}$ | $R_{mid}$ | $R_{abs}$ | C | M | X |
| 12017 | 2014-03-23 12:00 | 2014-03-30 06:51 | 1 | -84 | 87 | 90 | 20 | 3 | 1 |
| 12035 | 2014-04-13 10:00 | 2014-04-22 10:42 | 1 | -174 | 178 | 182 | 47 | 1 | 1 |
| 12087 | 2014-06-12 00:00 | 2014-06-21 05:36 | 3 | -179 | 236 | 293 | 29 | 8 | 3 |
| 12158 | 2014-09-06 11:57 | 2014-09-15 19:18 | 1 | 207 | 207 | 207 | 12 | 1 | 1 |
| 12192 | 2014-10-19 10:00 | 2014-10-27 23:59 | 3 | -9 | 74 | 139 | 74 | 32 | 6 |
| 12242 | 2014-12-14 10:39 | 2014-12-22 19:51 | 3 | -217 | 237 | 257 | 55 | 6 | 1 |
| 12297 | 2015-03-08 12:00 | 2015-03-17 21:15 | 3 | -167 | 221 | 274 | 100 | 23 | 1 |
| 12339 | 2015-05-07 00:00 | 2015-05-15 13:30 | 3 | 74 | 118 | 161 | 56 | 3 | 1 |

*Table 4.2 –continued from previous page*

Figure 4.4 shows the distribution of $R_{net}$, $R_{mid}$ and $R_{abs}$ values of all 26 active regions in the X-class flare sample.

All three histograms show a population of active regions towards the lower end of rotation, although the position of this population varies based on which rotation parameter is observed. As expected, the $R_{net}$ population is shifted most towards the lower end, the $R_{abs}$ the most towards the higher end, and the $R_{mid}$ in between. There are six active regions below the significant spot rotation value of 60° in the $R_{net}$ histogram, zero in the $R_{abs}$ histogram, and two in the $R_{mid}$ histogram.

There are several active regions which deviate from the populated region of the histograms. In the $R_{net}$ histogram, these two regions are AR11515 with $R_{net} = 384° \pm 19°$ and AR11429 with $R_{net} = 450° \pm 24°$. In the $R_{abs}$ histogram, the three high rotation regions are AR11515 with $R_{abs} = 433° \pm 19°$, AR11429 with $R_{abs} = 470° \pm 24°$ and AR11158 with $R_{abs} = 564° \pm 24°$. AR11158 is an interesting case, as it exhibits a very high $R_{abs}$ value, but has a very low net rotation
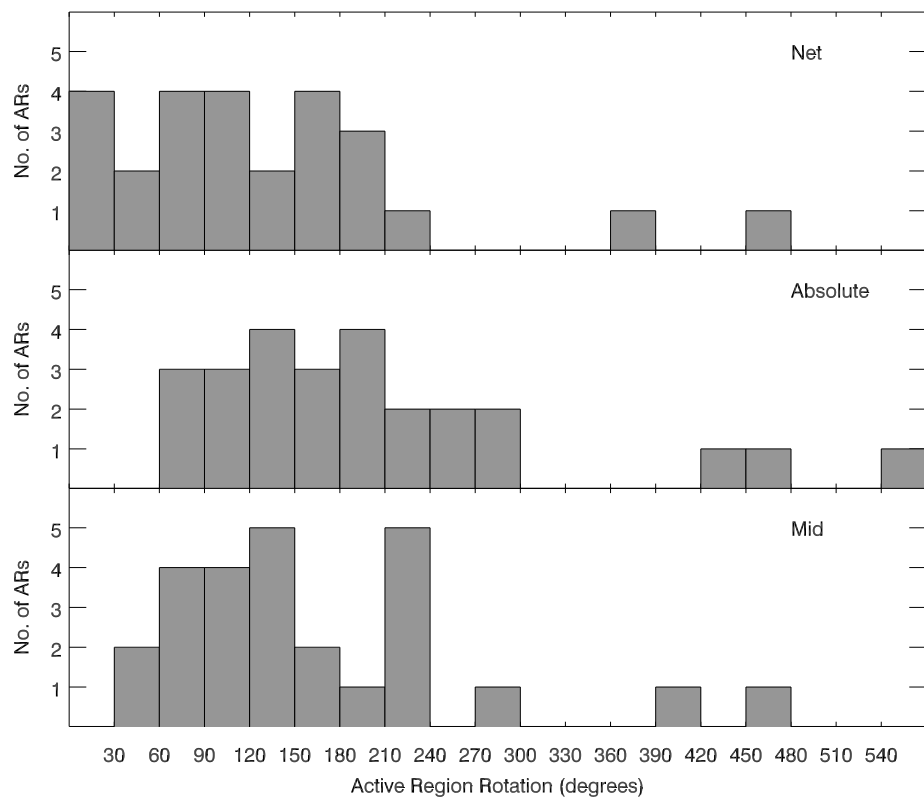
**Figure 4.4:** *The distribution of summed spot rotations. The top plot shows $R_{net}$, the middle plot shows $R_{abs}$, and the lower plot shows $R_{mid}$.*

**(a)** *Net rotation*

**(b)** *Mid rotation*



**(c)** *Absolute rotation*

**Figure 4.5:** *Radiated bolometric flare energy against rotation of all (large) spots in the active region. The black points represent regions where the X-class flare(s) occurs during the analysis period, the red points represent regions where the X-class flare(s) occurs before the analysis period, and the blue points represent regions where the X-class flare(s) occurs following the analysis period.*

$(R_{net} = 12° \pm 24°)$. AR11158 is the case study analysed in chapter 3.

The relationships between the radiated bolometric flare energy and different definitions of rotation are presented in figure 4.5.

CHAPTER 4

Bolometric flare energy against $R_{net}$ is shown in figure 4.5(a). The rotation values shown in this plot are likely to be an under-estimate of the true injection of twist into the corona, as opposite rotation directions exhibited by sunspots in the same region are assumed to cancel out.

The relationship between bolometric flare energy and $R_{mid}$ is presented in figure 4.5(b). Immediately obvious is the large uncertainty associated with the region AR11158, which is a result of the aforementioned large difference between the $R_{net}$ and $R_{abs}$ values of this region.

Shown in figure 4.5(c) is bolometric flare energy against $R_{abs}$. As the absolute rotation represents a maximum possible injection of twist into the corona, it is likely that some rotations will be an over-estimate of the actual value.

Of particular note is AR12192 which is a reasonably low rotator with an extremely high ($8.8 \times 10^{32}$ erg) bolometric flare energy. The amount of magnetic free energy injected into the solar corona from sunspot rotation is dependent upon the change in helicity, which is itself dependent upon the total magnetic flux of the region (equations 2.9 and 2.10). Regions with small sunspots may rotate by a large amount but inject the same amount of magnetic free energy as much larger sunspots that rotate by much less.

In all of the plots in figure 4.5, the black, blue and red points all cloud together. This indicates that the timing of the X-class flare is not an indication of how the active region will behave, in terms of both rotation and flaring activity.

Table 4.3 lists the active regions with their associated rotation energy from $R_{net}$, $R_{mid}$ and $R_{abs}$ as well as radiated bolometric flare energy. It is clear from this table that the majority of regions have a substantially larger energy injection from the absolute rotation than is output by bolometric flare radiation. Several regions have an extremely high energy injection from $R_{abs}$, namely AR11302, AR11429, AR11520, AR11944 and AR12192, which all have an injected energy of over $10^{33}$ erg. No

regions have a bolometric flare energy exceeding $10^{33}$ erg. Uncertainties associated with the net and absolute rotation energy range from $(0.01 - 5.64) \times 10^{32}$ erg, but are typically around $2 \times 10^{31}$ erg. Uncertainties associated with the mid rotation energy range from $(0.02 - 5.97) \times 10^{32}$ erg, but are typically in the region of $4 \times 10^{31}$ erg. The 45% uncertainty in the bolometric flare energy arises from the conversion between optically thin to the bolometric flare energy.

*Table 4.3:* *Energy properties for all X-class flare producing regions. The $R_{net}$, $R_{mid}$ and $R_{abs}$ columns represent the energy contributions from the respective rotation definitions. Flare Energy represents the energy contribution from bolometric flare radiation.*

| AR | Rot. Energy ($10^{32}$ erg) | | | Flare Energy ($\pm 45\%$) |
|---|---|---|---|---|
| | $R_{net}$ | $R_{mid}$ | $R_{abs}$ | $10^{32}$ erg |
| 11158 | -0.14 | 1.84 | 3.53 | 1.20 |
| 11166 | -0.27 | 1.01 | 1.75 | 1.04 |
| 11263 | -2.89 | 3.50 | 4.11 | 1.20 |
| 11283 | -0.72 | 0.73 | 0.73 | 1.30 |
| 11302 | 11.54 | 11.71 | 11.87 | 3.02 |
| 11339 | -2.61 | 4.31 | 6.01 | 2.97 |
| 11402 | 4.71 | 4.87 | 5.02 | 2.29 |
| 11429 | 13.69 | 13.74 | 13.78 | 3.39 |
| 11515 | 5.51 | 6.02 | 6.53 | 1.87 |
| 11520 | -17.05 | 17.18 | 17.30 | 1.87 |
| 11598 | 2.78 | 2.84 | 2.89 | 1.15 |
| 11748 | 0.06 | 0.08 | 0.09 | 0.73 |
| 11875 | 6.37 | 6.40 | 6.42 | 1.20 |
| 11882 | -0.04 | 0.18 | 0.32 | 0.21 |

| AR | \multicolumn{3}{c}{Rot. Energy ($10^{32}$ erg)} | Flare Energy ($\pm 45\%$) |
| | $R_{net}$ | $R_{mid}$ | $R_{abs}$ | $10^{32}$ erg |
|---|---|---|---|---|
| 11890 | 0.21 | 0.98 | 1.75 | 0.89 |
| 11893 | -1.76 | 1.79 | 1.82 | 1.51 |
| 11944 | -26.79 | 28.85 | 30.91 | 2.55 |
| 11990 | 1.52 | 1.52 | 1.52 | 0.21 |
| 12017 | -0.17 | 0.18 | 0.18 | 3.02 |
| 12035 | -1.25 | 1.29 | 1.32 | 2.40 |
| 12087 | -0.29 | 0.40 | 0.51 | 0.89 |
| 12158 | 8.36 | 8.36 | 8.36 | 3.44 |
| 12192 | 37.62 | 52.30 | 66.97 | 8.80 |
| 12242 | -4.20 | 4.69 | 5.18 | 3.28 |
| 12297 | -1.32 | 2.75 | 4.18 | 5.31 |
| 12339 | 0.73 | 1.19 | 1.64 | 4.74 |

**Table 4.3 –continued from previous page**

Figure 4.6 shows scatter plots of the radiated bolometric flare energy against the energy injected by $R_{net}$, $R_{mid}$ and $R_{abs}$ for all regions in the sample. The dashed line represents the energy balance line, where the output energy from the bolometric flare radiation is equal to the input energy from rotation. The red points represent active regions that give rise to one or more X-class flares prior to the analysis period, blue points represent regions that give rise to one or more X-class flares after the analysis period, and black points represent regions that give rise to all X-class flares during the analysis period (there are no regions in which a X-class flare occurs before and after the analysis period). These points are clouded together in each of these plots. In the net rotation plot (figure 4.6(a)), 12 regions are to the left of the energy

(a) Net rotation

(b) Mid rotation

(c) Absolute rotation
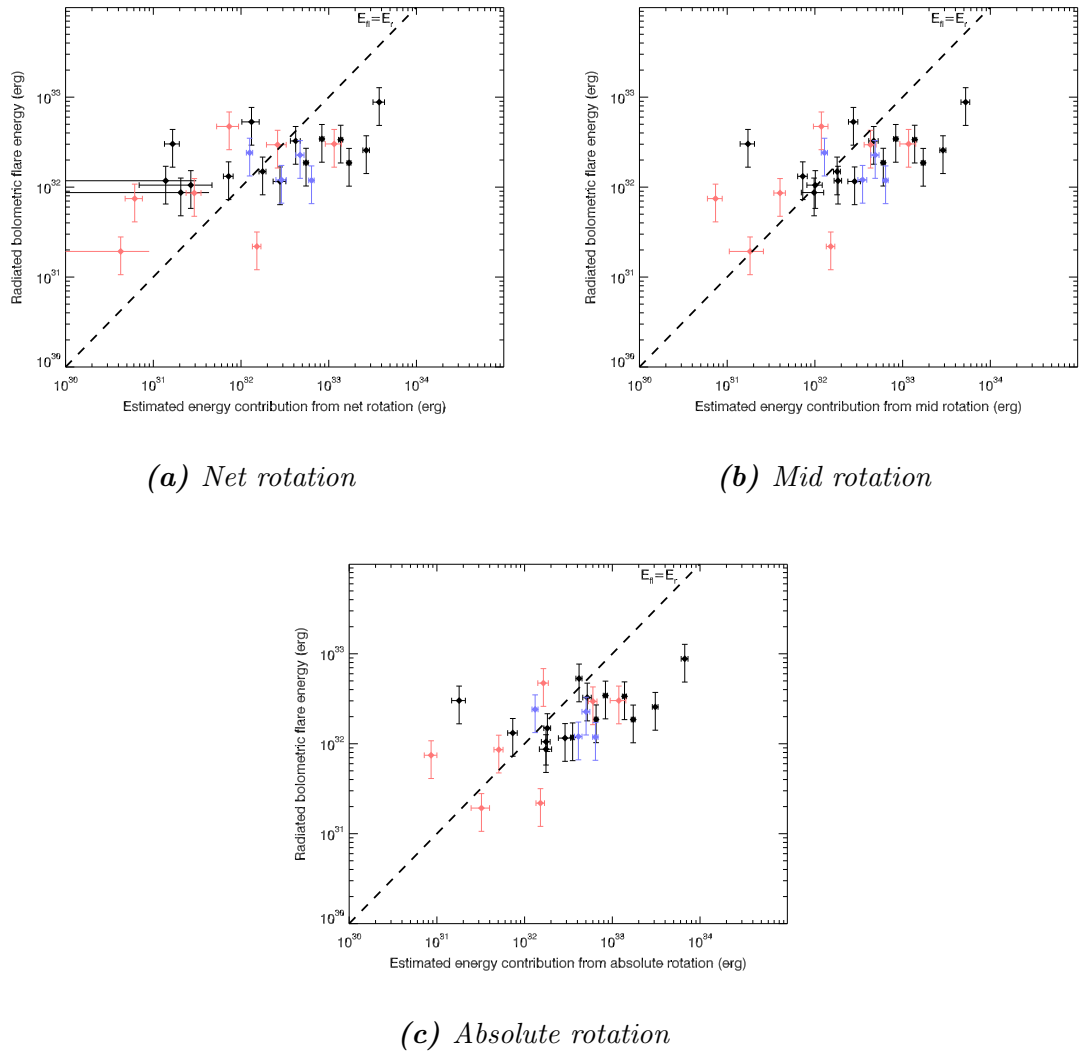
**Figure 4.6:** *Radiated bolometric flare energy against energy contribution from the three rotation definitions, $R_{net}$ (top left), $R_{mid}$ (top right) and $R_{abs}$ (lower middle). In each plot, the dashed line is the zero balance line where the bolometric flare energy would be equal to the input rotation energy. Red points are regions in which an X-class flare occurred prior to the analysis, blue regions indicate regions where an X-class flare occurred after the analysis period, and the black points are regions in which all X-class flares occurred during the analysis period.*

balance line, meaning they have a greater output energy than input from rotation. This drops to nine in the mid rotation plot (figure 4.6(b)) and seven in the absolute rotation plot (figure 4.6(c)).

In terms of general properties, all rotation definitions shown in figure 4.6 show a positive trend. The dashed diagonal line represents the 1:1 flare:rotation energy line, meaning points lying to the right of the line represent regions with a higher input energy from rotation than output energy radiated by flares. To the left of the line, the energy output by bolometric flare radiation is greater than that input by sunspot rotation. $R_{net}$ indicates a minimum possible energy injection from rotation. AR11748 is a particularly interesting region, as this region gives rise to four X-class solar flares on or close to the eastern limb, prior to the analysis period. It is likely that this region rotates onto the disc with a stored energy surplus, possibly supplied from sunspot rotation, prior to the beginning of the analysis period. AR12017 gives rise to one X-class flare during the analysis period, but only contains a single sunspot that meets the selection criteria. This sunspot rotates by $90° \pm 14°$, which is a significant amount of rotation, however, due to the very small size of the sunspot, the contribution of magnetic free energy from the rotation is low. Sunspot rotation alone does not provide enough energy to account for the flaring activity of this region, and so some of the energy must be provided from elsewhere.

The point with the highest radiated bolometric flare energy, AR12192, has shifted to fit into the overall trend, as opposed its position in figure 4.5. Although this region exhibits a relatively small $R_{abs}$ of just $120° \pm 11°$, the sunspots in this region are large, meaning the amount of flux undergoing rotation is high, leading to a larger injection of magnetic free energy.

In several cases where the X-class flare occurs after the analysis period, there is an excess of injected energy. Four regions in which the X-class flare occurs prior to the analysis period occupy the low-flare, low-rotation energy region of the plots

in figure 4.6, indicating that most activity (in terms of both flaring and sunspot rotation) has likely occurred prior to analysis, and the active region may rotate onto the disc containing an excess of stored energy before any analysis can be performed. In most cases, there is an excess of energy provided by sunspot rotation. This is a somewhat expected outcome, as there are many other energy loss mechanisms at play in active regions such as heating and coronal mass ejections. The local coronal magnetic field above the active region will also play a large part in generating solar flares, and in some cases the conditions above active regions may not be ideal for a large number of flares to occur, regardless of sunspot rotation magnitude.

This plot is somewhat reassuring in the sense that there are few outliers, and there seems to be a strong case for arguing that there is a relationship between the energy contributed from rotation and the radiated bolometric flare energy of active regions. it is important to note that the calculation of the energy contribution from sunspot rotation uses a simplistic approach to a complicated problem, as is the conversion from optically thin flaring radiation to bolometric.

## 4.6   Conclusions

X-class flare producing regions generally exhibit more sunspot rotation than the non-X-class flare producing regions studied in this chapter. This appears to be independent of magnetic complexity, as examples in figure 4.1 include regions with multiple sunspots (high magnetic complexity) and a region with a single sunspot (low magnetic complexity). X-class flare producing active regions also produce significantly more lower-class solar flares than the non-X-class regions observed here. Large solar flares (or large bursts of flaring activity) typically correspond to periods of fast sunspot rotation, and in the four X-class flare cases studied in detail here, the X-class flares follow significantly large amounts of rotation. It cannot be stated that sunspot rotation is the cause of every solar flare that is observed in these regions,

**Table 4.4:** *A summary of the statistical results in the context of energy from rotation. Essentially, high and low rotation energies are defined by the energy contribution from the $R_{abs}$ energy plot (figure 4.6(c)). If the region is to the right of the dashed line it is classed as high rotation energy, and to the left of the line is defined as low rotation energy. Only the high flare energy row is filled, as this sample is biased towards X-class flare producing regions.*

|                  | High Rotation Energy | Low Rotation Energy |
| ---------------- | :------------------: | :-----------------: |
| High Flare Energy | 19                  | 7                   |
| Low Flare Energy  | *                   | *                   |

as several flares appear to correspond to flux emergence.

Shown in figure 4.6 is the radiated bolometric flare energy against the energy contribution from rotation. A promising positive trend can be seen in this plot, indicating that there is indeed a relationship between energy contributed from sunspot rotation and radiated bolometric flare energy. Nineteen out of 26 of the X-class flare regions analysed gain enough energy from rotation to account for the radiated bolometric flare energy, and in some cases there is an excess of energy from sunspot rotation. This excess of energy may be used in other processes such as heating and coronal mass ejections. Conversely, there are some cases in which the bolometric flare energy is significantly higher than the absolute rotation energy. In these cases, other energy input processes are likely to have contributed to the flaring activity.

From the results presented in this chapter, there appears to be a strong relationship between sunspot rotation and solar flare production. This is not to say that sunspot rotation provides all of the energy for solar flares, as there are many other mechanisms that likely contribute. However, sunspot rotation certainly appears to be an important mechanism in providing the extra energy required to power the higher-energy/class solar flares.

CHAPTER 4

This sample consists only of high flare-energy active regions (defined here as any region associated with an X-class solar flare). However, to get a full picture of the relationship between sunspot rotation and solar flare production, low flare energy regions must also be studied. Table 4.4 illustrates the region of parameter space that the results from this work occupy, and the asterisks in the table indicate the parameter regions that need to be completed. The next step is to carry out a more representative statistical study of a typical distribution of active regions with a typical distribution of flare energies to test whether this relation holds for less eruptive regions. This table is purely illustrative of the regions studied in this chapter, and the overall goal is not to specifically fill in this table, but to study regions in all parts of parameter space that this represents.

This leads on to chapter 5, where an unbiased statistical sample based solely on a time period is compiled. This sample will consist of every sunspot that meets the selection criteria in a four-month window, from 1 May 2013 to 31 August 2013. This will allow the second row of table 4.4 to be filled, and will be the another step along the path to give insight into the relationship between sunspot rotation and solar flare production.

# Chapter 5

# Four-Month Statistical Sample

## 5.1 Introduction

Following the work carried out in chapter 4, it is apparent that an unbiased statistical sample is required to complete the parameter space illustrated in table 4.4. It is important to include low flare energy regions and their relation to sunspot rotation to determine whether the relationship observed for the X-class flare sample holds for lower energy active regions.

### 5.1.1 The Sample

To remove bias in the context of flaring activity, a four-month sample is defined based only on date and the selection criteria originally defined in chapter 3. A full list of the criteria is given below.

1. The sunspot must belong to an active region visible on the Sun by SDO between 1 May 2013 and 31 August 2013.

2. The sunspot umbra must contain more pixels than a circle of seven-pixel radius. The umbral size may drop to an area with an equivalent radius of between

six and seven pixels for a maximum of three hours, before returning to above seven pixels.

3. The sunspot must have an effective longitude of between -60° and 60° for the analysis period, as per equation 2.1.

4. The sunspot must not interact with another sunspot in such a way that interferes with the analysis (sunspot mergers for example). In this case, the sunspot is analysed up to the point of interaction.

5. The sunspot must meet criteria 2-4 for a period of at least 24 hours.

The time period of 1 May 2013 to 31 August 2013 is chosen for the sample as this covers a tractable period during solar maximum, increasing the number of eligible sunspots in the sample. Sunspots already on the disc on 1 May 2013 are only included if they are newly formed, or are near the eastern limb. Likewise, sunspots on the solar disc on 31 August 2013 are only analysed if they are close to dissipation or close to the western limb. This extra criterion is included in an attempt to get as close to a full transit across the disc as possible for each region. The sample comprises 59 sunspots contained within 38 active regions over the four months, giving a comparable sample size to that of the X-class flare sample. This sample includes ten active regions that do no flare.

## 5.2   Analysis

The analysis techniques used in this chapter mirror those used in chapter 4. Once the sunspots meet the selection criteria, the analysis tool described in chapter 2 is run on each one to calculate their rotation properties. The sunspots are grouped into their respective active regions, and their rotations are summed to obtain values of $R_{net}$, $R_{mid}$ and $R_{abs}$ for each active region in the sample, as described in chapter 4.

CHAPTER 5

Flare information for each region is obtained by querying the HEK (described in chapter 3), and the flares that occur during the active region's analysis period are integrated to obtain a total radiated bolometric flare energy for each region. The flares listed in table 5.1 include every flare associated with the active region, but only the energy from flares occurring during the analysis period is used to determine the total radiated bolometric flare energy for each active region.

The sunspot rotations for each active region are converted into an estimated energy contribution from sunspot rotation, using equations 2.8 through 2.10. These equations convert from sunspot size to sunspot flux, which is used in conjunction with total sunspot rotation to calculate the helicity. This helicity is then converted into an estimate of magnetic energy contribution from sunspot rotation.

## 5.3   Results

In this section, the results of the statistical sample are presented.

### 5.3.1   Rotation Properties

Figure 5.1 shows the distribution of sunspot rotations across the sample. The 30° bin size was selected to give the sample some resolution, and based on the study by Kazachenko et al. (2009) in which 32° rotation is claimed to provide enough energy for an M8.0 flare. The upper panel shows the net sunspot rotation and the lower panel shows the absolute sunspot rotation, as defined in chapter 3. Forty-six sunspots, roughly 78% of the sample, have less than 60° net rotation. Only six sunspots, 10% of the sample, have greater than 90° net rotation, with the highest net rotation value being (-)232°. In terms of absolute rotation, 36 sunspots (61% of the sample) have less than 60° rotation, and nine sunspots (15% of the sample) have more than 90° rotation. The largest absolute sunspot rotation in the sample
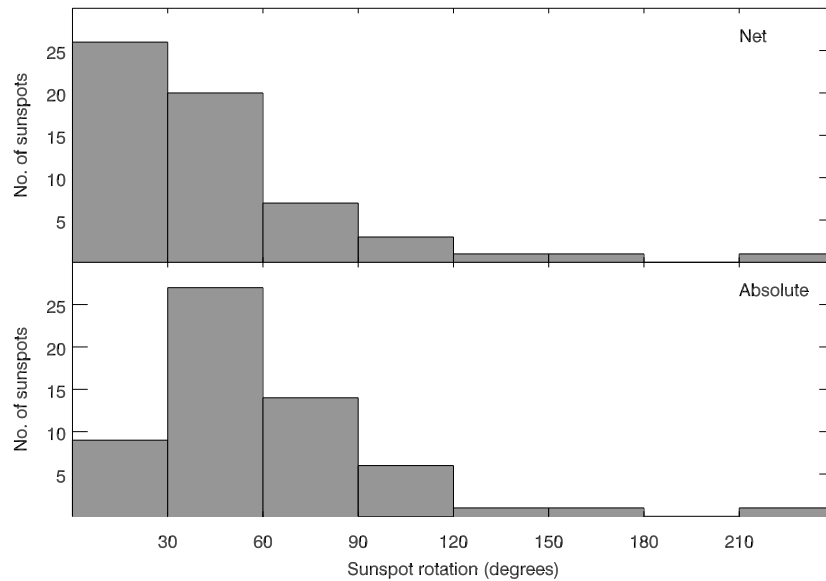
***Figure 5.1:*** *The distribution of sunspot rotations. The top plot shows the net sunspot rotation, and the lower plot shows the absolute sunspot rotation. 30° bins were selected as they gave the*

is 234° (corresponding to the largest net rotator in the top panel).

The rotations of each sunspot are combined into active region spot rotations, using the approach described in chapter 4. Table 5.1 lists the active region analysis periods, spot rotation values and the number of flares associated with each region. The uncertainties in $R_{abs}$ and $R_{net}$ rotation values range from 5° to 33°, with typical values around 15°. Uncertainty values associated with $R_{mid}$ are higher on average, ranging from 6° to 48°, but are typically around $20 - 25$°.

**Table 5.1:** *Active regions and their rotation and flare properties. The start and end columns indicate the start and end time of the analysis for each active region, $N_S$ is the number of sunspots, AR Rot $R_{net}$, $R_{mid}$ and $R_{abs}$ represent the net, mid and absolute rotation values, respectively. The flare columns indicate the number of C-, M- and X-class solar flares associated with the active region.*

| AR | Start | End | $N_S$ | Spot Rot (°) | | | Flares | | |
|---|---|---|---|---|---|---|---|---|---|
| | | | | $R_{net}$ | $R_{mid}$ | $R_{abs}$ | C | M | X |
| 11732 | 2013-05-01 00:00 | 2013-05-07 21:12 | 2 | 59 | 92 | 124 | 2 | 0 | 0 |
| 11734 | 2013-05-01 00:00 | 2013-05-09 20:54 | 2 | 104 | 190 | 276 | 11 | 0 | 0 |
| 11742 | 2013-05-10 14:54 | 2013-05-12 04:30 | 1 | 32 | 32 | 32 | 0 | 0 | 0 |
| 11743 | 2013-05-15 14:12 | 2013-05-16 03:12 | 1 | 27 | 31 | 34 | 1 | 0 | 0 |
| 11744 | 2013-05-12 05:30 | 2013-05-19 00:03 | 2 | -23 | 50 | 77 | 3 | 0 | 0 |
| 11745 | 2013-05-14 00:00 | 2013-05-21 10:30 | 2 | 17 | 54 | 91 | 2 | 0 | 0 |
| 11746 | 2013-05-13 00:00 | 2013-05-21 18:36 | 2 | -21 | 79 | 136 | 0 | 0 | 0 |
| 11747 | 2013-05-14 06:33 | 2013-05-16 21:36 | 1 | -33 | 47 | 61 | 0 | 0 | 0 |
| 11755 | 2013-05-22 12:00 | 2013-05-27 02:48 | 2 | -29 | 77 | 126 | 4 | 0 | 0 |
| 11756 | 2013-05-22 00:00 | 2013-05-30 02:00 | 1 | -151 | 159 | 168 | 12 | 0 | 0 |
| 11757 | 2013-05-27 00:00 | 2013-05-30 23:30 | 1 | -16 | 28 | 41 | 0 | 0 | 0 |
| 11762 | 2013-06-01 12:00 | 2013-06-06 09:03 | 4 | -263 | 303 | 342 | 3 | 1 | 0 |
| 11764 | 2013-06-02 16:00 | 2013-06-05 14:57 | 1 | 66 | 69 | 72 | 0 | 0 | 0 |
| 11765 | 2013-06-06 22:54 | 2013-06-08 18:33 | 2 | 18 | 43 | 69 | 0 | 0 | 0 |
| 11768 | 2013-06-14 00:27 | 2013-06-16 07:24 | 2 | 74 | 81 | 89 | 0 | 0 | 0 |
| 11770 | 2013-06-15 00:00 | 2013-06-21 00:09 | 1 | 8 | 30 | 52 | 0 | 0 | 0 |
| 11772 | 2013-06-18 00:00 | 2013-06-23 19:15 | 2 | -26 | 89 | 152 | 7 | 0 | 0 |
| 11775 | 2013-06-18 00:00 | 2013-06-25 23:59 | 2 | -94 | 101 | 108 | 9 | 0 | 0 |

**Continued on next page**

| | | | | Spot Rot (°) | | | Flares | | |
|---|---|---|---|---|---|---|---|---|---|
| AR | Start | End | $N_S$ | $R_{net}$ | $R_{mid}$ | $R_{abs}$ | C | M | X |
| 11776 | 2013-06-21 16:42 | 2013-06-23 12:00 | 1 | -36 | 36 | 36 | 1 | 0 | 0 |
| 11777 | 2013-06-22 00:00 | 2013-06-30 17:24 | 1 | -90 | 91 | 92 | 1 | 0 | 0 |
| 11785 | 2013-07-04 00:00 | 2013-07-11 00:33 | 2 | 52 | 76 | 99 | 25 | 0 | 0 |
| 11787 | 2013-07-06 00:00 | 2013-07-07 03:24 | 1 | 8 | 11 | 14 | 0 | 0 | 0 |
| 11791 | 2013-07-14 13:57 | 2013-07-16 20:45 | 1 | 27 | 36 | 46 | 5 | 0 | 0 |
| 11793 | 2013-07-16 00:00 | 2013-07-24 20:09 | 2 | 87 | 103 | 120 | 1 | 0 | 0 |
| 11800 | 2013-07-23 12:00 | 2013-07-27 23:59 | 2 | 114 | 120 | 126 | 7 | 0 | 0 |
| 11801 | 2013-07-25 00:00 | 2013-08-02 22:45 | 1 | -24 | 50 | 76 | 1 | 0 | 0 |
| 11805 | 2013-07-27 13:00 | 2013-07-29 07:39 | 1 | -16 | 24 | 32 | 1 | 0 | 0 |
| 11806 | 2013-08-01 22:42 | 2013-08-05 15:51 | 1 | -92 | 94 | 96 | 0 | 0 | 0 |
| 11808 | 2013-07-30 12:00 | 2013-08-07 16:51 | 1 | -121 | 130 | 139 | 0 | 0 | 0 |
| 11809 | 2013-08-01 12:00 | 2013-08-09 08:36 | 1 | -41 | 49 | 58 | 0 | 0 | 0 |
| 11810 | 2013-08-02 12:00 | 2013-08-06 19:06 | 1 | 30 | 47 | 64 | 0 | 0 | 0 |
| 11817 | 2013-08-12 22:48 | 2013-08-17 16:21 | 2 | -42 | 93 | 143 | 7 | 0 | 0 |
| 11818 | 2013-08-11 12:00 | 2013-08-19 19:42 | 1 | -65 | 76 | 87 | 8 | 2 | 0 |
| 11823 | 2013-08-17 00:00 | 2013-08-18 00:06 | 1 | -5 | 9 | 13 | 0 | 0 | 0 |
| 11824 | 2013-08-17 15:48 | 2013-08-20 01:18 | 2 | -91 | 104 | 116 | 0 | 0 | 0 |
| 11825 | 2013-08-19 09:30 | 2013-08-22 06:03 | 1 | -44 | 53 | 63 | 1 | 0 | 0 |
| 11827 | 2013-08-20 00:00 | 2013-08-21 07:09 | 1 | -10 | 16 | 21 | 0 | 0 | 0 |
| 11835 | 2013-08-27 00:00 | 2013-08-31 23:59 | 3 | -25 | 46 | 66 | 0 | 0 | 0 |

**Table 5.1** –continued from previous page

The most apparent feature of table 5.1 is the lack of flares in the sample. The majority of the regions give rise to no M-class flares and fewer than 10 C-class flares.

CHAPTER 5

The most active regions are AR11785 with 25 C-class flares and AR11818 with eight C-class flares and two M-class flares. Out of the 104 active regions classified on the solar disc in this time period, 39 (one region, AR11748, is an X-class flare producing region, and is already included in the X-class flare sample, and the regions AR11770 and AR11772 are presented in chapter 4 as low flare-energy comparison regions) contain sunspots that meet the size criteria. Twenty-five of the 65 regions without sunspots large enough to analyse give rise to at least one C-class flare, but the resolution of current instrumentation is too low to usefully analyse the sunspot (or pore) rotation of these regions. Some regions also emerged as they traversed the western limb, and some dissipated as they traversed the eastern limb, meaning they did not meet the sunspot selection criteria.

The gaps in terms of active region number in the table correspond to active regions which either contain no sunspots, or regions in which the sunspots do not meet the size criteria. There is one active region in particular, AR11739, which gives rise to 18 C-class flare and 2 M-class flares. This is a region that contains a large amount of quite diffuse flux, such that no sunspot in the region evolves to be large enough for analysis.

Shown in figure 5.2 are the spot rotations for the $R_{net}$ (top), $R_{mid}$ (middle), and $R_{abs}$ (bottom) rotation definitions. The most striking feature in the $R_{net}$ plot is the abundance of active regions with a rotation of less than 60°. Twenty-seven out of 38 (equating to 71%) active regions in the sample have less than 60° rotation, while only nine active regions (24%) have greater than 90° rotation. The highest net rotation in the sample is AR11762 at (-)263° $\pm$ 25°.

The distribution of $R_{mid}$ values in the sample is shifted towards the higher end. However, half of the regions (19 out of 38) still exhibit less than 60° rotation. Twelve out of the 38 regions (32%) have higher than 90° rotation, with the highest $R_{mid}$ value in the sample once again belonging to AR11762, with a value of 303° $\pm$ 36°.
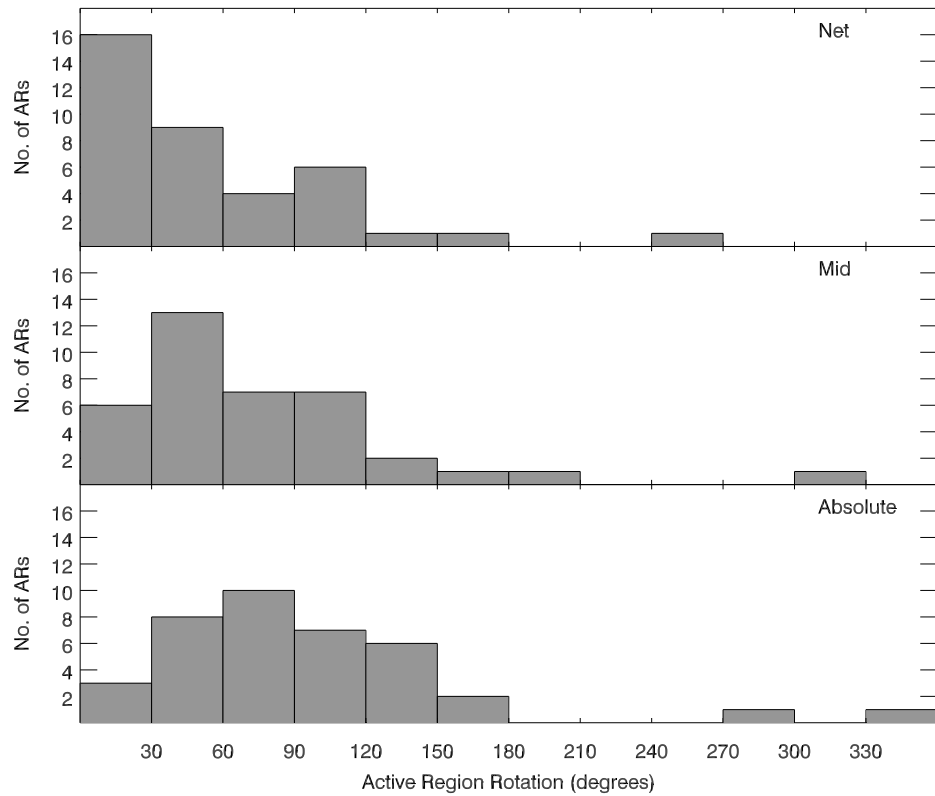
**Figure 5.2:** *The distribution of spot rotations in the statistical sample. The top plot shows the distribution of $R_{net}$, the middle plot shows the distribution of $R_{mid}$, and the lower plot shows the distribution of $R_{abs}$.*

The $R_{abs}$ distribution, shown in the lower panel of figure 5.2, is centred about the 60-90° range. Only eleven regions (29%) have a $R_{abs}$ value lower than 60°, whereas 17 regions (45%) have a $R_{abs}$ above 90°. AR11762 once again has the highest value, with $R_{abs} = 342° \pm 25°$.

The spot rotations against bolometric flare energy are presented in figure 5.3. In each case, the y-axis represents the radiated bolometric flare energy of the active region and the x-axis represents $R_{net}$ (upper left), $R_{mid}$ (upper right) and $R_{abs}$ (lower middle) rotation values.

Particularly in the mid and absolute rotation plots, there appears to be a convincing positive trend, neglecting the active regions which do not flare during the analysis period (displayed in the box at the bottom of the plots). The contribution of helicity from sunspot rotation is dependent upon the rotation and the square of the flux, such that the amount of flux being twisted is the most important factor. The energy contribution from sunspot rotation for each active region is presented in section 5.3.2.

## 5.3.2   Energy Properties

The energy properties of the active regions are listed in table 5.2. This table lists the energy contributions from the $R_{net}$, $R_{mid}$ and $R_{abs}$ rotations. The net rotation energy indicates a minimum possible amount of energy injected, but also indicates the direction of the helicity that contributes this energy. Negative net rotation energy indicates clockwise helicity, whereas positive indicates anti-clockwise helicity. Uncertainties in the energy values range from $10^{30}$ erg to $5 \times 10^{31}$ erg, with typical values of $10^{31}$ erg. The uncertainty in the bolometric flare energy of 45% arises form the conversion to bolometric flare energies from optically thin.
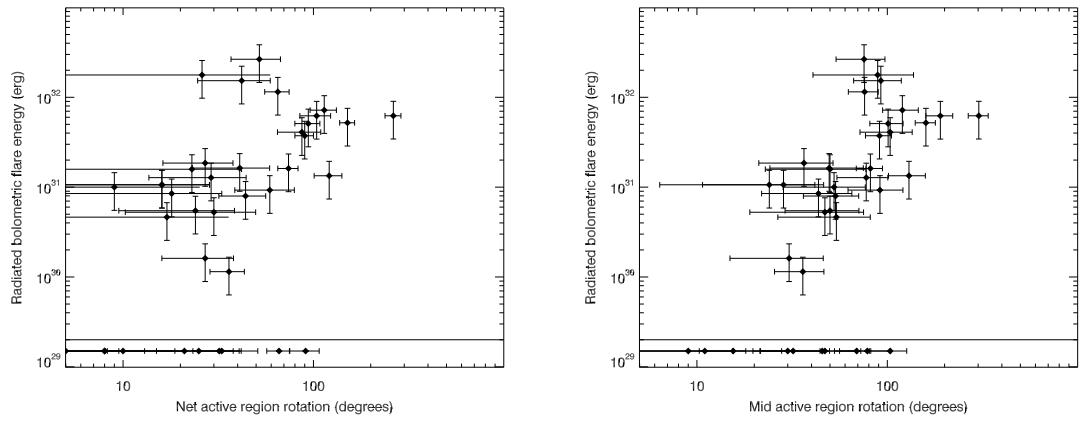
(a) Net rotation



(b) Mid rotation
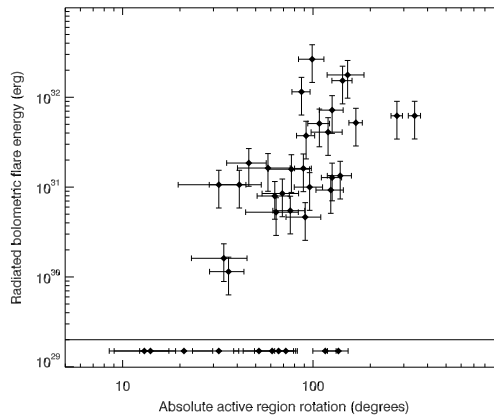


(c) Absolute rotation

**Figure 5.3:** *Radiated bolometric flare energy against spot rotation profiles for the four-month statistical sample. Regions that do not flare during the analysis period are presented in the box at the bottom of the plots.*

**Table 5.2:** *Energy properties for all statistical sample regions. Rot. Energy $R_{net}$, $R_{mid}$ and $R_{abs}$ columns represent the energy input from the net, mid and absolute rotation respectively. Flare Energy represents the energy output from bolometric flare radiation.*

| AR | Rot. Energy ($10^{32}$ erg) | | | Flare Energy ($\pm$ 45%) |
|---|---|---|---|---|
| | $R_{net}$ | $R_{mid}$ | $R_{abs}$ | ($10^{32}$ erg) |
| 11732 | 0.07 | 0.13 | 0.18 | 0.10 |
| 11734 | 7.64 | 8.64 | 9.64 | 0.62 |
| 11742 | 0.03 | 0.03 | 0.03 | 0.00 |
| 11743 | 0.01 | 0.01 | 0.01 | 0.02 |
| 11744 | -0.01 | 0.01 | 0.02 | 0.16 |
| 11745 | 0.31 | 0.54 | 0.76 | 0.47 |
| 11746 | -0.35 | 0.59 | 0.82 | 0.00 |
| 11747 | -0.02 | 0.04 | 0.05 | 0.00 |
| 11755 | 0.09 | 0.15 | 0.21 | 0.10 |
| 11756 | -0.87 | 0.92 | 0.97 | 0.52 |
| 11757 | -0.02 | 0.04 | 0.06 | 0.10 |
| 11762 | -1.84 | 1.96 | 2.07 | 0.62 |
| 11764 | 0.15 | 0.16 | 0.17 | 0.00 |
| 11765 | -0.05 | 0.09 | 0.13 | 0.10 |
| 11768 | 0.43 | 0.48 | 0.53 | 0.16 |
| 11770 | 0.01 | 0.05 | 0.09 | 0.00 |
| 11772 | -0.06 | 0.14 | 0.22 | 1.77 |
| 11775 | -0.70 | 0.76 | 0.82 | 0.52 |
| 11776 | -0.07 | 0.07 | 0.07 | 0.01 |

**Continued on next page**

| Table 5.2 –continued from previous page | | | |
|---|---|---|---|
| AR | Rot. Energy ($10^{32}$ erg) | | Flare Energy ($\pm$ 45%) |
| | $R_{net}$ | $R_{mid}$ | $R_{abs}$ | ($10^{32}$ erg) |
| 11777 | -1.06 | 1.07 | 1.08 | 0.36 |
| 11785 | 1.03 | 1.21 | 1.39 | 2.66 |
| 11787 | 0.02 | 0.03 | 0.04 | 0.00 |
| 11791 | 0.03 | 0.04 | 0.05 | 0.21 |
| 11793 | 0.08 | 0.14 | 0.19 | 0.42 |
| 11800 | 0.33 | 0.33 | 0.33 | 0.73 |
| 11801 | -0.06 | 0.14 | 0.22 | 0.05 |
| 11805 | -0.01 | 0.02 | 0.02 | 0.10 |
| 11806 | -0.11 | 0.11 | 0.11 | 0.10 |
| 11808 | -0.13 | 0.14 | 0.15 | 0.16 |
| 11809 | -0.05 | 0.07 | 0.08 | 0.16 |
| 11810 | 0.01 | 0.02 | 0.02 | 0.05 |
| 11817 | -0.48 | 0.52 | 0.55 | 1.51 |
| 11818 | -1.46 | 1.74 | 2.02 | 1.15 |
| 11823 | -0.02 | 0.04 | 0.05 | 0.00 |
| 11824 | -0.05 | 0.06 | 0.07 | 0.00 |
| 11825 | -0.04 | 0.05 | 0.06 | 0.10 |
| 11827 | -0.01 | 0.01 | 0.01 | 0.00 |
| 11835 | -0.15 | 0.27 | 0.38 | 0.00 |

The tabulated energies are plotted in figure 5.4. In each case, the y-axis values represent the radiated bolometric flare energy. The x-axes represent the energy contribution from the net (upper left), mid (upper right) and absolute (lower middle)

rotation. The dashed line indicates where the bolometric flare energy is equal to the rotation energy. As such, any points to the right of the line have enough energy from rotation to account for the radiated bolometric flare energy, and points to the left of the line do not. The active regions represented by the points in the box at the bottom of the plot do not flare during the analysis period. The majority (seven out of ten) of these non-flaring regions have an input energy from sunspot rotation of less than $10^{31}$ erg, and all of them have an input energy of less than $10^{32}$ erg. This implies that the energy injected into the system could either not be substantial enough to trigger any instabilities with the current coronal conditions, or perhaps a significant event occurred behind the limb, and the rotation being observed is a slow relaxing of the magnetic field.

Each plot in figure 5.4 shows a convincing trend between radiated flare energy and energy contributed from sunspot rotation. In the $R_{mid}$ and $R_{abs}$ plots, the points appear to show a positive trend clustered around the 1:1 line, which is particularly interesting, as this suggests that there is a strong relationship between input energy from sunspot rotation and output bolometric flare energy for low-energy active regions.

There are ten active regions that do not produce any solar flares, but contain rotating sunspots that provide significant ($10^{30}$ to $10^{32}$ erg) input energy. This energy may be stored in the active region magnetic field and be used later, or it may be used in other processes, such as coronal mass ejections, or perhaps coronal heating. Conversely, the sunspot rotation observed in these regions may be an untwisting of the magnetic field following flare events prior to the regions meeting the selection criteria.

(a) $R_{net}$



(b) $R_{mid}$



(c) $R_{abs}$
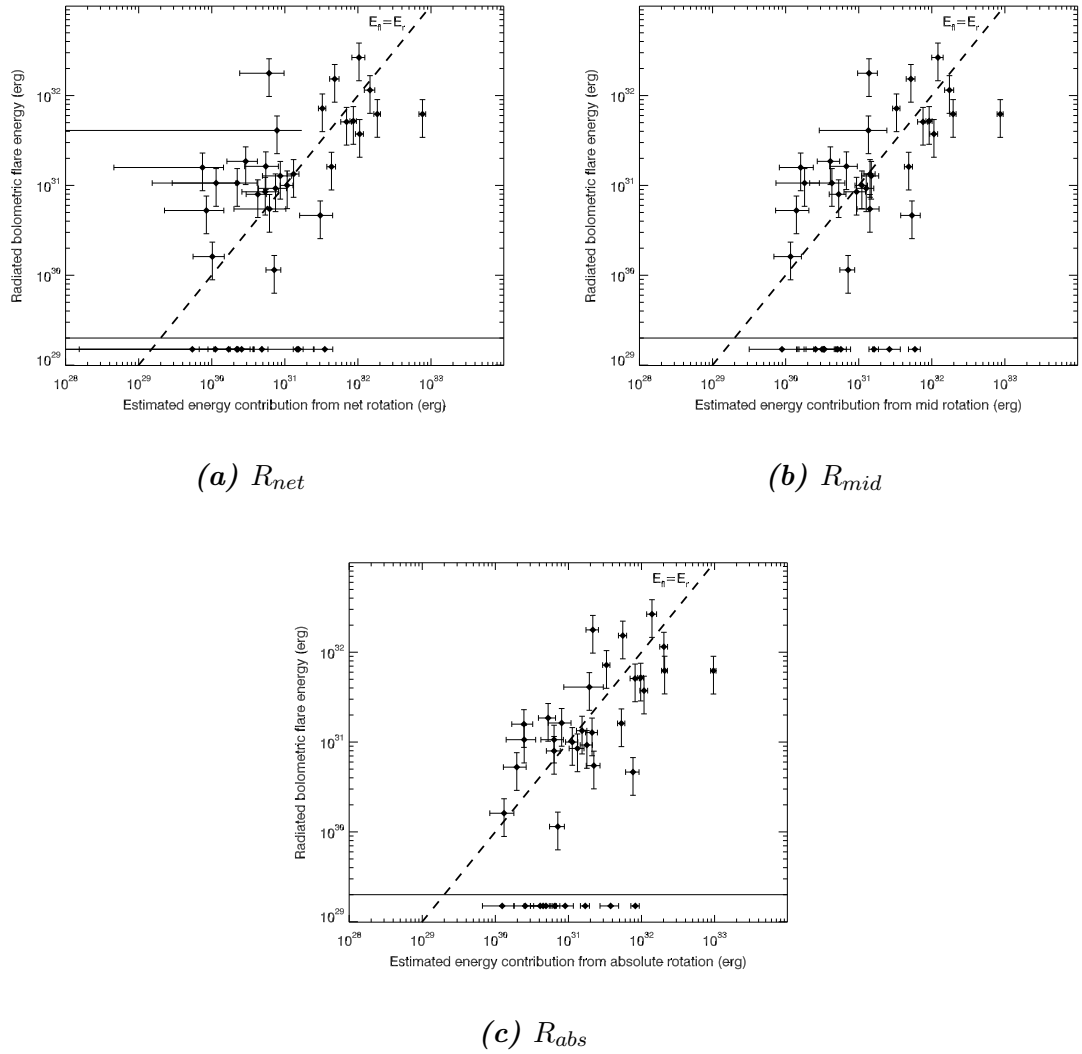
**Figure 5.4:** *Radiated bolometric flare energy against energy contribution from the three rotation definitions, $R_{net}$ (top left), $R_{mid}$ (top right) and $R_{abs}$ (lower middle). In each plot, the dashed line is the zero balance line where the bolometric flare energy is equal to the input rotation energy.*

CHAPTER 5

## 5.4   Conclusions

This chapter presented the rotational properties of all sunspots that meet the selection criteria observed by SDO/HMI between 1 May 2013 and 31 August 2013, to create an unbiased sample.

A large majority of the sunspots within the sample exhibit less than 60° net and absolute rotation, and very few exhibit more than 90°. This skew towards lower rotation values in this sample is reassuring, as it implies that the sunspots in these lower flare energy regions do not exhibit much rotation.

The variation in spot rotation is more dependent upon the rotation definition. The vast majority (71%) of active regions have a net rotation of less than 60°, and very few (24%) exihibit more than 90° net rotation. Half of the regions exhibit less than 60° middle rotation, with 12 out of the 38 regions (32%) exhibiting more than 90°. The story changes drastically with the absolute spot rotation, where only 11 out of 38 regions (29%) exhibit less than 60° rotation. The distribution peaks in the 60-90° absolute rotation range, and almost half (45%) of the regions exhibit over 90° absolute rotation. There is a convincing trend between radiated bolometric flare energy and spot rotation (figure 5.3).

The energy contributed from sunspot rotation is dependent upon the flux squared, and as such, the actual magnitude of rotation is not an accurate representation of the energy input into the system. The radiated bolometric flare energy against energy contribution from rotation plots in figure 5.4 shows a much more convincing relationship, particularly in the mid and absolute cases where the points are clustered around the 1:1 line.

To draw conclusions regarding the relationship between sunspot rotation and solar flares, these samples can be combined and analysed as a complete set. This is the focus of chapter 6, which pulls together the work presented thus far in this thesis to understand how sunspot rotation and flaring activity are interlinked.

# Chapter 6

# The Link Between Sunspot Rotation and Solar Flares

## 6.1  Introduction

This chapter consolidates the results from the statistical samples with the goal of determining the relationship between sunspot rotation and solar flares. In particular, it focuses on how the energy contribution from rotation compares to the radiated bolometric flare energy for each active region. Within the two samples combined, and any overlaps discounted, there are a total of 135 sunspots within 64 active regions.

## 6.2  Results

An important measure pertaining to how important a role sunspot rotation plays in providing the energy reservoir for solar flares is the amount of energy contributed from sunspot rotation compared to the amount of radiated bolometric flare energy. Table 6.1 lists the percentage of bolometric flare energy to rotation energy for the energy contribution from each definition of rotation. As such, a value of 100% means

CHAPTER 6

the energy values are equal, above 100% indicates there is more radiated bolometric flare energy, and a value below 100% indicates there is more energy contributed from sunspot rotation than radiated bolometric flare energy. These percentages are calculated over the whole analysis period for each region. Any values quoted as zero are regions in which there was no flaring activity over the analysis period.

***Table 6.1:*** *This table lists the bolometric flare energy as a percentage of the rotation energy for each definition of rotation for each active region from both samples. Cases where the values are zero are regions from which no flares were observed during the analysis period. Values of greater than 100 represent cases where the bolometric flare energy is greater than the energy contribution from rotation.*

| | X-Class Sample | | | | 4-Month Sample | | |
|---|---|---|---|---|---|---|---|
| AR | $E_{fl}$ as % of $E_R$ | | | AR | $E_{fl}$ as % of $E_R$ | | |
| | $R_{net}$ | $R_{mid}$ | $R_{abs}$ | | $R_{net}$ | $R_{mid}$ | $R_{abs}$ |
| 11158 | 849 | 62 | 31 | 11732 | 125 | 73 | 52 |
| 11166 | 391 | 104 | 62 | 11734 | 10 | 5 | 5 |
| 11263 | 42 | 36 | 31 | 11742 | 0 | 0 | 0 |
| 11283 | 182 | 182 | 182 | 11743 | 156 | 141 | 125 |
| 11302 | 26 | 26 | 26 | 11744 | 2120 | 984 | 641 |
| 11339 | 115 | 68 | 47 | 11745 | 16 | 10 | 5 |
| 11402 | 47 | 47 | 47 | 11746 | 0 | 0 | 0 |
| 11429 | 26 | 26 | 26 | 11747 | 0 | 0 | 0 |
| 11515 | 31 | 31 | 26 | 11755 | 146 | 83 | 62 |
| 11520 | 10 | 10 | 10 | 11756 | 62 | 57 | 52 |
| 11598 | 42 | 42 | 42 | 11757 | 479 | 245 | 166 |
| 11748 | 1213 | 1010 | 865 | 11762 | 31 | 31 | 31 |

**Continued overleaf**

**Table 6.1 –continued**

| X-Class Sample | | | | 4-Month Sample | | | |
|---|---|---|---|---|---|---|---|
| AR | $E_{fl}$ as % of $E_R$ | | | AR | $E_{fl}$ as % of $E_R$ | | |
| | $R_{net}$ | $R_{mid}$ | $R_{abs}$ | | $R_{net}$ | $R_{mid}$ | $R_{abs}$ |
| 11875 | 21 | 21 | 21 | 11764 | 0 | 0 | 0 |
| 11882 | 453 | 104 | 57 | 11765 | 156 | 89 | 62 |
| 11890 | 422 | 89 | 52 | 11768 | 36 | 31 | 31 |
| 11893 | 83 | 83 | 83 | 11770 | 0 | 0 | 0 |
| 11944 | 10 | 10 | 10 | 11772 | 2916 | 1281 | 812 |
| 11990 | 16 | 16 | 16 | 11775 | 73 | 68 | 62 |
| 12017 | 1818 | 1750 | 1682 | 11776 | 16 | 16 | 16 |
| 12035 | 193 | 187 | 182 | 11777 | 36 | 36 | 36 |
| 12087 | 292 | 214 | 167 | 11785 | 255 | 219 | 193 |
| 12158 | 42 | 42 | 42 | 11787 | 0 | 0 | 0 |
| 12192 | 21 | 16 | 16 | 11791 | 635 | 453 | 349 |
| 12242 | 78 | 68 | 62 | 11793 | 526 | 302 | 214 |
| 12297 | 401 | 193 | 125 | 11800 | 219 | 219 | 219 |
| 12339 | 645 | 401 | 286 | 11801 | 89 | 36 | 26 |
| | | | | 11805 | 927 | 583 | 427 |
| | | | | 11806 | 94 | 89 | 89 |
| | | | | 11808 | 104 | 94 | 89 |
| | | | | 11809 | 297 | 240 | 203 |
| | | | | 11810 | 624 | 375 | 266 |
| | | | | 11817 | 318 | 297 | 276 |
| | | | | 11818 | 78 | 68 | 57 |
| | | | | 11823 | 0 | 0 | 0 |

**Continued overleaf**

| Table 6.1 –continued | | | | | | | |
|---|---|---|---|---|---|---|---|
| X-Class Sample | | | | 4-Month Sample | | | |
| AR | $E_{fl}$ as % of $E_R$ | | | AR | $E_{fl}$ as % of $E_R$ | | |
| | $R_{net}$ | $R_{mid}$ | $R_{abs}$ | | $R_{net}$ | $R_{mid}$ | $R_{abs}$ |
| | | | | 11824 | 0 | 0 | 0 |
| | | | | 11825 | 187 | 151 | 125 |
| | | | | 11827 | 0 | 0 | 0 |
| | | | | 11835 | 0 | 0 | 0 |

The tabulated values are presented as histograms in figure 6.1 for clarity, with the dark grey portions representing the X-class sample and the light grey representing the four-month sample. Regions with no flaring activity are not included in figure 6.1, meaning these ten active regions are essentially excluded from the sample. If these regions were to be included, the number of regions within the 0-20% range for the net, mid and absolute histograms would be 16, 17 and 17 respectively (up from 6, 7 and 7). There are some regions in which the bolometric radiated bolometric flare energy is substantially higher than the energy contribution from sunspot rotation. One example is AR11772, where the radiated bolometric flare energy is 2916% of the energy contribution from the net rotation, and 812% of the energy contribution from the absolute rotation. AR12017 from the X-class flare sample exhibits 1818% more radiated bolometric flare energy than energy contribution from the absolute rotation.

A common trend over all of the histograms is that there are more regions in the 200%+ range than in any other range. The distribution of energy inputs compared to bolometric flare energies from absolute rotation is weighted more to the lower end, implying that, in the majority of cases, more energy is input by the absolute
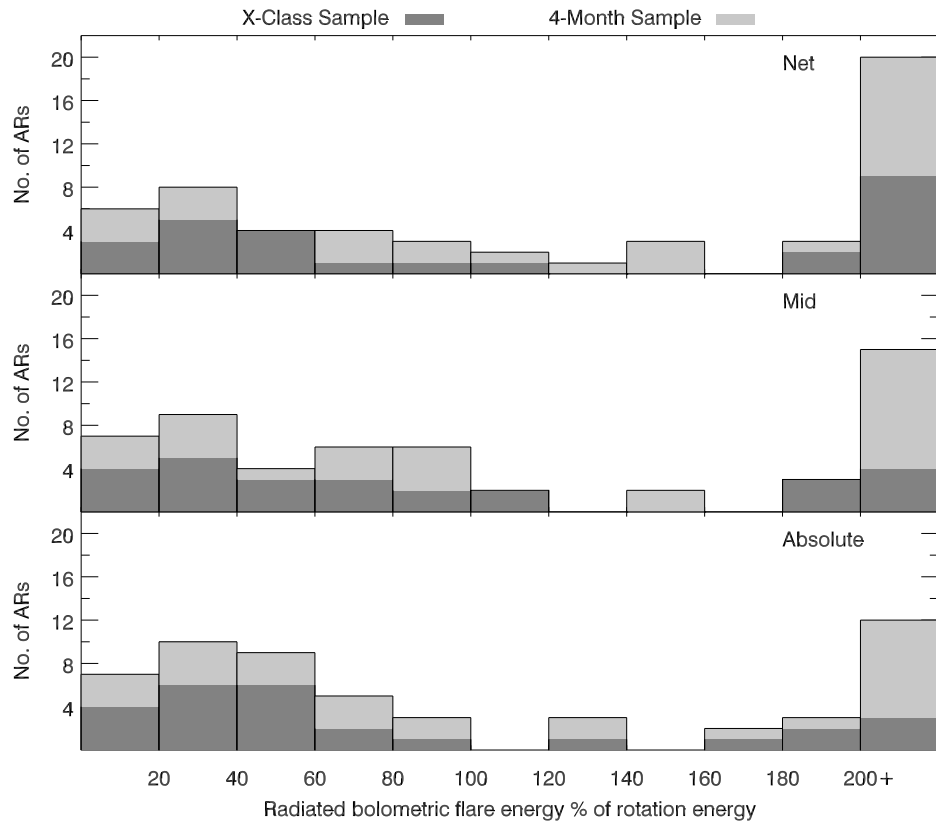
**Figure 6.1:** *Histograms of the distributions of bolometric flare energy as a percentage of rotation energy. The light grey shaded regions represent the four-month sample and the dark grey shaded regions represent the X-class flare sample. Histograms are shown for the net, mid, and absolute rotations.*

rotation than output by the bolometric flare radiation.

In terms of overall distributions, the percentage of radiated bolometric flare energy compared to the net sunspot energy is the most spread distribution, with values filling the full 200%+ range. The distribution pertaining to the mid rotation energy is shifted to the lower end, as is the distribution pertaining to the absolute rotation energy, but to an even greater extent. This is to be expected, as the energy from the net rotation represents a minimum and the energy contribution from the absolute rotation represents a maximum.

Twenty-nine (45%) regions have a greater radiated bolometric flare energy than net sunspot rotation energy, 22 (34%) regions have a greater radiated bolometric flare energy than mid sunspot rotation energy, and 20 (31%) regions have a greater radiated bolometric flare energy than absolute sunspot rotation energy. On average, even in the scenario where the minimum amount if energy is input from sunspot rotation (net spot rotation), over half of the active regions over both samples have enough energy input from sunspot rotation to account for the output from the bolometric flare radiation. Over two-thirds of active regions have enough input energy from the maximum possible amount of sunspot rotation (absolute spot rotation) to account for the bolometric flare radiation.

Figure 6.2 shows the cumulative energy distributions (CDFs) for the net, mid and absolute rotations. The 200+ bin has been excluded from the plot as the rotation plays a significantly diminished role in these cases, and is a limit rather than a data-point. A two-sample Kolmogorov-Smirnov (K-S) test is performed, comparing the X-class flare and 4-month sample CDFs for each definition of rotation. The K-S statistic ($D$) is defined as the maximum difference between the CDFs, and to determine whether the two populations are from the same underlying distribution, the K-S statistic is compared to the critical value ($D_c$). The critical value is calculated
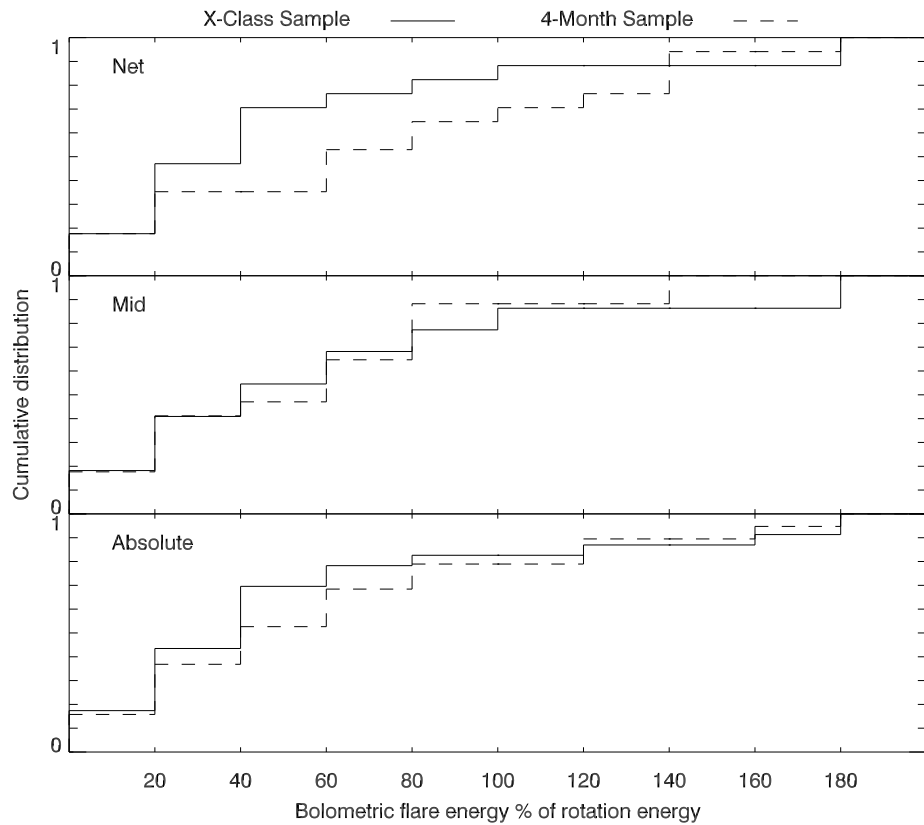
**Figure 6.2:** *Cumulative histograms of the distribution of bolometric flare energy as a percentage of the rotation energy. The solid line represents the distribution of regions from the X-class flare sample, and the dashed line represents the distribution of regions from the four-month statistical sample.*

as

$$D_c = c(\alpha)\sqrt{\frac{m+n}{mn}}, \tag{6.1}$$

where $m$ and $n$ are the sample sizes of the two populations, and $c(\alpha)$ is calculated based on the significance level, $\alpha$. For this test, a significance level of $\alpha = 0.05$ is used, giving a $c(\alpha)$ value of 1.36 (this value is determined from look-up tables of common K-S test significance levels). If the K-S statistic is less than the critical value, the two populations (in this case the X-class flare sample and the 4-month sample) are likely from the same underlying distribution. For the net rotation, the K-S statistic is $D_{net} = 0.35$, and the critical value is $D_{c,net} = 0.47$. For the mid rotation, $D_{mid} = 0.14$ and $D_{c,mid} = 0.44$, and for the absolute rotation, $D_{abs} = 0.17$ and $D_{c,abs} = 0.42$. For each definition of rotation, the K-S statistic is below the critical value. This indicates, to a 95% confidence level, that the two populations are from the same underlying distribution. As such, it is reasonable to conclude that the underlying physics relating sunspot rotation and bolometric flare energy does not discriminate between high or low flare energy active regions.

Figures 6.3, 6.4 and 6.5 show scatter plots of radiated bolometric flare energy against net, mid and absolute sunspot rotation energy contributions, respectively. The red filled diamonds represent the X-class flare sample, and the blue filled triangles represent the statistical sample. The thick, dashed diagonal line represents the values at which the radiated bolometric flare energy is equal to the rotation, the two dotted diagonal lines represent the values where the bolometric flare energy is equal to 10% and 1% of the rotation energy (labelled in the figures). The ten regions that do not flare within the analysis period are confined to the box at the bottom of these plots.

The relationship between radiated bolometric flare energy and energy contribution from net sunspot rotation is presented in figure 6.3. There is a distinct positive trend between the radiated bolometric flare energy and rotation energy, clustered
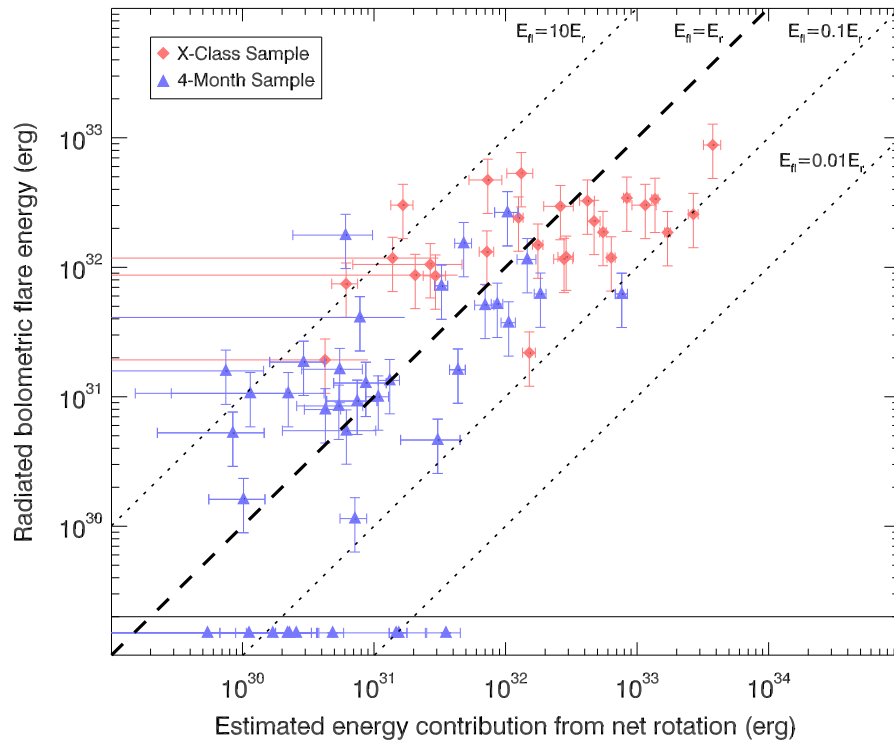
**Figure 6.3:** *Bolometric flare energy against net rotation energy. The dashed line indicates where radiated bolometric flare energy is equal to the rotation energy. The dotted lines represent where the bolometric flare energy is a 10% and 1% of the rotation energy, as labelled in the plot.*
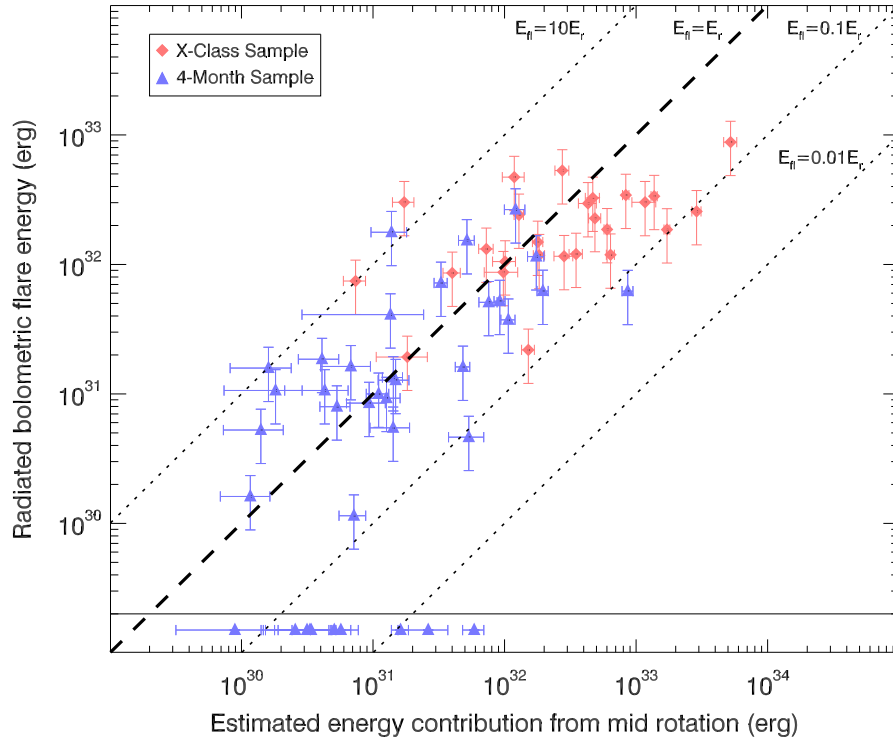
***Figure 6.4:*** *Bolometric flare energy against mid rotation energy. The dashed line indicates where radiated bolometric flare energy is equal to the rotation energy. The dotted lines represent where the bolometric flare energy is a 10% and 1% of the rotation energy, as labelled in the plot.*

around the 1:1 line. The net rotation represents a minimum amount of rotation for each active region, and as such, more points are located to the left of the 1:1 line. There is a divide between the majority of the X-class flare sample regions and the four-month sample regions. The vast majority of regions populate the 10%+ region of figure 6.3.

The plot of radiated bolometric flare energy against energy contribution from the mid rotation is shown in figure 6.4. The positive trend is apparent in this plot, with the points divided almost equally between the left and right of the 1:1 line. The divide between the X-class flare sample and four-month sample is also apparent in
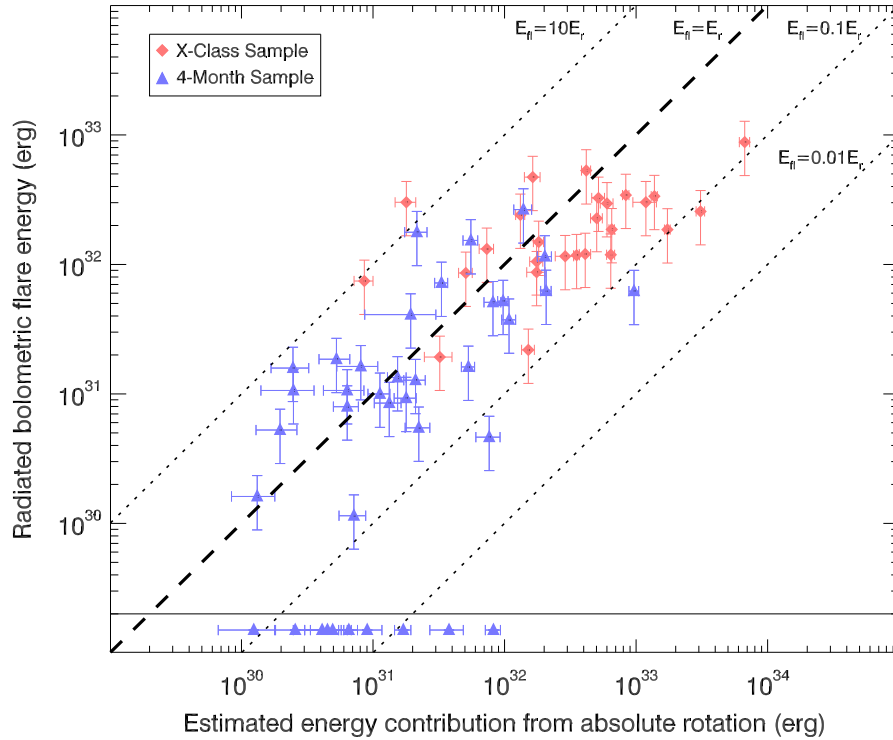
***Figure 6.5:*** *Bolometric flare energy against absolute rotation energy. The dashed line indicates where the bolometric radiated flare energy is equal to the rotation energy. The dotted lines represent where the bolometric flare energy is a 10% and 1% of the rotation energy, as labelled in the plot.*

this plot, although several of the four-month sample regions do populate the higher flare energy and higher rotation energy portion of the plot that is mostly populated by the X-class sample regions. The vast majority of regions populate the 10%+ region of figure 6.3.

The relationship between the radiated bolometric flare energy and energy contribution from the absolute spot rotation, shown in figure 6.5, is arguably the most convincing. This distribution has the least number of active regions to the left of the 1:1 line. There is still a separation between the two samples, which further supports the claim that there is a relationship between sunspot rotation and flaring activity.

The majority of the X-class flare regions lie within the 10-100% $E_{fl}$ range, whereas the four-month sample regions are distributed almost evenly around the 1:1 line.

A fit is not performed for figures 6.3, 6.4 and 6.5 as it is difficult to physically justify. This is because sunspot rotation is one of many possible energy input mechanisms, and the bolometric flaring radiation is one of several energy output mechanisms. The other justification for not performing a fit is that the sunspot rotation (and flaring activity) is only measured while the active region is on the solar disc, which provides an incomplete picture of the energetics of the region. In the majority of cases, the energy output from bolometric flaring radiation is accounted for by the energy input from (absolute) rotation (typically the absolute sunspot rotation injects just less than double the amount of energy output by bolometric flare radiation).

## 6.3  Discussion

It would seem apparent from figures 6.3, 6.4 and 6.5 that there is a clear relationship between the energy injected from sunspot rotation and the radiated bolometric flare energy of an active region.

Combining both of the statistical samples yields a total sample size of 135 sunspots within 64 active regions. Ten of these regions, all from the four-month statistical sample, are presented in the box at the bottom of figures 6.3, 6.4 and 6.5, as they do not produce any flares throughout the analysis period, and as such have a radiated bolometric flare energy of zero.

A key feature of figures 6.3, 6.4 and 6.5 is that the two statistical samples appear to populate different parts of the plot. The X-class flare sample populates the higher bolometric flare energy, higher rotation energy region and the four-month sample populates the lower bolometric flare energy, lower rotation energy region. The mean absolute spot rotation energy for the X-class sample is $5.32 \times 10^{32}$ erg, with a mean

radiated bolometric flare energy of $3.49 \times 10^{32}$ erg. So, on average, the radiated bolometric flare energy accounts for 65.6% of the absolute rotation energy. The four-month sample has a mean absolute rotation energy of $7.59 \times 10^{31}$ erg ($6.06 \times 10^{31}$ erg taking into account the regions that do not flare), and a mean radiated bolometric flare energy of $4.49 \times 10^{31}$ erg ($3.31 \times 10^{31}$ erg). On average, the radiated bolometric flare energy of the four-month sample contributes 59.2% (54.6%) of the absolute rotation energy. The average percentage of absolute rotation accounted for by the bolometric flare energy is comparable between the two samples.

The absolute rotation energy of four-month sample is only 14.3% (11.4%) of the absolute rotation energy of the X-class flare sample. The radiated bolometric flare energy of the four-month sample is 12.9% (9.5%) of the radiated bolometric flare energy of the X-class sample. Once again, these percentages are consistent. These consistencies support the claim that there is an underlying relationship between sunspot rotation and solar flares. With regards to flare energetics, Emslie et al. (2005) report that for large eruptive flares with associated CMEs, approximately half of the energy from the event is emitted as total flare radiation, and half is released in the form of the kinetic energy of the CME. This is likely to vary from event to event, and does not take into account particle acceleration. However, this does leave an excess of energy on average from sunspot rotation, so perhaps this energy from rotation is used for other processes, such as heating the corona.

Figures 6.3, 6.4 and 6.5 all show a convincing positive trend between radiated bolometric flare energy and energy contribution from the net, mid and absolute rotation, respectively. The strongest trend is most certainly between the radiated bolometric flare energy and the estimated energy contribution from the absolute rotation (figure 6.5). The absolute rotation represents a maximum possible rotation, and assumes that rotation in opposite directions does not cancel out. The energy contribution from the absolute rotation is interpreted as the maximum possible

energy contribution from sunspot rotation.

In the vast majority of cases, particularly in regards to the absolute values, the energy generated from sunspot rotation exceeds the radiated bolometric flare energy. This observed excess of energy from sunspot rotation is not problematic, as the radiated bolometric flare energy is only a portion of the energy released by active region-based solar activity. Flares also accelerate particles, and are often associated with coronal mass ejections. Therefore the fact that the most active regions in figure 6.5 have a higher input energy contribution from rotation than output energy from the bolometric flare radiation is somewhat expected.

Through combining the two statistical samples, it is apparent that there is an underlying relationship between sunspot rotation and flaring activity. On average, the energy output from bolometric flare radiation is around 60% of the energy input from sunspot rotation, which leaves some excess energy or eruptive phenomena such as coronal mass ejections. The parameters studied in this thesis comprise a small portion of the overall problem when discussion active region energy budgets. Equation 1.7.6 lists the different possible energy input and output terms, of which this work studies the relationship between just one input process, $E_{rot}$, and one output process, $E_{fl-rad}$.

# Chapter 7

# Summary and Future Work

## 7.1 Summary

The aim of this thesis was to determine the relationship between sunspot rotation and solar flares. Several steps were set out to achieve this goal following the development and improvement of the analysis technique: a case study of a single active region; a statistical study of high flare energy active regions; and an unbiased statistical study of active regions. A summary of the findings of these studies are presented in this chapter.

### 7.1.1 Case Study

Chapter 3 focused on an in-depth analysis of a single active region, AR11158. This region was chosen partly due to its complexity and the presence of five clear sunspots to analyse, and partly due to the fact that literature pertaining to the rotation of sunspots in this region was available from which to draw comparisons.

The case study presented in this thesis is the most complete case study of the rotation of sunspots in AR11158, in terms of the analysis time over which the study was carried out. This offers insight into the long-term rotational properties of the

sunspots within the region, allowing an energy budget to be calculated for AR11158.

The radiated bolometric flare energy of AR11158 is compared to the total absolute and net rotations of the region (the sum of the corresponding rotation values of all sunspots within the region), this is presented in figure 3.12. The absolute rotation traces the bolometric flare energy particularly well. The net rotation is more interesting, with a change in net rotation direction occurring roughly 20 hours after the X-class flare. The absolute rotation at the end of the analysis period for AR11158 was 563° ± 24°, and the net rotation was only 12° ± 24°.

The energy output from the absolute sunspot rotation is higher than the energy output by bolometric flare radiation for the duration of the analysis. By the end of the analysis period, the absolute rotation contributes three times more energy to the corona than is released by the bolometric solar flare radiation.

## 7.1.2 X-Class Flare Sample

The X-class flare sample is the first statistical sample solely devoted to understanding the role sunspot rotation plays in generating the energy released by solar flares. The sample consists of every active region from the launch of SDO in February 2010 to the present day (as of 9 March 2017) that has given rise to an X-class solar flare. The sample contains 76 sunspots within 26 active regions, which gave rise to a total of 42 X-class solar flares.

It was determined in this chapter that for a meaningful comparison between sunspot rotation and solar flares to be drawn, the sunspot rotation must be converted into an estimate of energy contribution from an injection of helicity. As the helicity is proportional to the sunspot rotation multiplied by the flux squared, the amount of magnetic flux (determined by the size of the sunspot) rotating plays an important role in determining the quantity of energy injected from the rotation.

Nineteen out of the 26 active regions analysed received enough energy from absolute sunspot rotation to account for the bolometric flaring radiation. On average, the output bolometric flare energy accounted for approximately two thirds (65.5%) of the energy input by the absolute sunspot rotation. This is somewhat consistent with work undertaken by Emslie et al. (2005), who report that half of the energy released during an eruptive event is released as radiation, while the rest is used for other processes (to provide the kinetic energy for a CME, for example). It became apparent that this high flare-energy study must be accompanied by an unbiased sample, to determine whether the relationship observed was consistent with a more typical sample of active regions.

### 7.1.3 Four-Month Statistical Sample

The four-month statistical sample consists of all sunspot that meet the selection criteria between 1 May 2013 and 31 August 2013. The sample contains 59 sunspots within 38 active regions. This sample was subjected to the same analysis as the X-class flare sample, to determine the relationship between sunspot rotation energy and radiated bolometric flare energy.

As in the X-class sample, the average bolometric flare energy output was close to two-thirds (59.2%) of the energy input from the absolute sunspot rotation. The absolute rotation energy of the four-month sample was, on average, only 14.3% of that of the X-class flare sample, and the average bolometric flare energy of the four-month sample was only 12.9% of the bolometric flare energy of the X-class flare sample. This indicates that there is in fact a relationship between the amount of energy injected through sunspot rotation and the amount of energy radiated by solar flares. This claim is supported by figure 6.5, which shows the energy due to flare radiation versus the energy contributed from $R_{abs}$. This figure indicates an upwards trend between radiated bolometric flare energy an energy contributed

from $R_{abs}$, and shows a separation between the high flare-energy (X-class sample) and low flare-energy (four-month sample) samples. A Kolmogorov-Smirnov test was performed on the cumulative distributions between the two samples, and found that the maximum difference (of the cumulative volume) between the two samples was only 25%. The samples followed similar cumulative distributions, which further confirms that there is some underlying physics that does not discriminate between high and low flare energy active regions.

## 7.2  Future Work

This work has determined the relationship between sunspot rotation and radiated bolometric flare energy. Referring back to the energy balance equation (equation 1.7.6), radiated bolometric flare energy is only a piece of the puzzle. An in-depth analysis into other possible energy release mechanisms is required, such as coronal mass ejections/filament eruptions, particle acceleration, and the role sunspot rotation may play in coronal heating. The next step in understanding the different energy outputs processes at play would be to include these other energy release mechanisms in the statistical samples carried out in this thesis. The HEK would be used to search for CMEs and filament eruptions and associate them with active regions in the samples. Case studies would be undertaken to determine how to convert these events into an output energy. Once the CME/filament eruption analysis tool is developed, the statistical samples would be updated with an energy input from these mechanisms. A statistical study into active regions that have no flaring activity would have particular value when investigating the effect of sunspot rotation on solar flare productivity. If these regions show significant sunspot rotation, but no flaring activity, then further investigation into energy outputs would be required to understand how the input energy is balanced.

There are several regions in which the energy from sunspot rotation is not enough

to account for the observed radiated bolometric flare energy. Other energy input processes such as shearing motions and flux emergence must be studied in detail to understand how photospheric motions can inject energy into the corona, as well as which are the common and dominant mechanisms. Case studies of these regions, with an emphasis on the different energy input mechanisms, would be required to determine the energy budget and dominant source of energy injection. A starting point for this would be to analyse any outlying regions in the samples presented and investigate them to determine what other mechanisms provide the input energy required to account for the output energy. Analysis tools would be developed to estimate energy injection values from different mechanisms such as emergence and shear through case studies of these outlying regions, and these tools would then be applied to the samples as a whole.

Essentially it boils down to the need to determine the energy injection and output for each term in equation 1.7.6, most likely through statistical studies such as those presented in this thesis, in order to calculate a detailed energy budget, and to understand how energy is transferred through the photosphere and into the corona.

The energy injected from sunspot rotation estimation used in this thesis is drawn from an empirical relationship, and as such it only provides an energy estimate for each active region. A more critical evaluation of the energy estimation from sunspot rotation using numerical simulations is needed to evaluate the quality of this estimate, and would also aid in understanding how the twist from the photosphere is injected into the coronal magnetic field. As a starting point, non-linear force free simulations with different sunspot connectivities and rotations to represent the rotation parameters ($R_{net}$, $R_{mid}$ and $R_{abs}$) defined in this work could be used to determine the energy input in each case. An estimation similar to that used to calculate the active region energy input would be calculated to evaluate the reliability of the current method.

CHAPTER 7

Although the statistical analyses carried out in this thesis provide a large data-set in terms of rotation values of active regions, they are lacking the depth of analysis that would be achieved through case studies. Selected case studies of the regions covered in this work would give a better breakdown of the energy budget for each region, and may shed some light as to what the dominant energy injection mechanism is in each region. There are three cases (AR11302, AR11402 and AR11515) where the leading 'parent' sunspot splits into two smaller 'child' sunspots following a period of significant anti-clockwise rotation. In each case, the 'child' sunspots are then observed to rotate significantly in the same anti-clockwise direction. A multi-wavelength analysis of these regions would illustrate the mechanisms at play, for example perhaps the 'parent' sunspot emerged as two braided flux tubes, where the observed rotation is the unbraiding of these flux tubes, leading to the splitting. Studies into the temporal and spatial association of high-energy solar flares would aid in our understanding of how connecting sunspots affect one another when it comes to sunspot rotation.

A long-term aim is to fully automate the analysis tool. This would involve automatically locating the active regions and carrying out the analysis of their sunspots. This would allow a very large sample of sunspot rotations to be built up, which in turn would grow the current sample size to incorporate every sunspot that meets the selection criteria since the launch of SDO. This would place greater constraints on the relationship between sunspot rotation and solar flares and provide stronger statistical significance. This would also increase the number of outliers in the sample, making it easier to select and study regions in which other energy input and output mechanisms dominate.

## 7.3 Closing Remarks

This thesis has studied the relationship between the energy injected through sunspot rotation and the energy released from solar flare radiation using two statistical samples comprising 64 active regions and 135 sunspots. It has been found that there is convincing evidence that sunspot rotation provides a significant portion of energy towards solar flare radiation, and in many cases provides an excess of energy (the output bolometric flare energy accounts for 65.6% and 59.2% of the input rotation energy on average in the X-class flare and four-month samples, respectively), which may be used for other solar eruptive behaviour. That is not to say that sunspot rotation is the only form of energy injection into the corona, but in most cases it may be the dominant mechanism.

To put this into context within the field of solar physics as a whole, this thesis has determined that sunspot rotation can inject a significant amount of helicity, and so energy, into the solar atmosphere which can be used to power solar activity.

# Bibliography

Abetti, G. & Colacevich, A. 1932, Osservazioni e memorie dell'Osservatorio astrofisico di Arcetri, 50

Babcock, H. W. 1961, *Astrophys. J.*, 133, 572

Barlow, R. J. 1989, in Statistics: A Guide to the Use of Statistical Methods in the Physical Sciences, ed. D. J. Sandiford, 1–200

Barnes, C. W. & Sturrock, P. A. 1972, *Astrophys. J.*, 174, 659

Berger, M. A. 1984, Geophysical and Astrophysical Fluid Dynamics, 30, 79

Botha, G. J. J., Busse, F. H., Hurlburt, N. E., & Rucklidge, A. M. 2008, *Mon. Not. Roy. Astron. Soc.*, 387, 1445

Brown, D. S., Nightingale, R. W., Alexander, D., et al. 2003, *Solar Phys.*, 216, 79

Burnell, J. B., Green, S. F., Jones, B. W., et al. 2003, An Introduction to the Sun and Stars

Carrington, R. C. 1859, *Mon. Not. Roy. Astron. Soc.*, 19, 81

Cox, D. P. & Tucker, W. H. 1969, *Astrophys. J.*, 157, 1157

Dere, K. P., Landi, E., Mason, H. E., Monsignori Fossi, B. C., & Young, P. R. 1997, *Astron. Astrophys. Suppl.*, 125, 149

Dere, K. P., Landi, E., Young, P. R., et al. 2009, *Astron. Astrophys.*, 498, 915

Deubner, F.-L. 1975, *Astron. Astrophys.*, 44, 371

Donnelly, R. F., Grubb, R. N., & Cowley, F. C. 1977, NASA STI/Recon Technical Report N, 78, 13992

Dwivedi, B. N. 2003, in Dynamic Sun, ed. B. N. Dwivedi, 106–112

Emslie, A. G., Dennis, B. R., Holman, G. D., & Hudson, H. S. 2005, Journal of Geophysical Research (Space Physics), 110, A11103

Emslie, A. G., Dennis, B. R., Shih, A. Y., et al. 2012, *Astrophys. J.*, 759, 71

Evershed, J. 1910, *Mon. Not. Roy. Astron. Soc.*, 70, 217

Fan, Y. 2009, *Astrophys. J.*, 697, 1529

Foukal, P. 2013, in Solar Astrophysics, ed. P. Foukal, 1–29

Georgoulis, M. K. & LaBonte, B. J. 2006, *Astrophys. J.*, 636, 475

Gibson, S. E., Fan, Y., Mandrini, C., Fisher, G., & Demoulin, P. 2004, *Astrophys. J.*, 617, 600

Golub, L. & Pasachoff, J. M. 2013, in The Solar Corona, ed. L. Golub, 282–286

Gopasyuk, O. S. & Kosovichev, A. G. 2011, *Astrophys. J.*, 729, 95

Gopasyuk, S. I. & Gopasyuk, O. S. 2005, *Solar Phys.*, 231, 11

Gordovskyy, M., Browning, P. K., Kontar, E. P., & Bian, N. H. 2014, *Astron. Astrophys.*, 561, A72

Hale, G. E. & Nicholson, S. B. 1938, Magnetic observations of sunspots, 1917-1924

Hathaway, D. H. 2010, Living Reviews in Solar Physics, 7, 1

Heyvaerts, J. & Priest, E. R. 1984, *Astron. Astrophys.*, 137, 63

Hood, A. W., Archontis, V., & MacTaggart, D. 2012, *Solar Phys.*, 278, 3

Hood, A. W. & Priest, E. R. 1979, *Solar Phys.*, 64, 303

Hood, A. W. & Priest, E. R. 1981, Geophysical and Astrophysical Fluid Dynamics, 17, 297

Hughes, D. W., Rosner, R., & Weiss, N. O. 2007, The Solar Tachocline

Hurlburt, N., Cheung, M., Schrijver, C., et al. 2012, *Solar Phys.*, 275, 67

Jain, K., Komm, R. W., González Hernández, I., Tripathy, S. C., & Hill, F. 2012, *Solar Phys.*, 279, 349

Jain, K., Tripathy, S. C., & Hill, F. 2015, *Astrophys. J.*, 808, 60

Jiang, Y., Zheng, R., Yang, J., et al. 2012, *Astrophys. J.*, 744, 50

Kazachenko, M. D., Canfield, R. C., Longcope, D. W., et al. 2009, *Astrophys. J.*, 704, 1146

Komm, R., González Hernández, I., Howe, R., & Hill, F. 2015a, *Solar Phys.*, 290, 3113

Komm, R., Tripathy, S., Howe, R., & Hill, F. 2015b, in AAS/AGU Triennial Earth-Sun Summit, Vol. 1, AAS/AGU Triennial Earth-Sun Summit, 105.06

Koza, J., Sütterlin, P., Kučera, A., & Rybák, J. 2007, in Astronomical Society of the Pacific Conference Series, Vol. 368, The Physics of Chromospheric Plasmas, ed. P. Heinzel, I. Dorotovič, & R. J. Rutten, Heinzel

Kumar, P., Park, S.-H., Cho, K.-S., & Bong, S.-C. 2013, *Solar Phys.*, 282, 503

Lam, H.-L., Boteler, D. H., & Trichtchenko, L. 2002, Annales Geophysicae, 20, 1073

Leighton, R. B., Noyes, R. W., & Simon, G. W. 1962, *Astrophys. J.*, 135, 474

Lemen, J. R., Title, A. M., Akin, D. J., et al. 2012, *Solar Phys.*, 275, 17

Li, A. & Liu, Y. 2015, *Solar Phys.*, 290, 2199

Li, J., Mickey, D. L., & LaBonte, B. J. 2005, *Astrophys. J.*, 620, 1092

Li, L. & Zhang, J. 2009, *Astrophys. J. Letters*, 706, L17

Li, W., Ai, C., & Wang, H. 2001, in IAU Symposium, Vol. 203, Recent Insights into the Physics of the Sun and Heliosphere: Highlights from SOHO and Other Space Missions, ed. P. Brekke, B. Fleck, & J. B. Gurman, 291

Liu, C., Xu, Y., Cao, W., et al. 2016, Nature Communications, 7, 13104

Louis, R. E., Ravindra, B., Mathew, S. K., et al. 2012, *Astrophys. J.*, 755, 16

Maltby, P. 1964, Astrophysica Norvegica, 8, 205

Mazzotta, P., Mazzitelli, G., Colafrancesco, S., & Vittorio, N. 1998, *Astron. Astrophys. Suppl.*, 133, 403

Min, S. & Chae, J. 2009, *Solar Phys.*, 258, 203

Moses, D., Clette, F., Delaboudinière, J.-P., et al. 1997, *Solar Phys.*, 175, 571

Nightingale, R. W., Brown, D. S., Metcalf, T. R., et al. 2002, in Multi-Wavelength Observations of Coronal Structure and Dynamics, ed. P. C. H. Martens & D. Cauffman, 149

Nightingale, R. W., Shine, R. A., Brown, D. S., et al. 2001, AGU Spring Meeting Abstracts

Parker, E. N. 1972, *Astrophys. J.*, 174, 499

Pesnell, W. D., Thompson, B. J., & Chamberlin, P. C. 2012, *Solar Phys.*, 275, 3

Priest, E. R. 2014, in Magnetohydrodynamics of the Sun, ed. E. R. Priest, 1–65

Ravindra, B., Yoshimura, K., & Dasso, S. 2011, *Astrophys. J.*, 743, 33

Régnier, S. & Canfield, R. C. 2006, *Astron. Astrophys.*, 451, 319

Ruan, G., Chen, Y., Wang, S., et al. 2014, *Astrophys. J.*, 784, 165

Schou, J., Scherrer, P. H., Bush, R. I., et al. 2012, *Solar Phys.*, 275, 229

Schuck, P. W. 2006, *Astrophys. J.*, 646, 1358

Schuck, P. W. 2008, *Astrophys. J.*, 683, 1134

Schwabe, M. 1844, Astronomische Nachrichten, 21, 233

Selwa, M., Poedts, S., & DeVore, C. R. 2013, *Solar Phys.*, 284, 515

Srivastava, A. K., Zaqarashvili, T. V., Kumar, P., & Khodachenko, M. L. 2010, *Astrophys. J.*, 715, 292

St. John, C. E. 1913, *Astrophys. J.*, 37, 322

Stenflo, J. O. 1969, *Solar Phys.*, 8, 115

Stix, M. 2002, in The Sun - An Introduction, ed. M. Stix, 1–490

Sturrock, Z. & Hood, A. W. 2016, *Astron. Astrophys.*, 593, A63

Sturrock, Z., Hood, A. W., Archontis, V., & McNeill, C. M. 2015, *Astron. Astrophys.*, 582, A76

Su, J. T., Shen, Y. D., Liu, Y., Liu, Y., & Mao, X. J. 2012, *Astrophys. J.*, 755, 113

Thomas, J. H. & Weiss, N. O. 2008, Sunspots and Starspots

Tian, L. & Alexander, D. 2008, *Astrophys. J.*, 673, 532

Tian, L., Alexander, D., & Nightingale, R. 2008, *Astrophys. J.*, 684, 747

Tobias, S. M., Weiss, N. O., & Kirk, V. 1995, *Mon. Not. Roy. Astron. Soc.*, 273, 1150

Török, T., Temmer, M., Valori, G., et al. 2013, *Solar Phys.*, 286, 453

Tziotziou, K., Georgoulis, M. K., & Raouafi, N.-E. 2012, *Astrophys. J. Letters*, 759, L4

Ulrich, R. K. 1970, *Astrophys. J.*, 162, 993

Vemareddy, P., Ambastha, A., & Maurya, R. A. 2012, *Astrophys. J.*, 761, 60

Vemareddy, P., Cheng, X., & Ravindra, B. 2016, *Astrophys. J.*, 829, 24

Wang, R., Liu, Y. D., Wiegelmann, T., et al. 2016, *Solar Phys.*, 291, 1159

Wang, S., Liu, C., Deng, N., & Wang, H. 2014, *Astrophys. J. Letters*, 782, L31

White, S. M., Thomas, R. J., & Schwartz, R. A. 2005, *Solar Phys.*, 227, 231

Yan, X. L. & Qu, Z. Q. 2007, *Astron. Astrophys.*, 468, 1083

Yan, X. L., Qu, Z. Q., & Kong, D. F. 2008a, *Mon. Not. Roy. Astron. Soc.*, 391, 1887

Yan, X. L., Qu, Z. Q., Kong, D. F., & Xu, C. L. 2012, *Astrophys. J.*, 754, 16

Yan, X. L., Qu, Z. Q., & Xu, C. L. 2008b, *Astrophys. J. Letters*, 682, L65

Yan, X.-L., Qu, Z.-Q., Xu, C.-L., Xue, Z.-K., & Kong, D.-F. 2009, Research in Astronomy and Astrophysics, 9, 596

Yan, X. L., Xue, Z. K., Pan, G. M., et al. 2015, *Astrophys. J. Supple.*, 219, 17

Zeeman, D. P. 1897, Philosophical Magazine Series 5, 44, 55

Zhang, J., Li, L., & Song, Q. 2007, *Astrophys. J. Letters*, 662, L35

Zhang, Y., Liu, J., & Zhang, H. 2008, *Solar Phys.*, 247, 39

Zhu, C., Alexander, D., & Tian, L. 2012, *Solar Phys.*, 278, 121

# Appendix

# X-Class Sample Profiles
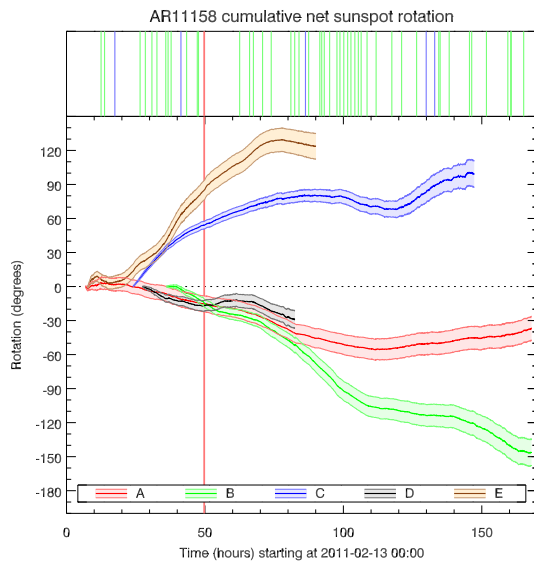
**(i)** *AR11158*
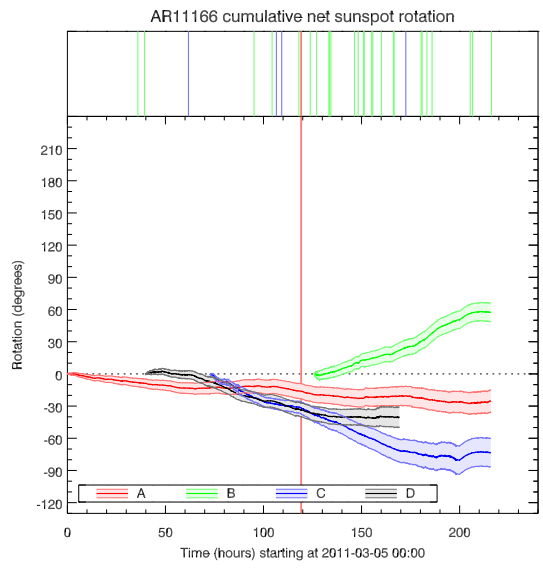
**(ii)** *AR11166*
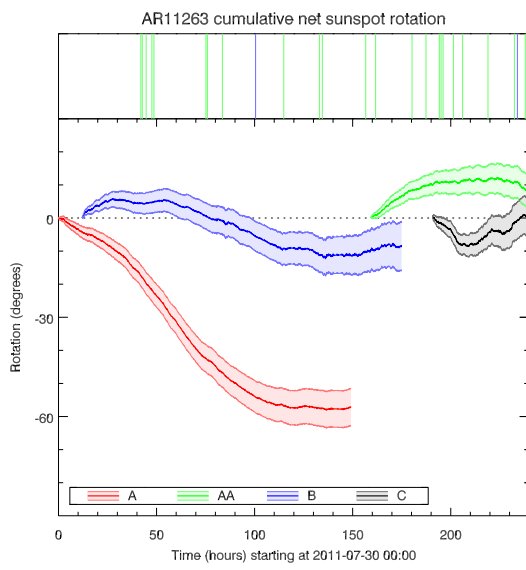
**(iii)** *AR11263*
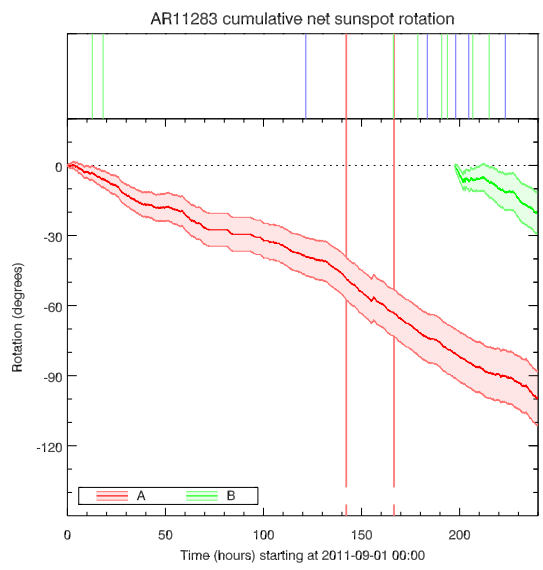
**(iv)** *AR11283*
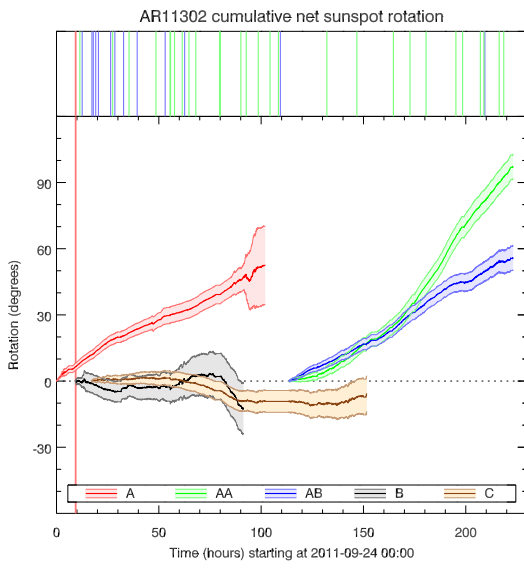
**(v)** *AR11302*
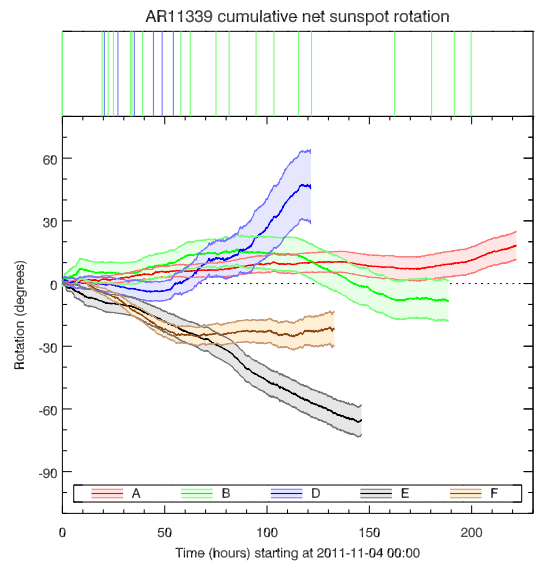


**(vi)** *AR11339*
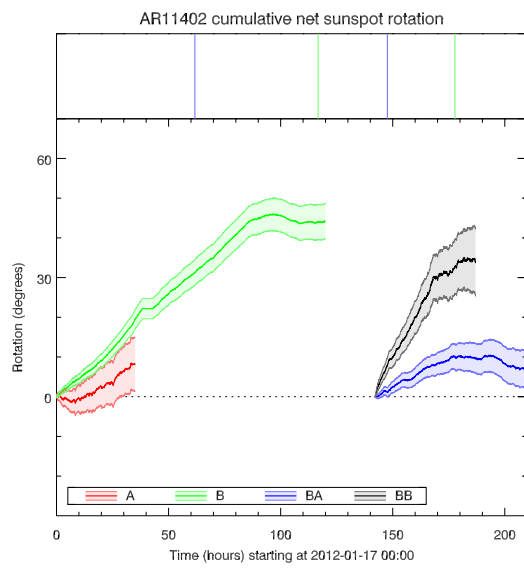


**(vii)** *AR11402*
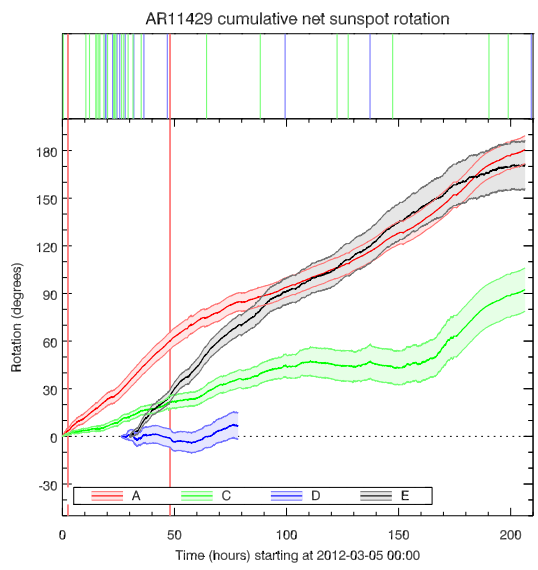


**(viii)** *AR11429*
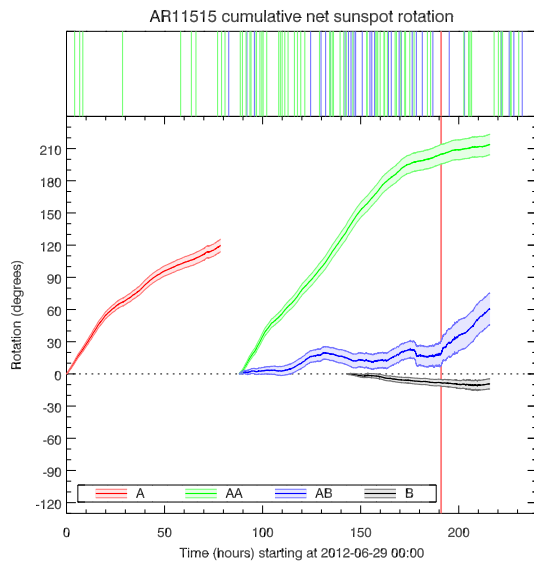
**(ix)** *AR11515*
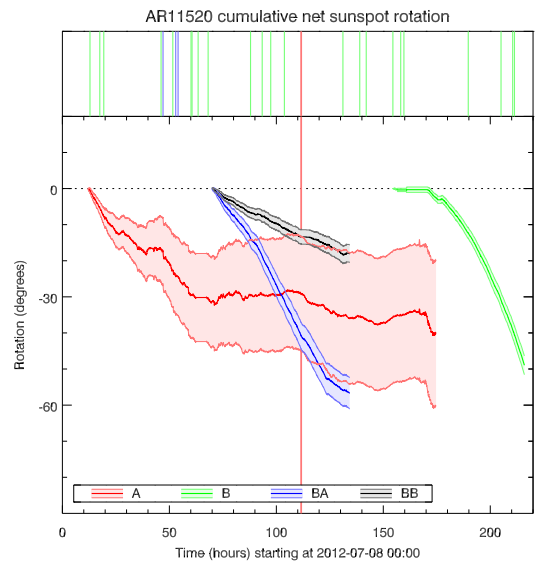
**(x)** *AR11520*
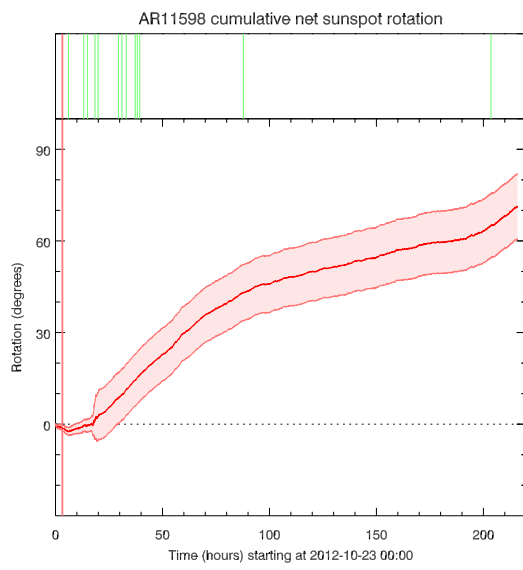


**(xi)** *AR11598*
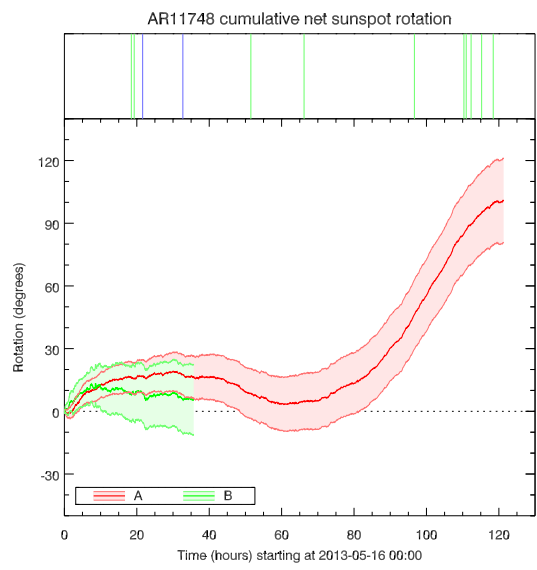
**(xii)** *AR11748*
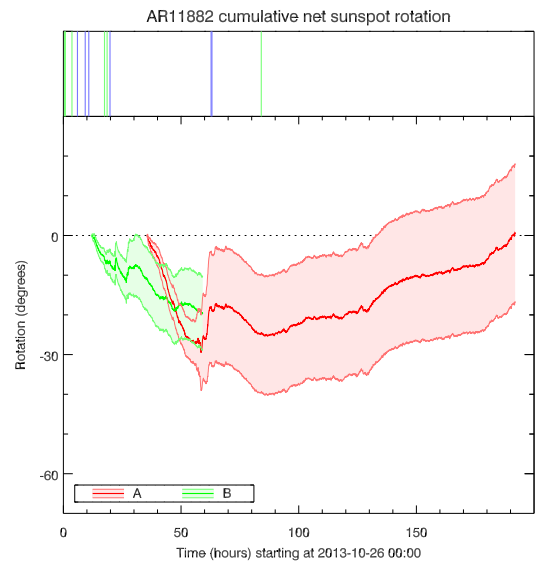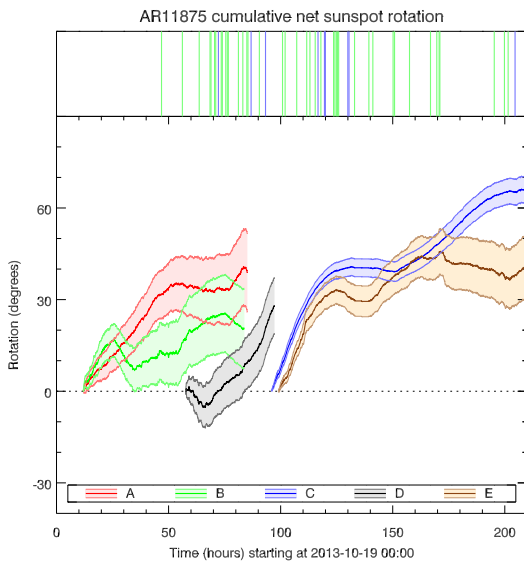
**(xiii)** *AR11875*

**(xiv)** *AR11882*
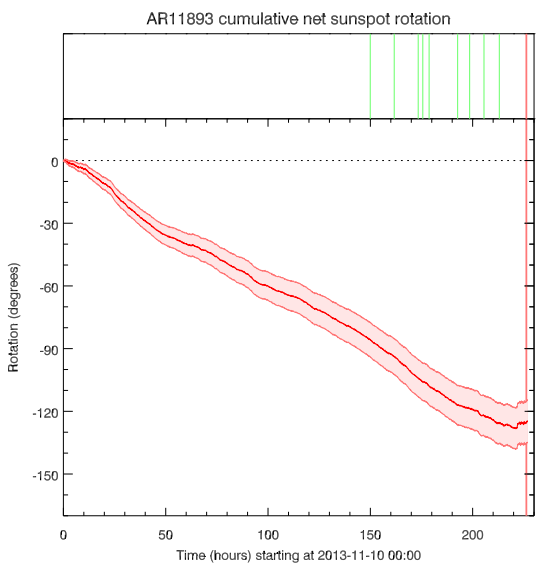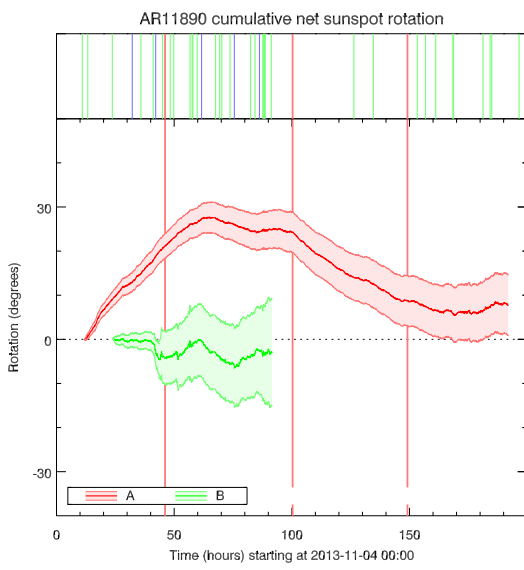


**(xv)** *AR11890*

**(xvi)** *AR11893*
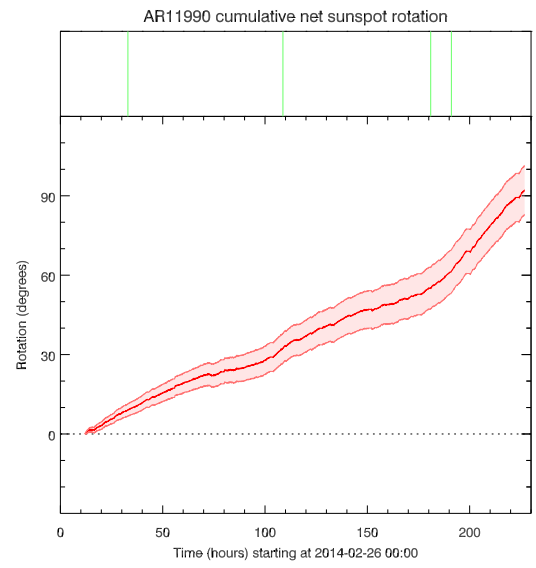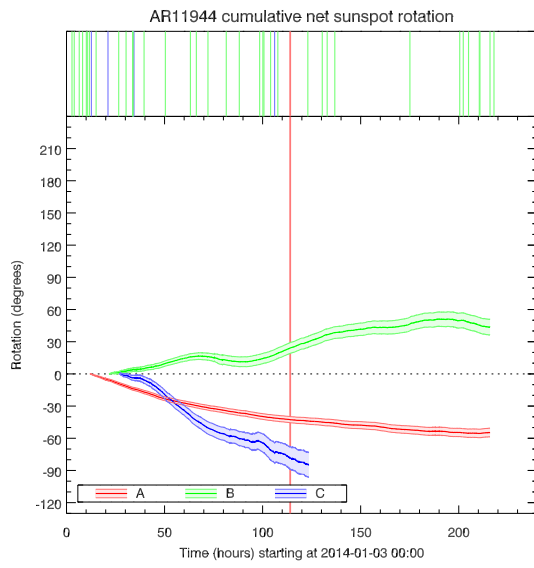
**(xvii)** *AR11944*



**(xviii)** *AR11990*
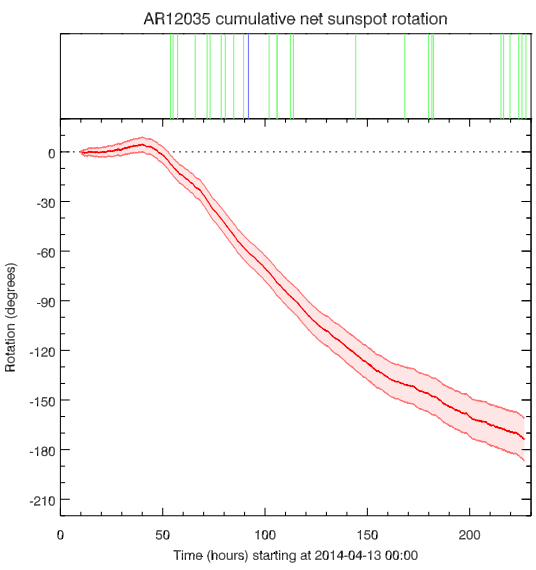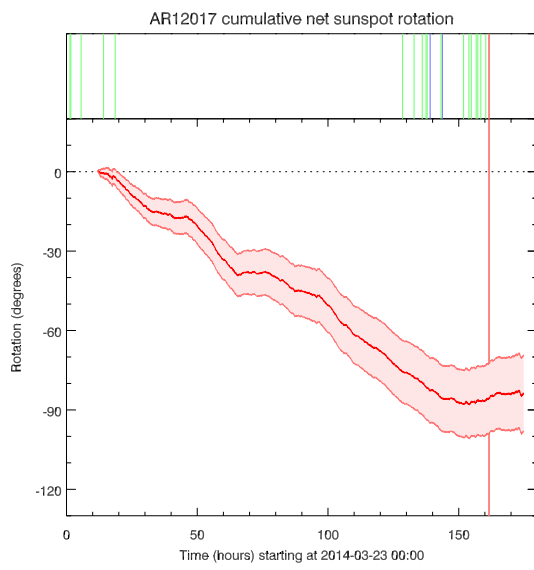


**(xix)** *AR12017*



**(xx)** *AR12035*
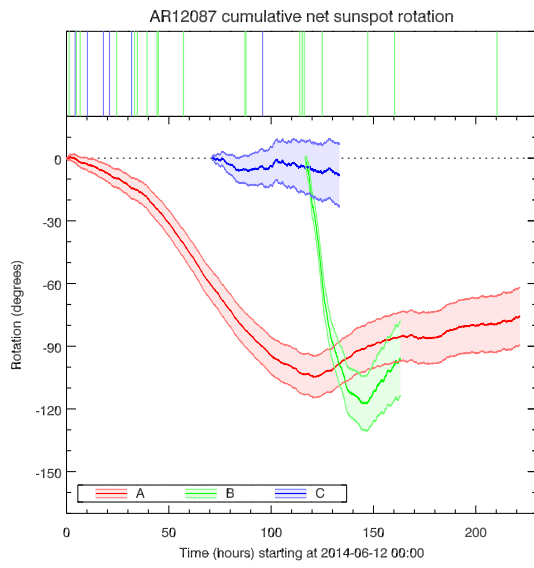
**(xxi)** *AR12087*
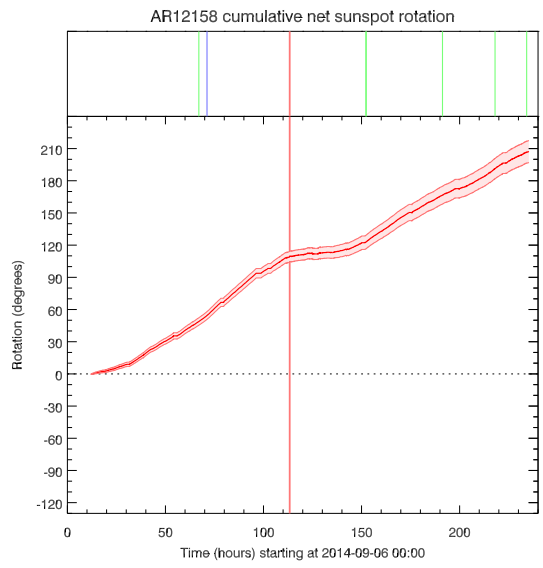
**(xxii)** *AR12158*
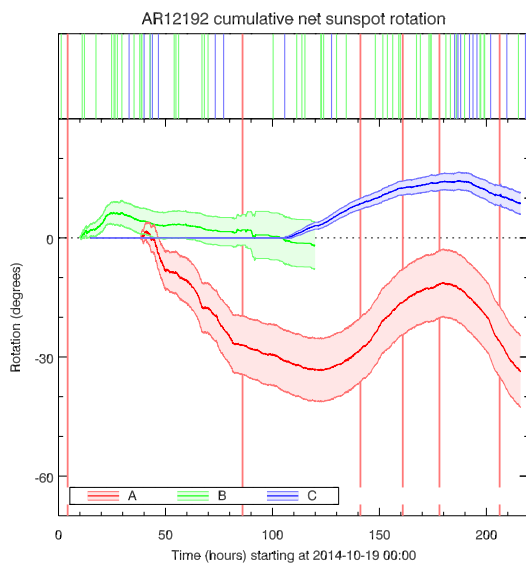


**(xxiii)** *AR12192*
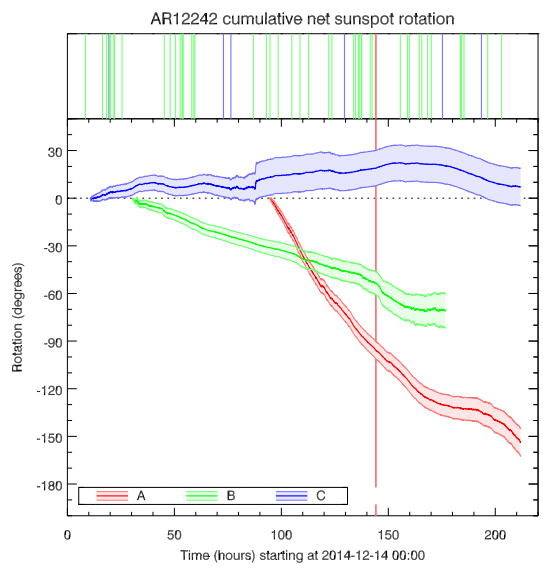
**(xxiv)** *AR12242*
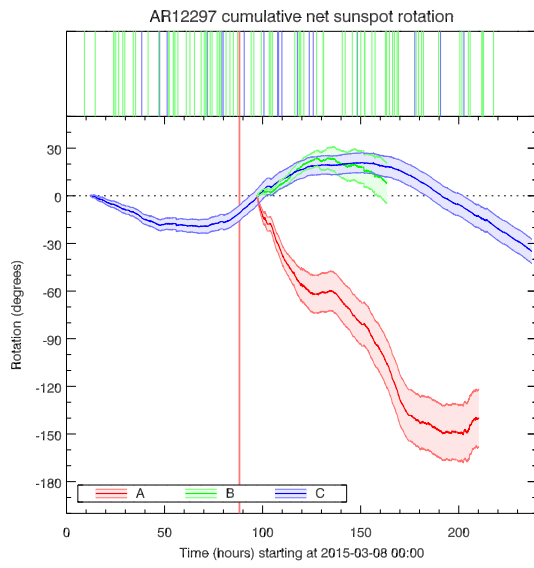
**(xxv)** *AR12297*
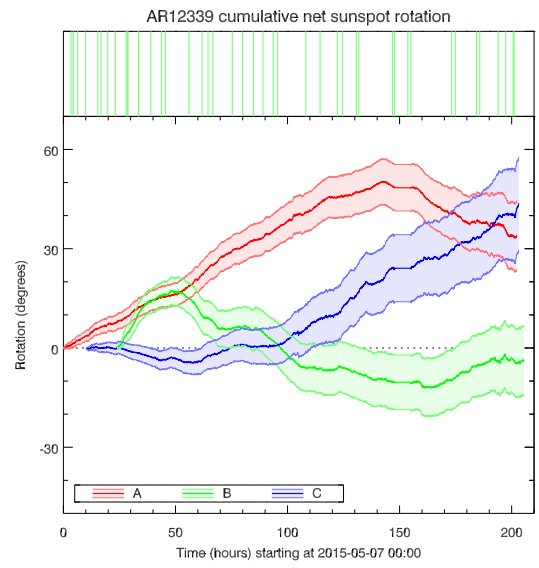


**(xxvi)** *AR12339*

# Four-Month Sample Profiles
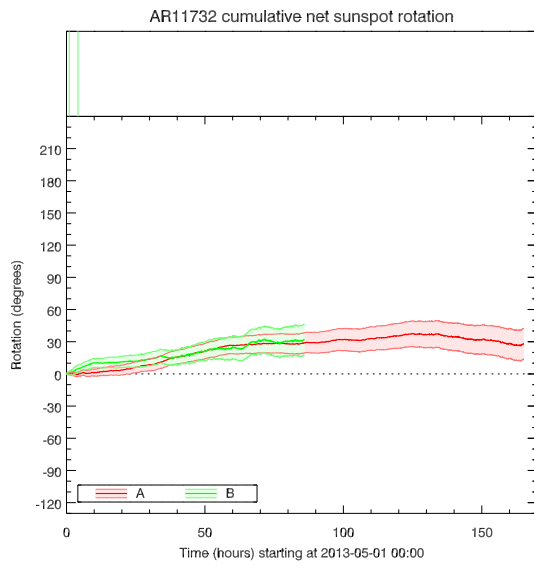
**(i)** *AR11732*
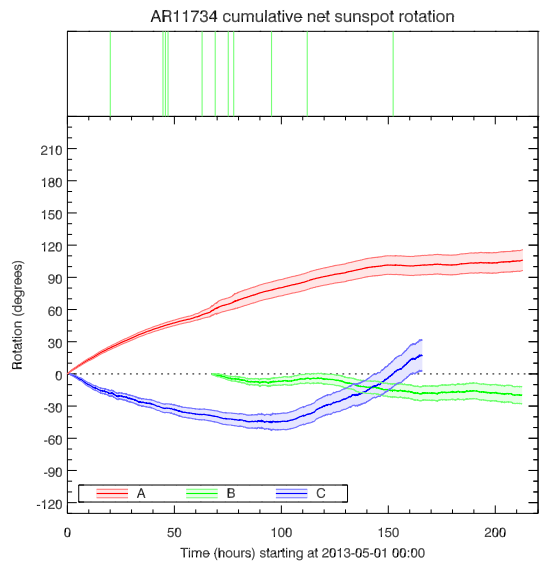
**(ii)** *AR11734*
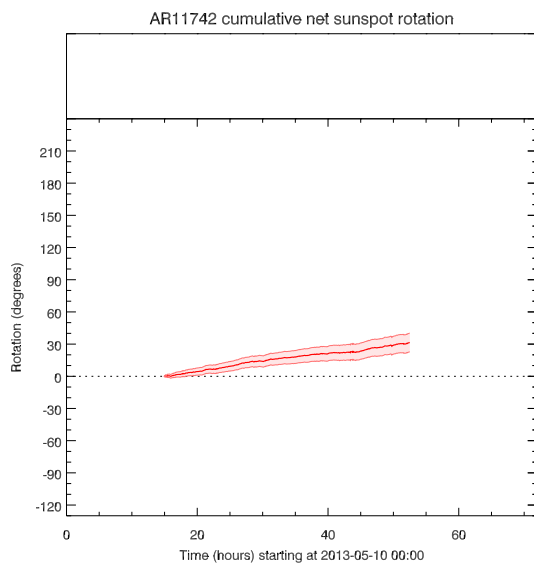
**(iii)** *AR11742*
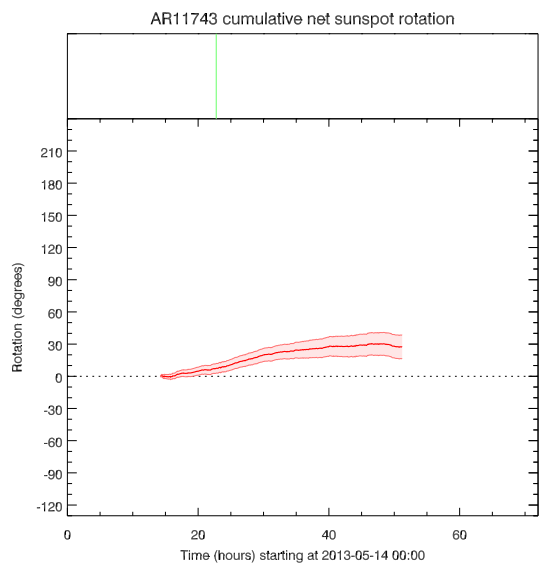
**(iv)** *AR11743*
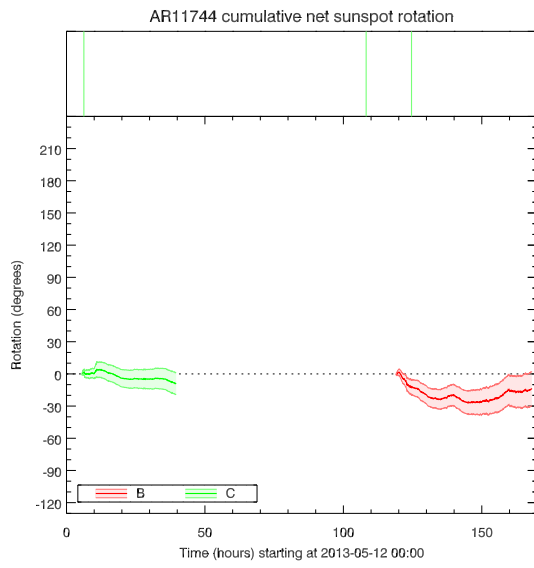
**(v)** *AR11744*
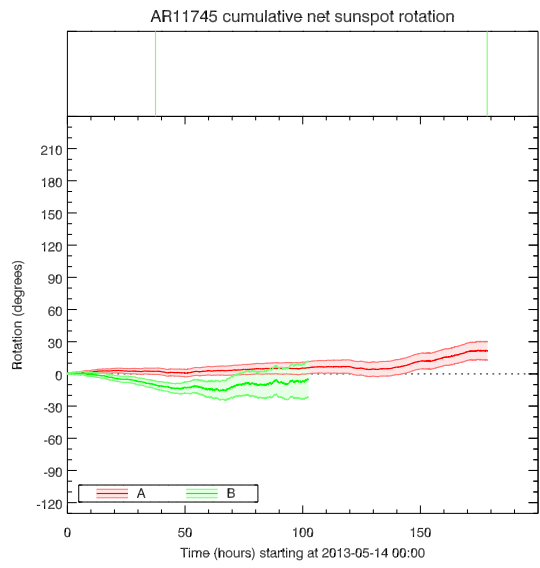


**(vi)** *AR11745*
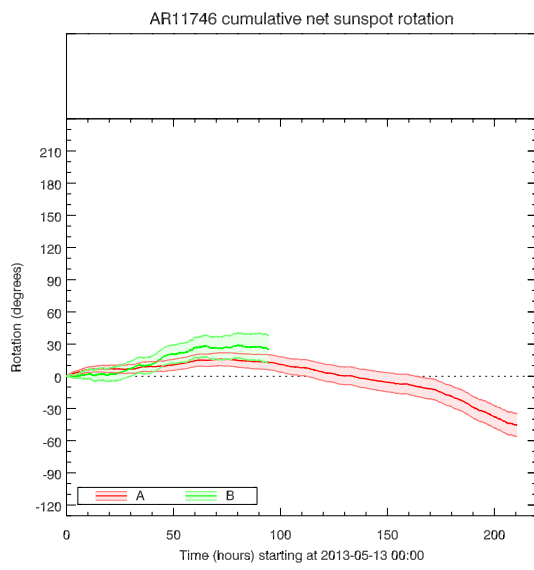


**(vii)** *AR11746*



**(viii)** *AR11747*

168
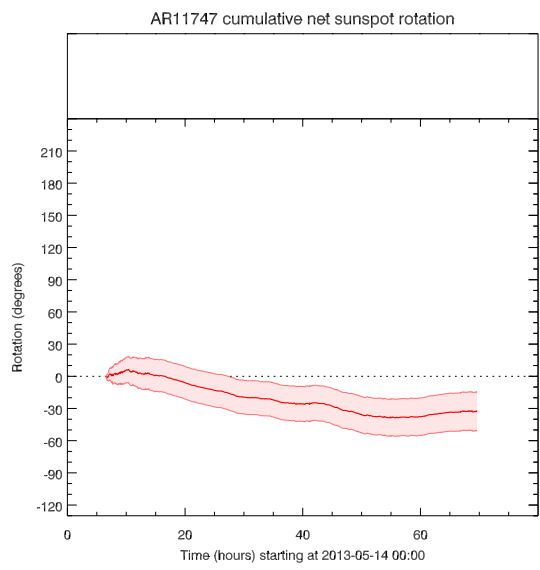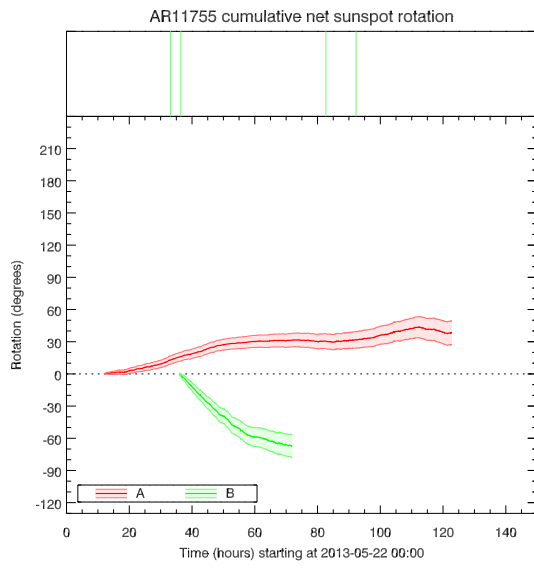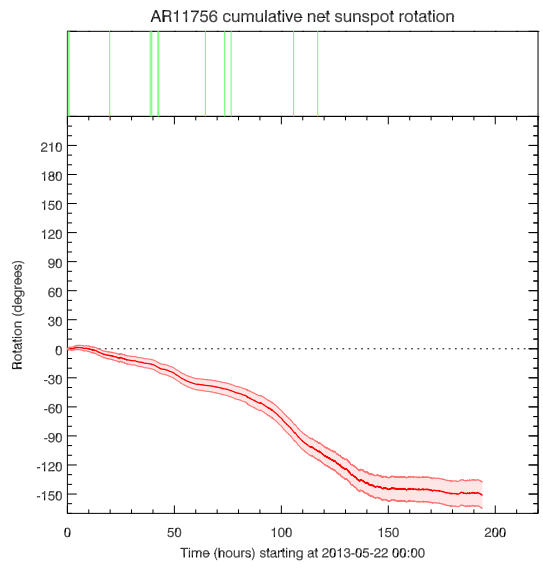
**(ix)** *AR11755*



**(x)** *AR11756*
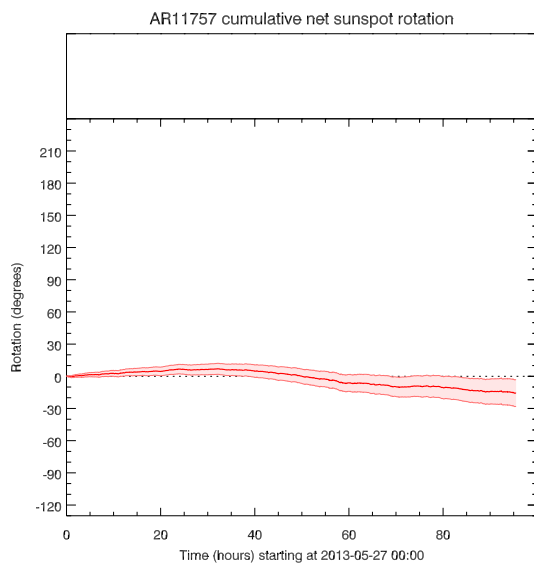


**(xi)** *AR11757*
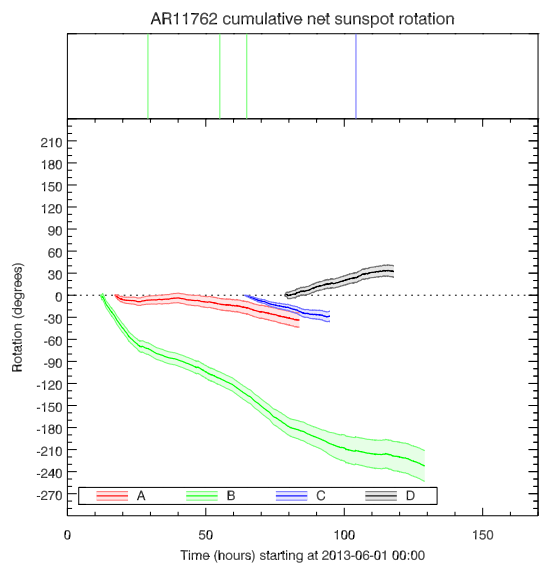


**(xii)** *AR11762*
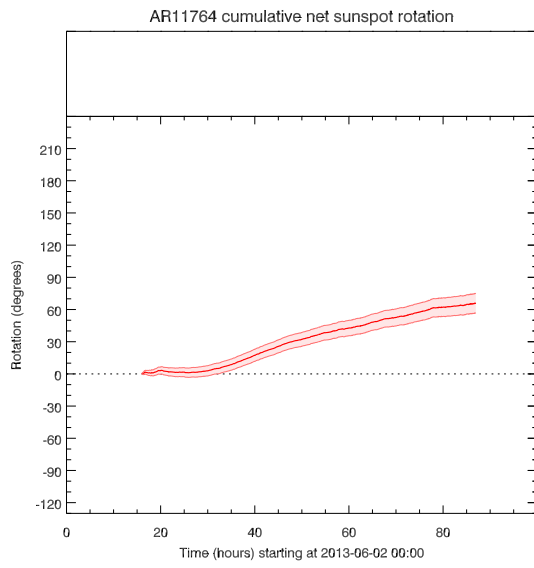
**(xiii)** *AR11764*
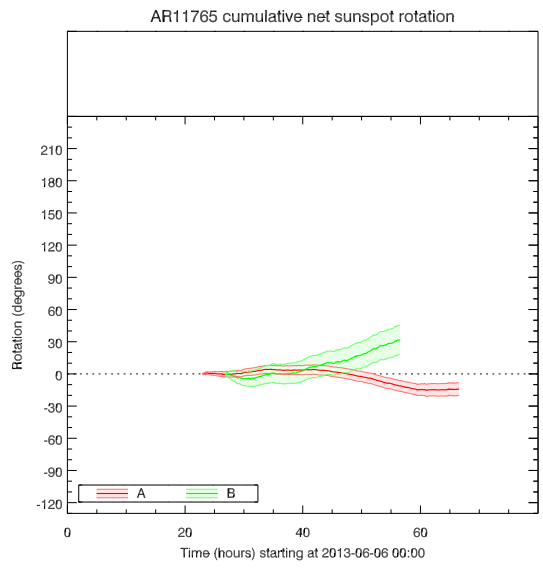


**(xiv)** *AR11765*
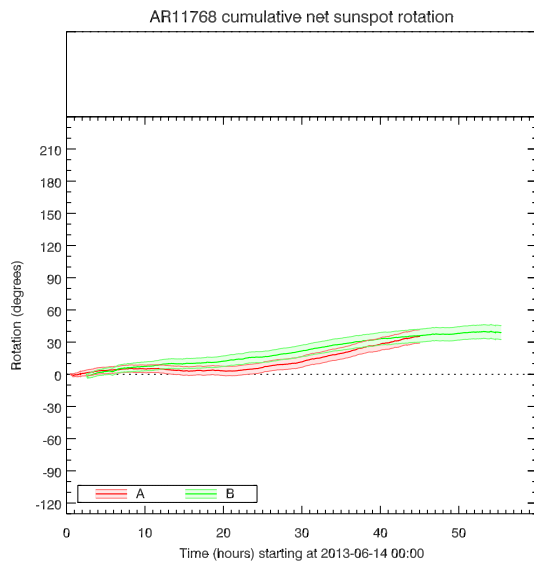


**(xv)** *AR11768*
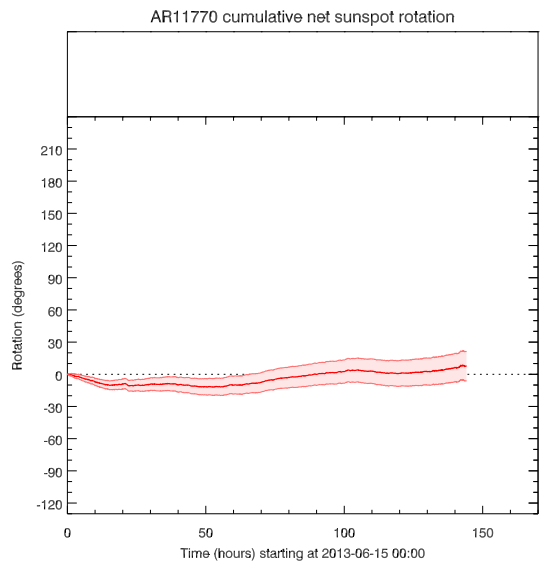


**(xvi)** *AR11770*
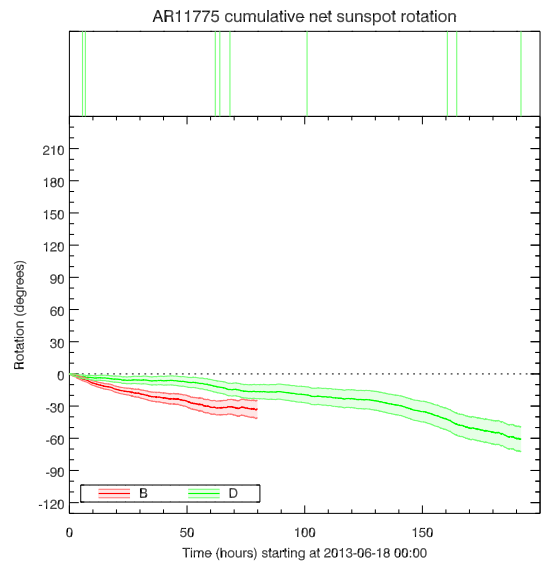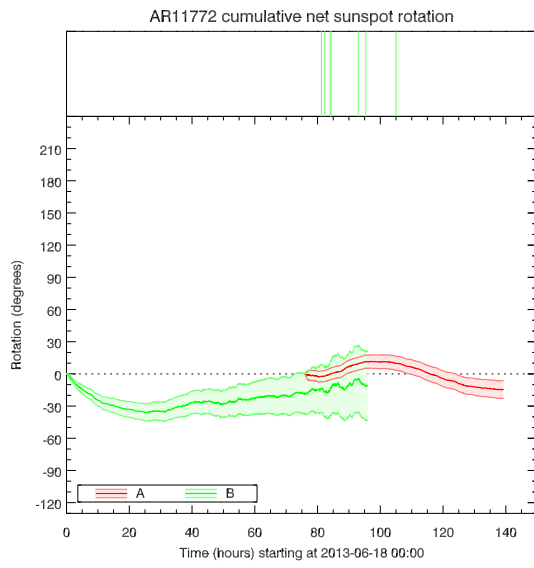
**(xvii)** *AR11772*



**(xviii)** *AR11775*
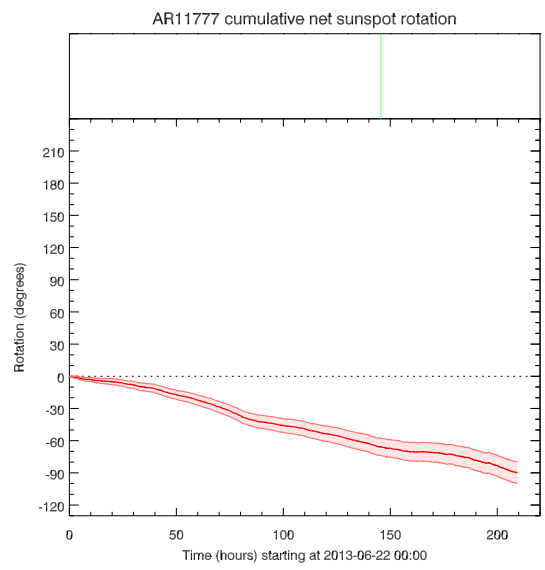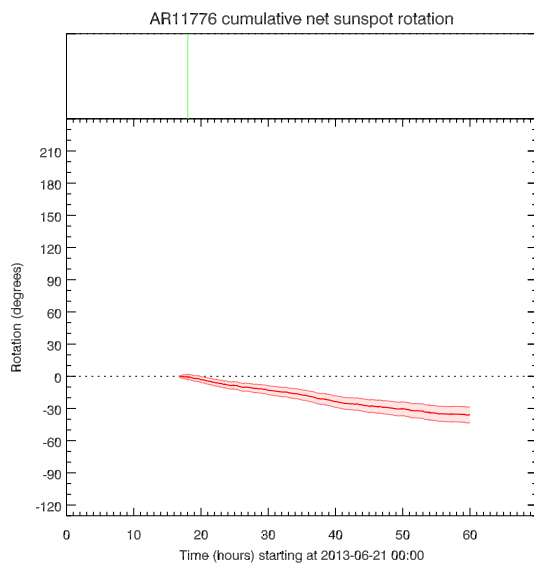


**(xix)** *AR11776*



**(xx)** *AR11777*
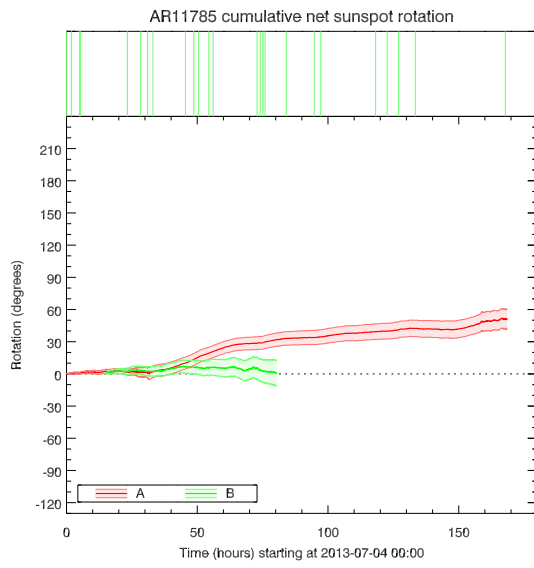
**(xxi)** *AR11785*
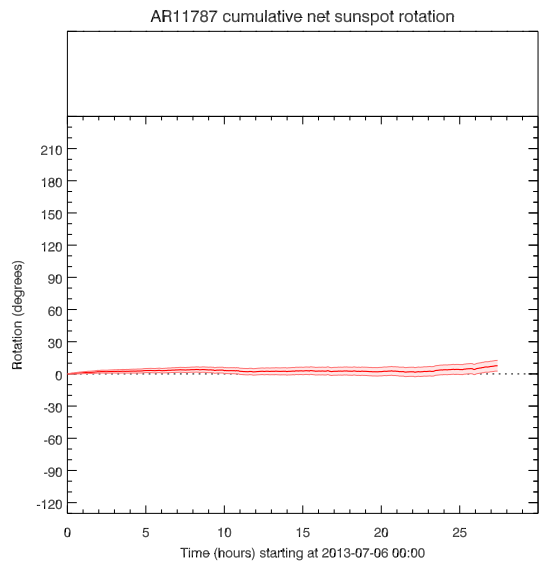


**(xxii)** *AR11787*
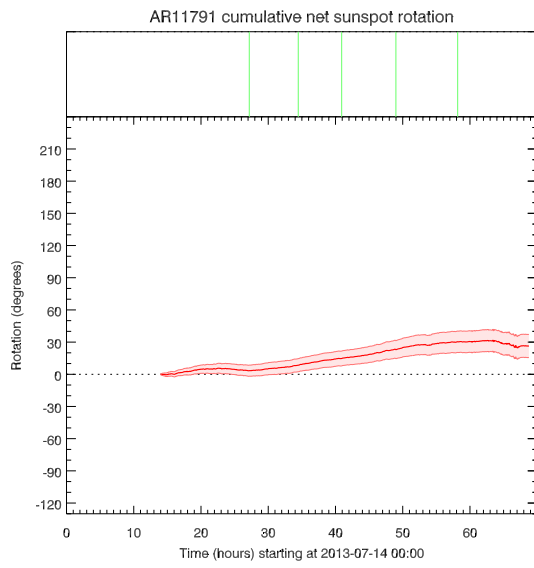


**(xxiii)** *AR11791*
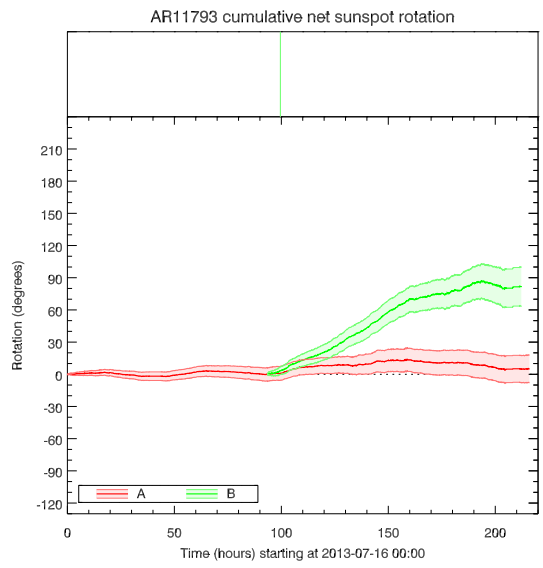


**(xxiv)** *AR11793*
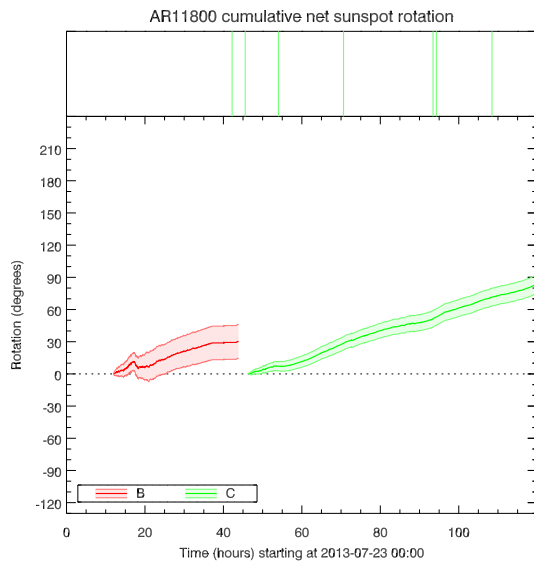
**(xxv)** *AR11800*
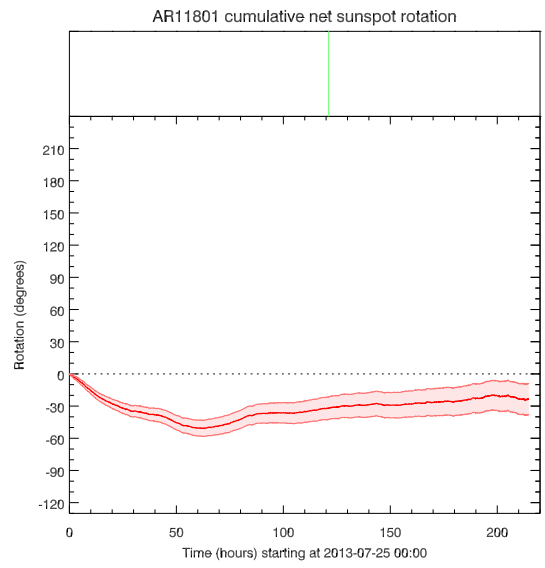


**(xxvi)** *AR11801*
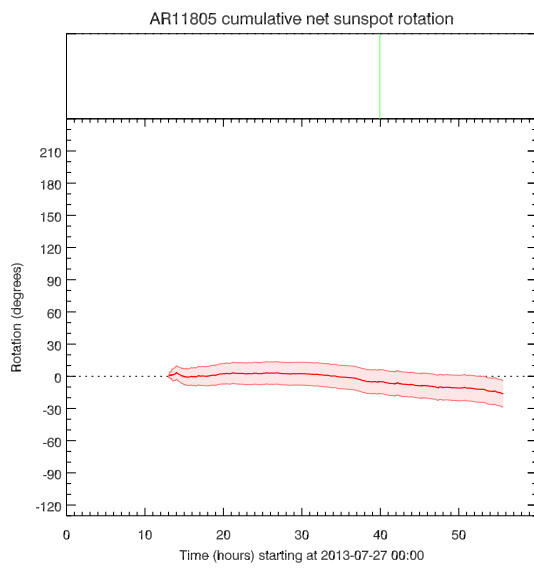


**(xxvii)** *AR11805*



**(xxviii)** *AR11806*

173
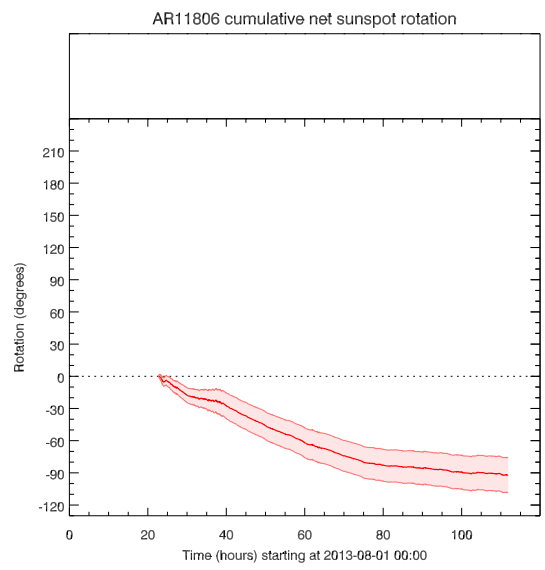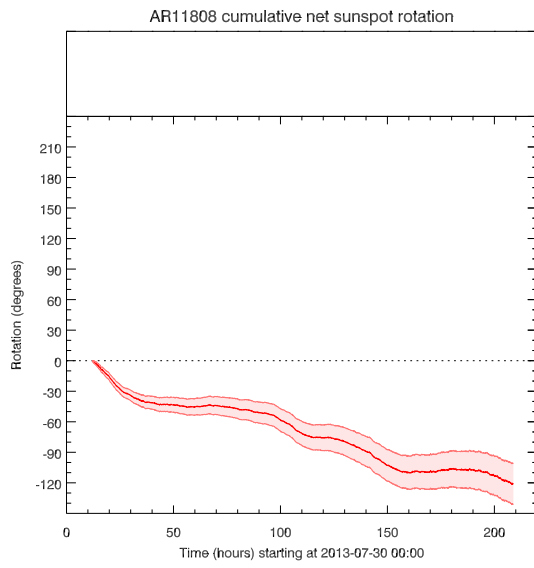
**(xxix)** *AR11808*
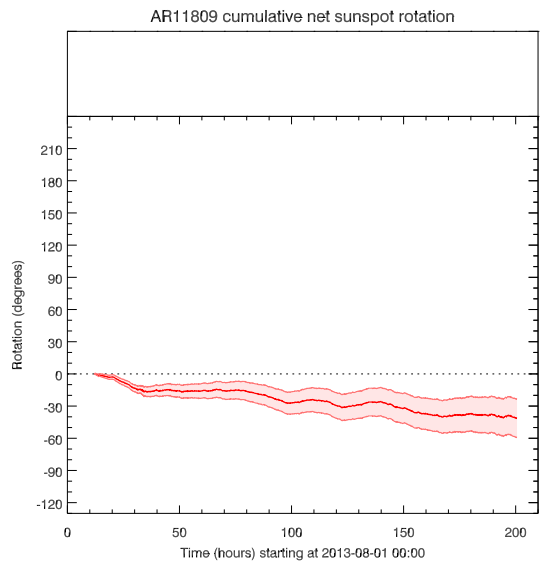


**(xxx)** *AR11809*
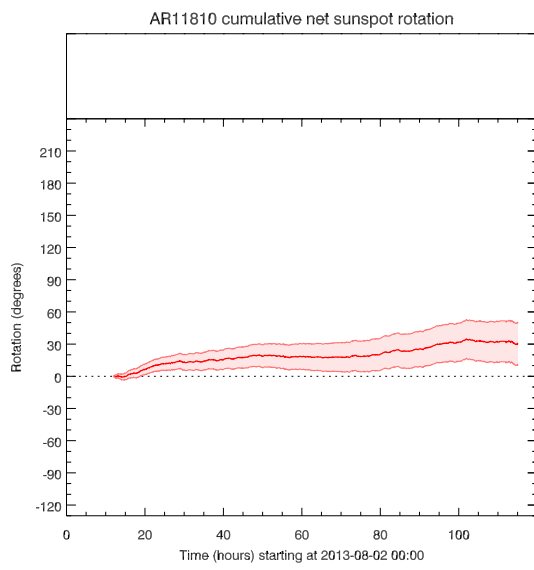


**(xxxi)** *AR11810*



**(xxxii)** *AR11817*

**(xxxiii)** *AR11818*



**(xxxiv)** *AR11823*



**(xxxv)** *AR11824*



**(xxxvi)** *AR11825*

**(xxxvii)** *AR11827*

**(xxxviii)** *AR11835*